sciendo

Slovak Journal of Civil Engineering

Vol. 31, 2023, No. 3, 1 – 11
DOI: 10.2478/sjce-2023-0015

DEVELOPMENT OF A CONCEPTUAL SNOW SUB-MODEL: APPLICATION IN METEOROLOGICAL STATIONS, SLOVAKIA

Miroslav KANDERA[1*], Roman VÝLETA[1]

Abstract

A semi-distributed rainfall-runoff Approximate Redistributive Balance (ARB) model is currently in development as a tool for the assessment and analysis of the water management balance at the level of micro-basins on the territory of Slovakia. For the winter season, it is necessary to supplement the model with a sub-model for calculating the snow water equivalent (SWE) with a comparatively low amount of the input data necessary. Since SWE models generally operate in a daily time step, a new sub-model was developed and tested in monthly and weekly time steps in 30 meteorological stations in the north of Slovakia. When compared in a weekly time step with the snow sub-model of the HBV rainfall-runoff model and when the impact of switching from a monthly to weekly time step on the quality of the runoff simulation was evaluated, the results showed that the snow sub-model does react to sudden snowmelt better when compared to the modified version of the HBV snow sub-model used. Using a weekly time step for the snow sub-model in a monthly ARB model runoff simulation showed an increase of accuracy (NSE change from 0.89 to 0.92) in one case, while maintaining the same level of accuracy in the second one.

Address

[1] Dept. of Land and Water Resources Management, Faculty of Civil Engineering, Slovak University of Technology in Bratislava, Slovakia

* ***Corresponding author:*** miroslav.kandera@stuba.sk

Key words

- Snow model,
- Approximate redistributive balance,
- Water evaluation and planning,
- Runoff,
- Snow water equivalent.

1 INTRODUCTION

Within the water management balances of Slovakia, the evaluation in a monthly time step has an established form, not only legislatively, but also regarding the availability of the water consumption data measured (Slovak Hydrometeorological Institute, 2021; Kandera and Výleta, 2021). To use rainfall-runoff modeling for the purpose of expanding an assessment of the water management balance beyond the profiles of water gauging stations, a compatible Approximate Redistributive Balance (ARB) model was developed (Kandera and Výleta, 2023), regarding the daily time step in rainfall-runoff modeling and the monthly time step in an assessment of the water management balance. This model requires a relatively small range of input data, works exclusively with hydrological and water management data, and enables a monthly water management assessment to be refined to a weekly time step. The model was built in Water Evaluation And Planning (WEAP) software for integrated water resources planning, it provides a comprehensive, flexible and user-friendly framework for planning and analysis with a wide range of time step options from daily to annual, including weekly and monthly options (Sieber and Purkey, 2015). The input data can also be used in the daily time step, while the software automatically processes it in the data structure for the time step selected. It is possible in its user environment to define new variables and their properties using combinations of a wide range of functions that fulfil an essential aspect in the development of the ARB model. Usual descriptions or analyses of a water balance do not often consider the impact of snow (Keszeliová et al., 2021; Olofintoye et al., 2022; Yonus and Hassan, 2022), either for a temperate/warm climate or the large scale of a modeled basin. To evaluate the winter season

as accurately as the summer, it was necessary for the ARB model to develop and include a snow sub-model that would simulate the processes of the snow accumulation, melting and runoff processes.

The snow models can be classified into different categories according to the spatial distribution characteristics of the models or the different algorithms used. An historical development and overview of snow models was provided by Zhou et al. (2021). Initially, the streamflow of the river was estimated by establishing a statistical relationship between the variables measured (such as the snow cover area, snow water equivalent) and snowmelt runoff (Dewalle and Rango, 2008). Over time, empirical equations have been used; their main principle is the assumption that there is a linear relationship between the air temperature and snow regime. This paper focuses on conceptual snow models, which have a physical meaning and are mature, with widely used methods. The conceptual snow models are hydrological models, which establish an empirical relationship between a snow regime and the temperature. These models can also be called degree-day models because they are usually based on a degree-day factor (He et al., 2014). At the present time, it is possible to modify these models to meet a variety of needs and thus satisfy the requirements of a large number of researchers. Such classic degree-day models also include the Snow Runoff Model (SRM) and the Hydrologiska Byråns Vattenbalansavdelning (HBV) model, see Martinec (1998) and Bergström and Singh (1995). These models have been continually modified and improved due to their ease of generalisation and broad applicability all over the world (Abudu et al., 2012; Zhang et al., 2014; Artimani et al., 2019; Hussainzada et al., 2021; Seibert and Bergström, 2022).

The aim of this paper was to develop a new conceptual snow sub-model, test it at selected meteorological stations in Slovakia, and incorporate it as a sub-model in the ARB model in the pilot basin. The snow sub-model of the HBV model was used to compare the snow regime simulation.

2 METHODS AND MATERIAL

2.1 Methodology

The many studies comparing snow models (Feng et al., 2008; Rutter et al., 2009) have highlighted the higher reliability of physically-based approaches such as the energy balance approach in models simulating snow conditions, which offer more realistic physical detail of the sub-processes (Wagner et al., 2009), but are often associated with intensive data requirements and primarily operate on a daily time step. However, the snow sub-model presented is a conceptual model system operating on a weekly/monthly time step. The development of the structure of the snow sub-model was based on the condition that it must be compatible with the ARB model (i.e., equally semi-distributed), but also with the condition of keeping within the boundaries of data already used for the ARB model. In the case of this study, time series of daily precipitation (P), daily air temperature (T) and the weekly snow water equivalent (SWE) were used. The last input data is the digital elevation model (DEM) in an resolution sufficient for the determining altitude.

In the ARB model created using the WEAP software, the whole modeled basin is divided into sub-basins, where water gauging stations represent pour points; these sub-basins are then further divided into more detailed micro-basins, which have defined runoff coefficient values based on several characteristics. Each sub-basin has its own set of calibration parameters. A similar procedure was applied to the snow sub-model of the ARB model. Among all the regional variables that influence the occurrence of snowfall, i.e., latitude, altitude, the distance from major water bodies, and the nature of the regional air mass circulation (McKay and Gray, 1981), the altitude was chosen as the most appropriate integrable parameter. In the initial stages of the integration of the snow sub-model, it already became apparent that with a multi-day time step, the average air temperature was insufficient as an indicator of the conditions for the formation, maintenance and melting of snow. Within the weekly time step, the last few days are most important in terms of temperature, while the last week is the most important in terms of the month. The defining of the limits of snow formation and melting as two calibratable but absolute values also showed incompatibility. Gyawali and Bárdossy (2022) concluded that uncertainty in the representation of snow accumulation and melt processes (e.g., in the HBV model) can be the result of calibration according to the runoff from the basin, which exhibits a compensating behavior with other non-snow-related parameters. Therefore, the new snow sub-model is calibrated only on snow water equivalent data.

From the point of view of the rainfall-runoff model, the calculation of the change in the snow water equivalent from one time step to another is necessary to define its effect on the relationship between precipitation and runoff (Holko et al., 2021). When calculating in a multi-day time step, the SWE value at the end of this time step is essential in order to know how much water in the snow was preserved for the next time step and how much of the snow melted. This applies both in the calculation of SWE and in the data measured to which the snow sub-model is calibrated. In (DeWalle and Rango, 2008), the change of SWE, defined as the snowpack water balance, was described by the equation:

$$\Delta SWE = SWE_{t2} - SWE_{t1} \tag{1}$$

where ΔSWE is the snowpack water balance; and $SWE_{t2} - SWE_{t1}$ is the change in the snow water equivalent (liquid and solid) of the snowpack over the time interval $t_2 - t_1$.

In the new snow sub-model, this equation for the calculations in time step i was modified to form:

$$SWB = SWE_{(i-1)} - SWE_i \tag{2}$$

where SWB is the snowpack water balance [mm]; SWE_{i-1} is the snow water equivalent in time step i-1 [mm]; and SWE_i is the snow water equivalent in time step i [mm].

The structure of the snow sub-model was constructed so that it better reflects the changes at the end of the time step; the temperature at the end of the time step T_{end} [°C] was also included as an input variable. In the weekly, but especially in the monthly time step, using only the last day at the end of the time step would lead the subsequent calculations to an extreme, since in many cases, the temperatures on a given day can be significantly outside the average temperature of the week/month. In the process of developing the snow sub-model it was found, that based on the analysis of the time series of daily temperatures, the average temperature for the last quarter of the time step has a relatively good predictive value concerning the temperature at the end of the time step, while avoiding extreme fluctuations. Therefore, it was decided that T_{end} would be the average temperature of the last 2 days for the weekly time step and the average temperature of the last week for the monthly time step.

Jonas et al. (2009) determined that based on their analysis of the snow density and depth data of 50 years from 37 sites over

Tab. 1 *Snow sub-model variables and calibration parameters (T_{Csw} - coefficient of the threshold value of snow regime, X_{Csw} - index value, C_{sw} - snow formation coefficient, C_{sp} - snow preservation coefficient, SWE - snow water equivalent, C_T, C_x, C_{Cx}, C_{Cy}, C_{spx} - calibration parameters, T - average air temperature, T_{end} - average air temperature at the end of the time step, P - average precipitation).*

Output variables	Parameters of calibration	Input data	Input variables
T_{Csw}	C_T	T, T_{end}	-
X_{Csw}	C_x	T, T_{end}	-
C_{sw}	C_{Cx}	T, T_{end}	X_{Csw}
	Cc_y		
C_{sp}	C_{spx}	-	C_{sw}
			SWE
SWE	-	P	C_{sw}
			T_{Csw}

the entire Swiss Alps, the bulk density of snow is mainly affected by four factors i.e., the season, snow depth, altitude, and location. When used in modeling with the ARB model, the altitude (h) of individual micro-basins serves as a simple tool for redistributing the total SWE in the sub-basin. In order that its influence is not too extreme, it is entered into the calculation in the form of ln(h), thanks to which the altitude range in Slovakia (from 94 to 2,654.4 m a.s.l.) is flattened to a range of values of 4.54 - 7.88. In order for it to be applicable in the calculations o f the individual variables in which it enters the calculations, it is always multiplied by the given calibration parameter. The new sub-model consists of 5 variables calculated with 5 calibration parameters, summarized in tab. 1.

The T_{Csw} variable in the form of the coefficient of the threshold value of the snow regime replaces the two threshold values of the snow formation and melting. Instead of two separate limit values, it is based on a function that in a 5 °C range goes from the coefficient values of 1 to 0, while the input is the minimum value between T and T_{end}. By adding ln(h) + C_T, it is possible to shift the function during the calibration in order to better suit the conditions of the sub-basin modeled.

$$T_{Csw,i} = f(min(T_i, T_{end,i}) + \ln(h) C_T) \quad (3)$$

where $T_{Csw,i}$ is the coefficient of the threshold value of the snow-melt [-]; T_i is the average temperature in time step i [°C]; $T_{end,i}$ is the average temperature at the end of time step i [°C]; and C_T is the calibration parameter [-].

The typical course of the dependence of T_{Csw} on the changing T_i, T_{end} and the calibration parameter C_T is shown in Fig. 1.

The variable X_{Csw} as an index value (0,1,2) determines whether the value of T_i (index 0), the combination of T_i and $T_{end,i}$ (index 1), or only the $T_{end,i}$ value (index 2) is used in the calculation of the snow formation coefficient (C_{sw}). This variable combines several conditions based on the development of the T_i, T_{i-1}, T_{i+1} and $T_{end,i}$ values and compares them to each other based on individual combinations of the conditions listed below. The conditions are set to look for two specific cases where $T_{end,i}$ fits the calculations partially or more than T_i.

The first case (X_{Csw} = 1), T_i is extremely low compared to $T_{end,i}$, T_{i-1} and T_{i+1}. Calculating only with the T_i would result in too high a value of the snow formation coefficient.

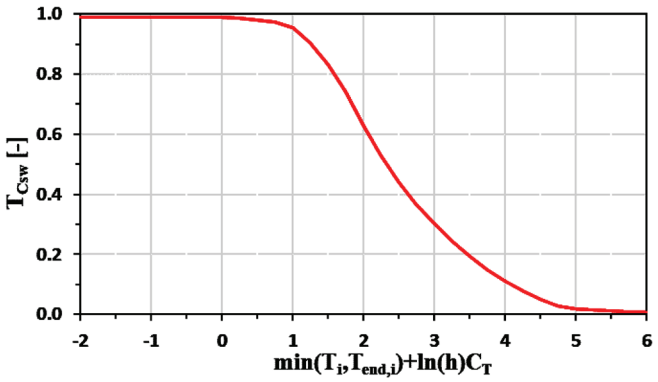

Fig. 1 *Function of variable T_{Csw} (modified from U.S. Army Corps of Engineers, 1998).*

In the second case (X_{Csw} = 2), T_i is lower than T_{i-1} but higher than T_{i+1} (T_i is in the middle of the process of getting colder). $T_{end,i}$ is lower than T_i and the average of T_i, T_{i-1}, T_{i+1}; at the same time, $T_{end,i}$ is higher than T_{i+1}. These conditions do try to detect situations when at the end of the time step, there in an extreme cooling compared to the trend, but at the same time the next time step is even colder, so the cooling continues. Calculating only with the T_i would result in a low value of the snow formation coefficient.

$$X_{Csw,i} = \begin{cases} 2,\ T_{i-1} > T_i + \ln(h)\, C_X < T_{i+1} \cap T_{end,i} > T_i \cap T_{end,i} > (T_i + T_{i-1} + T_{i+1})/3 \cap T_{end,i} \le T_{i+1} \\ 2,\ T_{i-1} > T_i > T_{i+1} \cap T_{end,i} < T_i \cap T_{end,i} < (T_i + T_{i-1} + T_{i+1})/3 \cap T_{end,i} > T_{i+1} \\ 1,\ T_{i-1} > T_i + \ln(h)\, C_X < T_{i+1} \cap T_{end,i} > T_i \cap T_{end,i} > (T_i + T_{i-1} + T_{i+1})/3 \\ 1,\ T_{i-1} > T_i + \ln(h)\, C_X < T_{i+1} \cap T_{end,i} \le T_{i+1} \\ 1,\ T_{i-1} > T_i > T_{i+1} \cap T_{end,i} < T_i \cap T_{end,i} < (T_i + T_{i-1} + T_{i+1})/3 \\ 1,\ T_{i-1} > T_i > T_{i+1} \cap T_{end,i} > T_{i+1} \\ 0,\quad \textit{neither condition is met} \end{cases} \quad (4)$$

where C_x is the calibration parameter [-].

The snow formation coefficient of (C_{sw}) defines how much of the precipitation in a given time step is snow and remains in the form of snow during the time step. It is also included in the calculation of the snow preservation coefficient. Similar to the case of T_{Csw}, a function with a wider range from -3 to 3 °C is used for its definition, while it reaches a value of 1 only at -10 °C. The calculation of the coefficient of snow formation is defined as:

$$C_{sw,i} = f(x)\ \ln(h) C_{Cy}\ while\ x = \begin{cases} T_{end,i}, & X_{Csw} = 2 \\ \frac{T_i + T_{end,i} C_{Cx}}{1 + C_{Cx}}, & X_{Csw} = 1 \\ T_i, & X_{Csw} = 0 \end{cases} \quad (5)$$

where C_{Cy} and C_{Cx} are the calibration parameters.

Fig. 2 on the left shows the course of the dependence of C_{sw} on the input temperature determined by X_{Csw}. One of the key variables affecting the ability to preserve snow is the height of the existing layer of the snow cover. It is therefore partially included in the calculation of the snow preservation coefficient (C_{sp}), which is defined as:

$$C_{sp,i} = \frac{C_{sw,i} + f(SWE_{i-1} C_{sw,i-1}) C_{spx}}{1 + C_{spx}} \quad (6)$$

where SWE_{i-1} is the snow water equivalent in time step i-1 [mm]; $C_{sw,i-1}$ is the coefficient of snow formation in time step i-1 [-]; and C_{spx} is the calibration parameter [-].

The function of C_{sp}, which is on the right side of Fig. 2, is dependent on C_{sw} in time step i-1 multiplied by SWE in the previous time step i-1. The sudden change in the function of C_{sp} at the value of 10 mm is based on the assumption that a certain, yet hard to

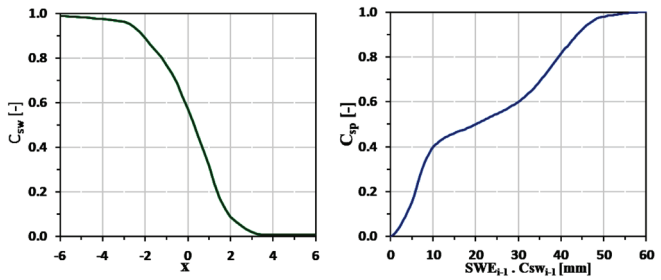

Fig. 2 *Function of variable C_{sw} adapted from U.S. Army Corps of Engineers (1998) (left), and function of variable C_{sp} (right).*

exactly determine, thickness of the snow cover is necessary to stabilize the formation and maintenance of snow over a long period of time.

DeWalle and Rango (2008) noted that when the depth of the snowpack decreases to levels (20–25 cm) that allow for the transmission of shortwave radiation to the ground in the late spring, ground warming and heat conduction become relatively more important.

The SWE calculations are composed of the snow water equivalent from the previous time step, which is multiplied by the snow preservation coefficient; and the precipitation multiplied by the snow formation coefficient is added to it. In the final step, it is multiplied by the T_{Csw}, while the whole form of the equation is:

$$SWE_{,i} = \left(SWE_{,i-1}C_{sp,i} + P_i C_{sw,i}\right)T_{Csw} \tag{7}$$

According to the above-described methodological approach, the new snow sub-model was created in monthly and weekly steps. The performance of these sub-models is compared at a weekly time step with the snow sub-model of the HBV model modified by the method of Valent (2014) from a daily to a weekly time step, while the degree-day factor was changed over time (for individual months of the year). For a statistical evaluation of the results, the Nash-Sutcliffe Efficiency Coefficient (NSE) and Mean Absolute Error (MAE) values are calculated. In addition, the Normalised Mean Absolute Error (NMAE) is added to the evaluation to better reflect the accuracy of the model with a wide range of the snow water equivalent measured between meteorological stations. The NMAE was used in a modified version of 1 - NMAE to better match the NSE system (1 = perfect match).

2.2 Data

In the test phase of the snow sub-model, 30 meteorological stations were selected for modelling SWE throughout Slovakia (Fig. 3) and divided into three groups according to their altitude. The altitudes in the first group (A) range up to 500 m a.s.l . ($h < 500$ m a.s.l.); the altitudes in the second group (B) range from 500 to 1500 m a.s.l. (500 m a.s.l. $< h <$ 1500 m a.s.l.) and in the last group (C) range above 1500 m a.s.l. ($h >$ 1500 m a.s.l.), see Tab. 1. We used the input data, as described in Tab. 2, from the period 5.11.2013 to 29.4.2019, i.e., 25 weeks.

In the application phase, by switching from a monthly to a weekly time step, the improvement of the runoff simulation for the ARB model was compared at 2 individual calibration sub-basins (with two separate validation sub-basins within them) in the lower Hron basin at Slovakia. The time series of the hydrometeorological data was chosen to be as similarly long as in the test phase.

Since the ARB model is semi-distributed, a time series of the average values (precipitation and air temperature) was calculated for each micro-basin using zonal statistics from raster data (500 x500) created using interpolation methods (IDW and kriging methods) from meteorological stations in the study area (45 stations for the precipitation and 14 stations for the temperature).

Tab. 2 *Selected meteorological stations divided into groups A, B and C based on their altitude.*

Group	h [m a.s.l.]	ID	Meteorological station	Group	h [m a.s.l.]	ID	Meteorological station
A.	163	826	Piešťany	B.	569	878	Liptovský Mikuláš - Ondrašová
	174	847	Topoľčany		570	950	Podolínec
	176	993	Kamenica n. Cirochou		640	874	Liptovský Hrádok
	188	846	Veľké Ripňany		694	934	Poprad
	216	976	Tisinec		703	952	Gánovce
	260	867	Prievidza		758	879	Kremnické Bane
	275	900	Žiar nad Hronom		827	935	Tatranská Lomnica
	305	962	Bardejov		901	938	Telgárt
	305	977	Medzilaborce		972	876	Podbanské
	307	955	Prešov-vojsko		975	959	Tatranská Polianka
	391	992	Osadné		1030	936	Javorina
	395	893	Martin		1354	933	Štrbské Pleso
	402	963	Jakubovany	C.	1778	931	Skalnaté Pleso
	462	897	Turčianske Teplice		2008	916	Chopok
	465	951	Červený Kláštor		2635	930	Lomnicky Štít

Tab. 3 *Input data used for the conceptual snow sub-model and modified snow sub-model of the HBV model developed: Slovak Hydrometeorological Institute - SHMÚ, Geodetic and Cartographic Institute Bratislava - GKÚ, Airborne Laser Scanning – ALS.*

Input data	Source	Measurement	Data use
Daily average temperature [°C]	SHMÚ	Stations	Average temperature in time step i [°C]
Total daily precipitation [mm]			Total precipitation in time step i [mm]
Weekly measured snow water equivalent [mm]			Snow water equivalent at the end of time step i [mm]
DEM 1x1 [m]	GKÚ	ALS	Average altitude [m a.s.l.]

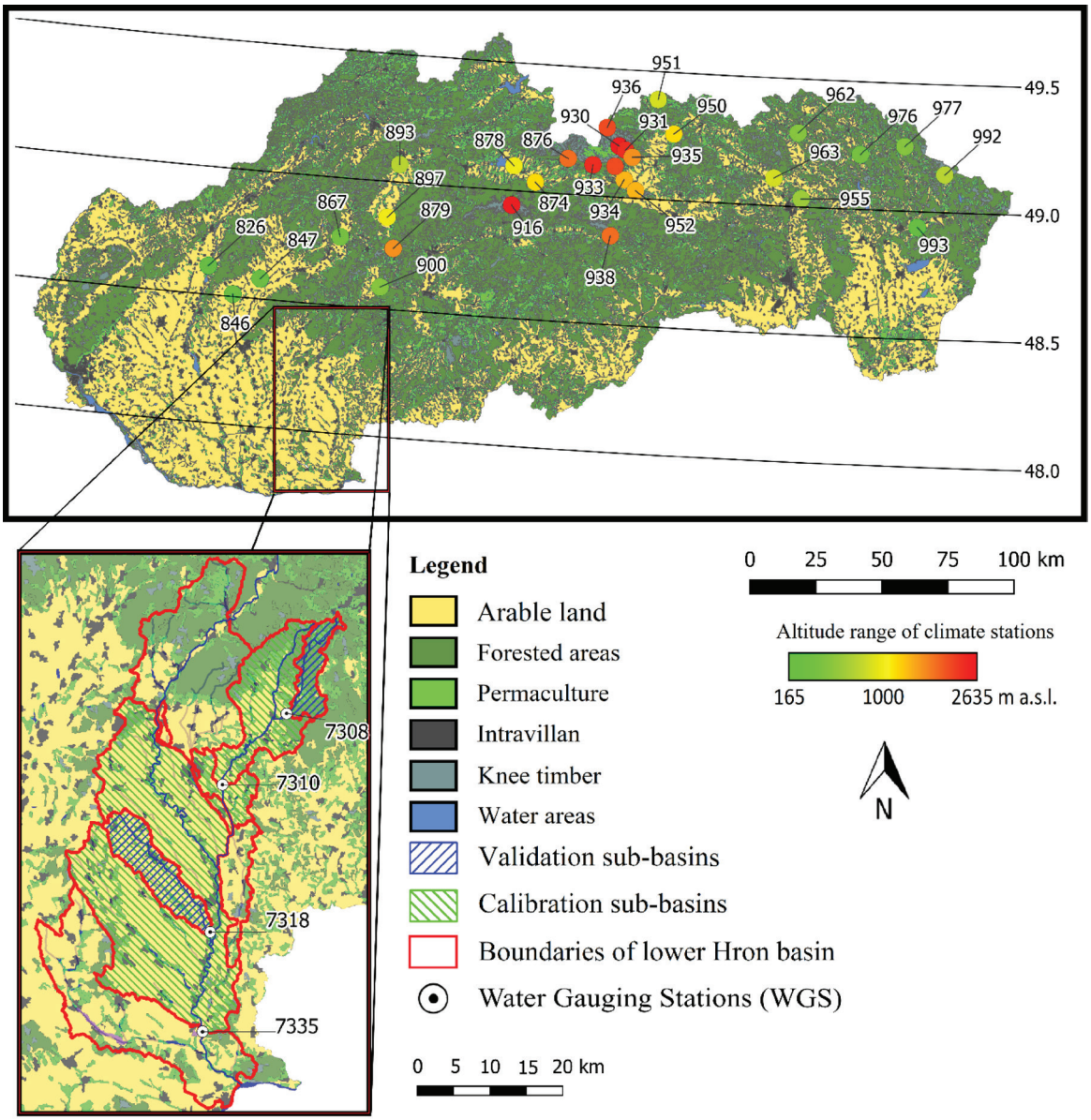

Fig. 3 *The location of the 30 meteorological stations, represented by colored points based on the altitude range and location of the two calibration sub-basins with their two subordinate validation sub-basins in the lower Hron basin at Slovakia.*

5 RESULTS

The results of the snow sub-model calibrations in terms of the different model performance metrics (the NSE and the 1-NMAE) for the meteorological stations studied are shown in Figs. 4 and 5. The ARB snow sub-model at the weekly time step outperforms both the HBV at the weekly time step and the ARB at the monthly time step, performing especially well in higher altitudes of groups B and C when compared to the weekly HBV or monthly ARB snow sub-models.

Compared to the NSE evaluation at Fig. 4, the 1-NMAE values at Fig. 5 show a steadier decrease in precision as the elevation rises, while confirming the best results for group B.

Since the aim of this paper was the development of a conceptual snow sub-model, Tab. 3 contains the calibration parameters of the

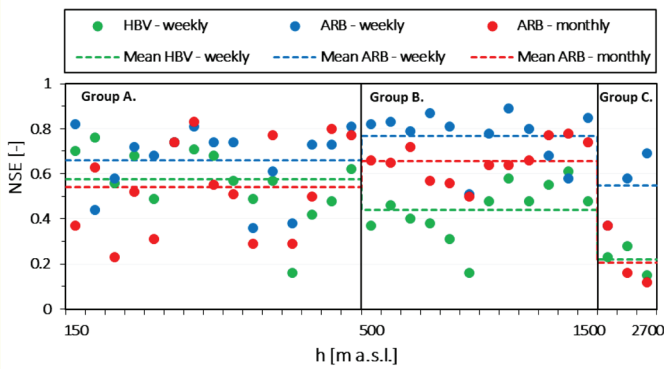

Fig. 4 *Comparison of HBV – weekly, ARB – weekly and ARB – monthly snow sub-model performance by NSE for 25 weeks in the years 2013-2019 with meteorological stations sorted by ascending altitude.*

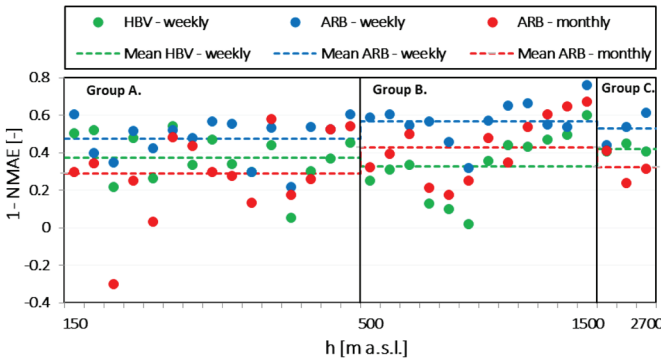

Fig. 5 *Comparison of HBV – weekly, ARB – weekly and ARB – monthly snow sub-model performance by 1- NMAE for 25 weeks in the years 2013-2019 with meteorological stations sorted by ascending altitude.*

Tab. 4 *Meteorological stations divided into altitude groups with a comparison of the results of Nash-Sutcliffe Efficiency (NSE), Mean absolute error (MAE), 1 – Normalized Mean absolute error (1-NMAE), and calibration parameters of ARB - weekly*

Group	ID	h	Statistics			Calibration parameters					
			NSE	MAE	1-NMAE						
		[m a.s.l.]	[-]	[mm]	[-]	C_T	C_{Cy}	Ln(h).C_{Cy}	C_{Cx}	C_{spx}	C_x
A.	826	163	0.82	1.5	0.58	0.1	0.26	1.30	0.19	0.27	0.81
	847	174	0.44	2.4	-0.01	0.5	0.24	1.25	0.00	0.14	0.50
	993	176	0.58	3.0	0.37	-6.7	0.18	0.95	0.25	0.00	0.11
	846	188	0.72	2.5	0.38	-0.5	0.20	1.07	0.00	0.12	0.10
	976	216	0.68	2.9	0.51	-0.4	0.17	0.93	0.72	0.05	0.04
	867	260	0.74	2.7	0.39	0.0	0.20	1.13	0.11	0.13	0.20
	900	275	0.81	2.9	0.48	-0.4	0.20	1.14	0.00	0.55	0.41
	962	305	0.74	3.2	0.58	-7.5	0.19	1.08	1.70	0.18	0.10
	977	305	0.74	6.7	0.54	-10.0	0.18	1.01	0.00	0.16	0.43
	955	307	0.36	3.6	0.38	-0.4	0.19	1.08	0.61	0.00	0.13
	992	391	0.61	10.0	0.51	-0.3	0.18	1.08	0.00	0.26	0.12
	893	395	0.38	6.1	0.10	0.0	0.16	0.93	0.22	0.28	0.11
	963	402	0.73	3.7	0.53	-2.3	0.17	1.03	0.75	0.05	0.22
	897	462	0.73	4.4	0.39	0.0	0.17	1.04	0.22	0.21	0.46
	951	465	0.81	8.7	0.54	-10.0	0.19	1.17	0.21	0.19	0.01
B.	878	569	0.82	3.2	0.56	0.5	0.19	1.22	0.00	0.13	0.52
	950	570	0.83	4.6	0.66	-0.8	0.16	1.04	0.00	0.07	0.21
	874	640	0.79	5.8	0.52	-0.2	0.16	1.03	0.28	0.03	0.06
	934	694	0.87	3.7	0.61	0.0	0.16	1.07	0.02	0.06	0.22
	952	703	0.81	4.1	0.57	-10.0	0.16	1.06	0.25	0.00	0.05
	879	758	0.51	23.0	0.11	0.0	0.15	0.99	0.06	0.07	0.98
	935	827	0.78	7.3	0.58	-6.6	0.15	1.04	0.00	0.03	0.31
	938	901	0.89	9.4	0.69	-10.0	0.16	1.08	0.00	0.06	0.26
	876	972	0.80	13.0	0.63	0.0	0.16	1.11	0.44	0.20	0.88
	959	975	0.68	11.0	0.51	-2.0	0.16	1.12	0.37	0.20	0.12
	936	1030	0.58	21.0	0.47	-0.4	0.15	1.03	0.00	0.37	0.61
	933	1354	0.85	22.0	0.75	-5.0	0.16	1.14	0.91	0.53	0.15
C.	931	1778	0.37	69.0	0.47	-15.0	0.14	1.05	2.00	0.18	0.03
	916	2008	0.58	58.0	0.64	-4.7	0.13	0.97	0.23	0.00	0.01
	930	2635	0.69	58.0	0.61	0.9	0.09	0.68	0.11	0.55	0.09
Avg.	A.	299	0.66	4.3	0.42	-2.5	0.19	1.08	0.33	0.17	0.25
	B.	833	0.77	10.7	0.56	-2.9	0.16	1.08	0.19	0.14	0.36
	C.	2140	0.55	61.7	0.57	-6.2	0.12	0.90	0.78	0.24	0.04

ARB - weekly snow sub-model and a detailed comparison of the NSE, MAE, and 1-NMAE results for the meteorological stations divided into altitude groups. By sorting the calibration parameters of the individual stations in Tab. 3, it is possible to observe that among the 5 parameters, only the C_{Cy} parameter shows a stable trend, i.e., decreasing with the increasing altitude. This parameter multiplied by the altitude logarithm regulates the snow formation coefficient C_{sw}.

In Tab. 3, it is also evaluated in the form $Ln(h).C_{Cy}$ with values in the range of 0.68 - 1.30, showing that in certain cases, the snow formation coefficient does exceed the value of 1, which indicates more snowfall in a given time step than the total amount of precipitation, which should not be possible. However, variable C_{sw} also influences the snow preservation coefficient C_{sp}. Upon closer examination of the variables calculated, the occurrence of cases where $C_{sw} > 1$ had a negative effect on the calculation of SWE was relatively in balance with a positive effect on its calculation. Therefore, limitation of the variable C_{sw} maximum value of 1 must be preceded by further analysis.

The C_T parameter ranged from -15 to 0.9, while both extremes were calibrated for the stations in group C. It was assumed that the C_T value would increase with the increasing altitude in order to lower the temperature limit for the snowmelt. The results showed that at stations with a relatively slow melting of snow, a low value of C_T can help to simulate such behavior, and the whole melting process remains only a gradual decrease of the snow formation coefficient C_{sw} and the snow preservation coefficient C_{sp}. According to the results, the assumption that the C_{spx}, C_{Cx} and C_x coefficients values will not indicate any trend and will only serve for the most accurate calibration without a wider context, is confirmed.

Figs. 6, 7, and 8 show the long-term mean weekly values of the snow water equivalent (SWE) for the period (2013–2019) calculated from the data observed, the data from the HBV - weekly and ARB - weekly snow sub-models, separately for the meteorological stations with the low (group A), medium (group B), and high elevations (group C). The lines in the graphs indicate the averages for the meteorological stations. Both weekly snow sub-models simulate SWE in the minimum-maximum range of the data observed in

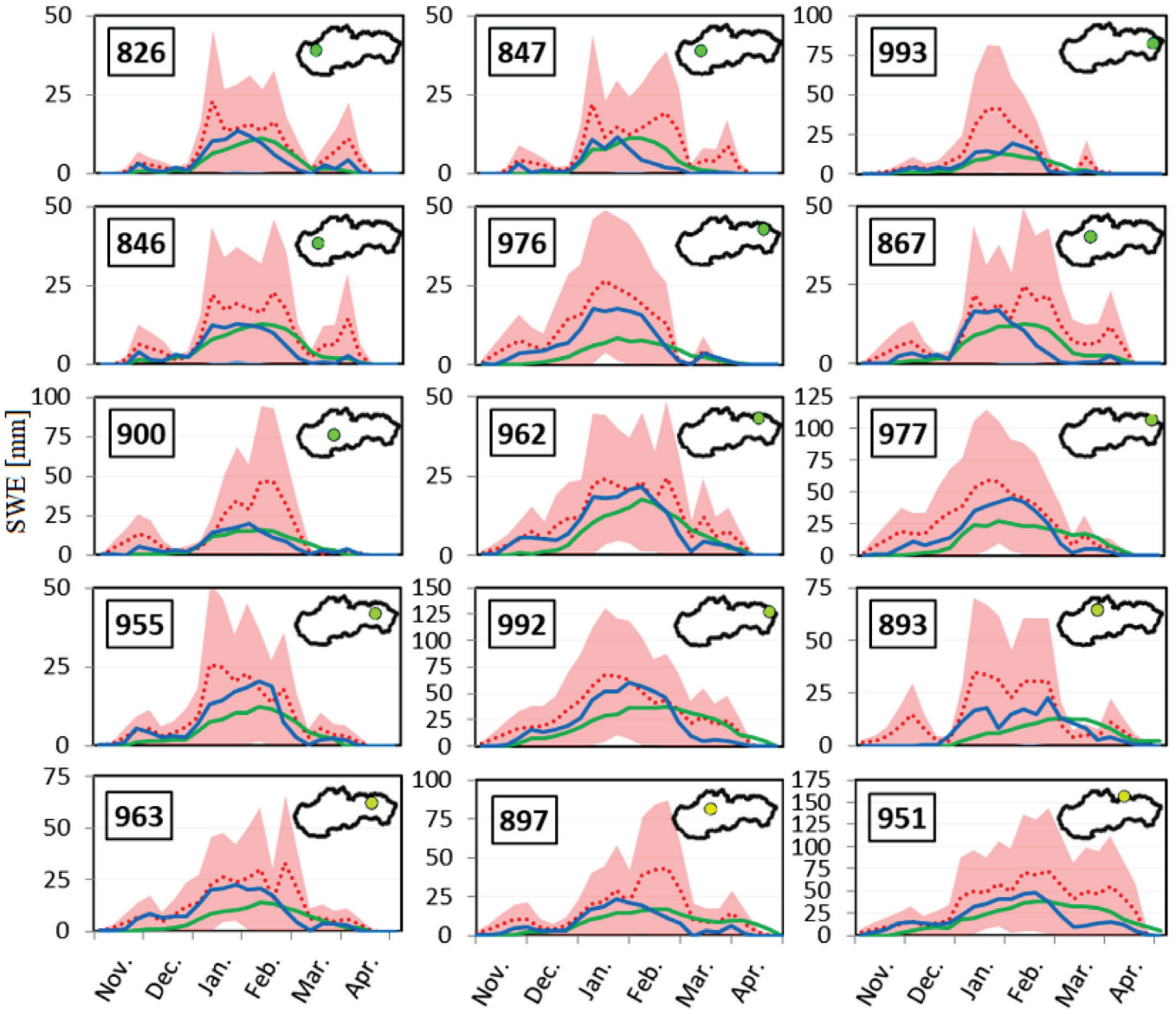

Fig. 6 *Long-term mean weekly SWE [mm] for stations in group A, sorted from top-left to bottom-right according to the increasing altitude: observed data (red dotted line), simulated data from the HBV - weekly sub-model (green line), and simulated data from the ARB - weekly sub-model (blue line). The minimum-maximum range of the SWE observed is in red area.*

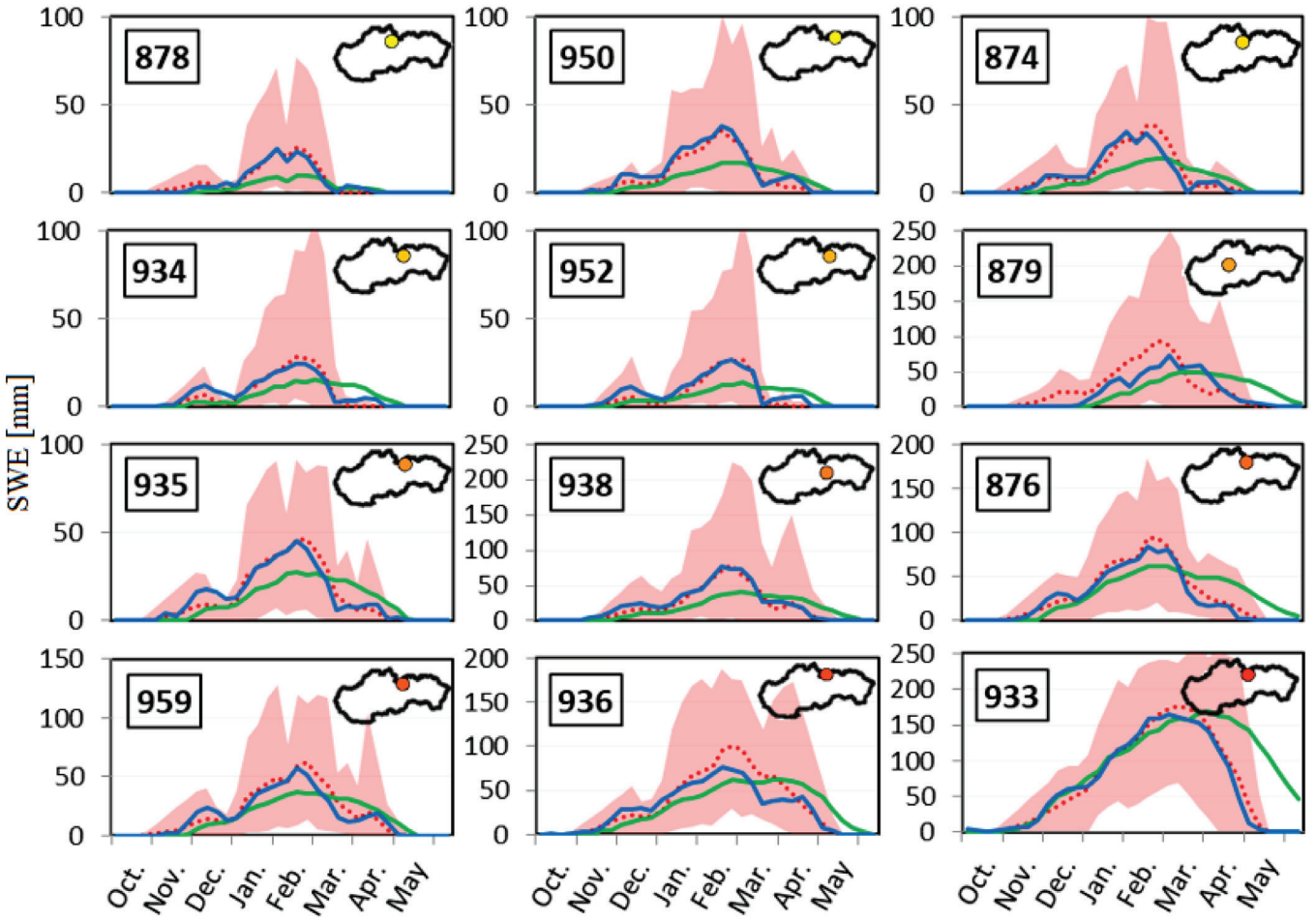

Fig. 7 *Long-term mean weekly SWE [mm] for stations in group B, sorted from top-left to bottom-right according to the increasing altitude: data observed (red dotted line), simulated data from the HBV - weekly sub-model (green line), and simulated data from the ARB - weekly sub-model (blue line). The minimum-maximum range of the SWE observed is in red area.*

the meteorological stations within group A and B (see Figs. 6 and 7). The HBV – weekly sub-model shows a steadier decrease in the SWE values, while the ARB – weekly sub-model is better able to adapt to sharp and sudden snowmelt, especially at the high altitudes of group C at Fig. 8.

The performance of the ARB - weekly and HBV - weekly sub-models was visually assessed using the correlations between the observed and simulated SWE in the meteorological stations divided into the altitude groups (Fig. 9). The ARB snow sub-model shows better correlations in general, especially in groups A and B, i.e., going from overestimating to underestimating, as the values increased in group C. In the case of the HBV, it steadily bends towards underestimating as the values increase, with a steady decrease of r^2 as the elevation rises.

4 DISCUSSION

In the ARB rainfall-runoff model of the pilot basin of the lower Hron River, the model was modified from a monthly to a weekly time step, with a snow sub-model calibrated to SWE in a week-

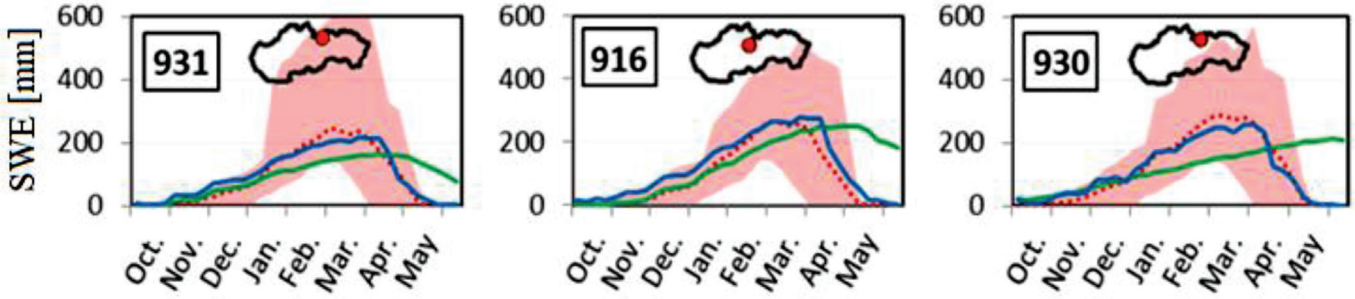

Fig. 8 *Long-term weekly SWE [mm] for stations in group C, sorted from left to right according to the increasing altitude: data observed (red dotted line), simulated data from the HBV - weekly sub-model (green line), and simulated data from the ARB - weekly sub-model (blue line). The minimum-maximum range of the SWE observed is in red area.*

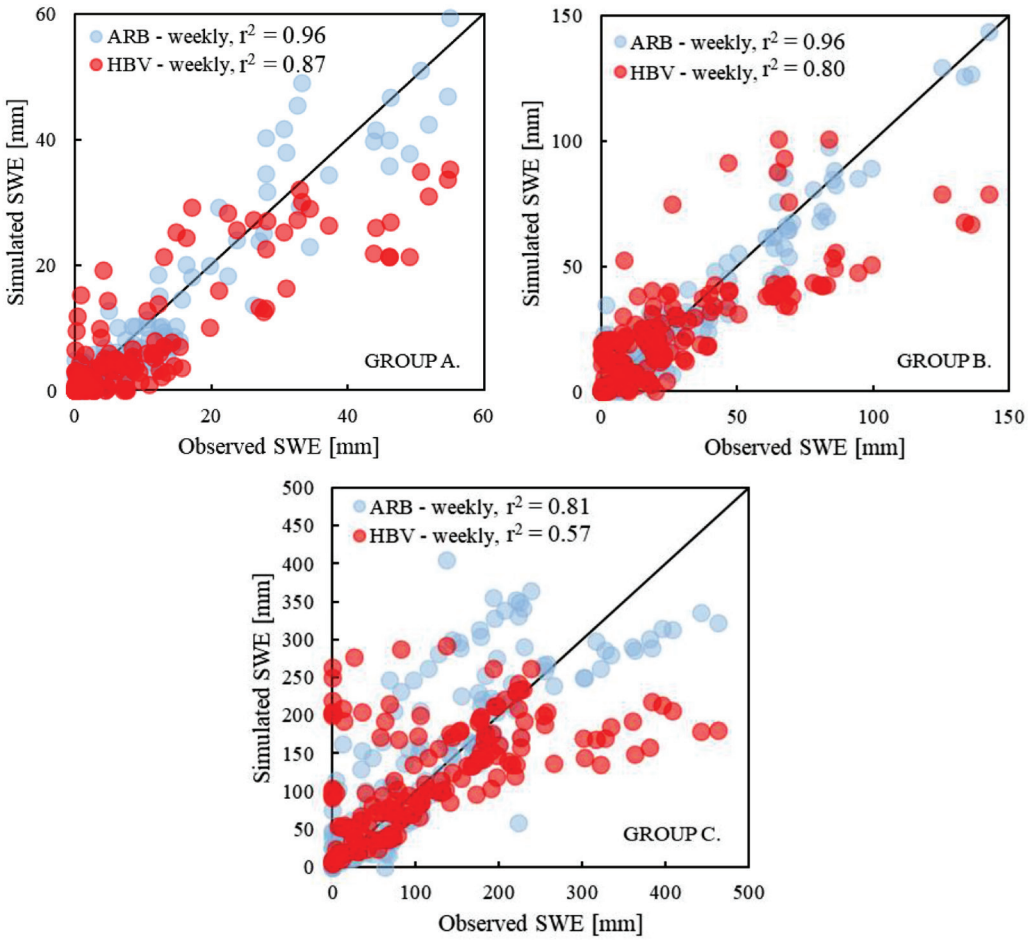

Fig. 9 *The correlation between the observed and simulated SWE: ARB – weekly (blue dots) and HBV – weekly (red dots) snow sub-model in weekly time steps for groups A, B and C.*

ly time step. Then the SWE was calculated in a weekly time step used as the input data back into the monthly model. The monthly rainfall-runoff model was then calibrated to the streamflow data from two calibration water gauging stations (WGS 7310 and WGS 7335). A comparison of the difference between the snow sub-model's performance within the weekly and monthly time steps was done based on the results from the two validation water gauging stations, WGS 7308 subordinate to WGS 7310 and WGS 7318 subordinate to WGS 7335.

The comparison in Fig. 10 does not show any sudden increase or decrease in accuracy, when using the weekly, instead of the monthly, calculated SWE in the ARB model. Statistically, the sub-basin

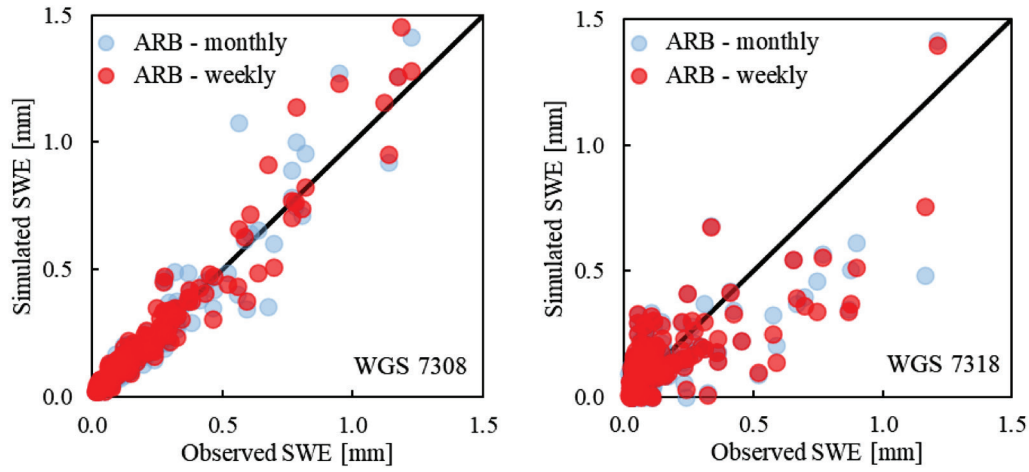

Fig. 10 *The correlation between the observed and simulated outflows with the use of SWE calculated in monthly (blue dots) and weekly (red dots) time steps; validation sub-basin C7308 (left) and validation sub-basin C7318 (right).*

of WGS 7308 had the NSE increased from 0.89 to 0.92 and r^2 from 0.9 to 0.92. On the other hand, sub-basin WGS 7318 showed no increase or decrease in the statistical results; it maintained both the NSE and r^2 at a value of 0.58. This proved how much of a smaller impact the SWE had on this more southernly sub-basin with the much lower average altitude (a decrease for 220 metres), while also considering that the WGS 7318 as a validation sub-basin was part of the much larger WGS 7335 calibration sub-basin. Simultaneously, WGS 7335 sub-basin had significant inflows from the upstream area, which had a serious impact on the calibration, and which also reduced the impact of SWE.

5 CONCLUSIONS

From the snowpack water balance point of view, the results showed that the ARB snow sub-model was developed to a level where it proved to simulate snow water content comparable to models such as the snow sub-model of the HBV model, which was, on the other hand, at a disadvantage in this comparison, since it had to be modified from its dedicated daily time step version to a weekly time step version to allow for the evaluation of the quality of the ARB snow sub-model simulation. Based on the results of the evaluation, the ability of the ARB snow model during simulation at 30 meteorological stations is considered sufficiently objective for its use in the redistribution of runoff at Slovakia. When evaluating the improvement of the impact on runoff by switching from a monthly to a weekly time step, the use of the sub-basins in the model of the lower Hron basin serves only as an outline, since a sufficiently objective assessment definitely requires more than a comparison of only 2 sub-basins. Regarding the improvement in the results when using a weekly, instead of a monthly, time step in the calculation of SWE for the ARB rainfall-runoff model, its effect depends on the elevation of the sub-basin itself, as well as the independence of its runoff regime, while with an increasing elevation and decreasing sub-basin size, we can assume an increasing necessity for a smaller time step.

Although a large number of sophisticated snow models operating in a smaller time step have been developed so far, for the purposes of the evaluation of water management balance and analysis of the water redistribution in the basin using the ARB model, this weekly/monthly snow sub-model developed represents a tool with a balanced ratio between the necessary input data, its complexity and a sufficiently good performance.

Acknowledgements

This work was supported by the Slovak Research and Development Agency under Contracts Nos. APVV-19-0340 and APVV-20-0374; and VEGA 1/0782/21.

REFERENCES

Abudu, S. - Cui, C. L. - Saydi, M. - King, J. P. (2012) *Application of snowmelt runoff model (SRM) in mountainous watersheds: A review.* Water Science and Engineering, 5(2), pp. 123-136. DOI: 10.3882/j.issn.1674-2370.2012.02.001

Artimani, M. M. - Zeinivand, H. - Tahmasebpour, N. (2019) *Performance evaluation of SRM and HBV model in simulation of snowmelt runoff in Bujin Basin*. Iran-Water Resources Research, 15(2), pp. 228-241.

Bergström, S. - Singh, V.P. (1995) *The HBV Model*; Water Resources Publications: Highland Ranch, CO, USA, 1995; pp. 443–476.

DeWalle, D. R. - Rango, A. (2008) *Principles of snow hydrology*. Cambridge University Press, 2008. ISBN 9780521823623

Feng, X. - Sahoo, A. - Arsenault, K. - Houser, P. - Luo, Y. - Troy, T. J. (2008) *The Impact of Snow Model Complexity at Three CLPX Sites*. Journal of Hydrometeorology, 9(6), pp. 1464-1481. DOI: 10.1175/2008JHM860.1

Gyawali, D. R. - Bárdossy, A. (2022) *Development and parameter estimation of snowmelt models using spatial snow-cover observations from MODIS.* Hydrology and Earth System Sciences, 26(12), pp. 3055-3077. DOI: 10.5194/hess-26-3055-2022

He, Z. H. - Parajka, J. - Tian, F. Q. - Blöschl, G. (2014) *Estimating degree-day factors from MODIS for snowmelt runoff modeling*. Hydrology and Earth System Sciences, 18(12), pp. 4773-4789. DOI: 10.5194/hess-18-4773-2014

Holko, L. - Danko, M. - Sleziak, P. (2021) *Snowmelt characteristics in a pristine mountain catchment of the Jalovecký Creek, Slovakia, over the last three decades*. Hydrological Processes, 35(4), e14128. DOI: 10.1002/hyp.14128

Hussainzada, W. - Lee, H. S. - Vinayak, B. - Khpalwak, G. F. (2021) *Sensitivity of snowmelt runoff modelling to the level of cloud coverage for snow cover extent from daily MODIS product collection 6*. Journal of Hydrology: Regional Studies, 36, 100835. DOI: 10.1016/j.ejrh.2021.100835

Jonas, T. - Marty, C. - Magnusson, J. (2009) *Estimating the snow water equivalent from snow depth measurements in the Swiss Alps.* Journal of Hydrology, 378(1-2), 161-167. DOI: 10.1016/j.jhydrol.2009.09.021

Kandera, M. – Výleta, R. (2023) *Development and validation of an Approximate Redistributive Balance model to estimate the distribution of water resources using the WEAP: The lower Hron river basin, Slovakia*, Acta Hydrolgica Slovaca, Volume 24, No. 1, 122-133

Kandera, M. - Výleta, R. - Liová, A. - Danáčová, Z. - Lovasová, Ľ. (2021) *Testing of water evaluation and planning (Weap) model for water resources management in the Hron river basin*. Acta Hydrologica Slovaca, 22(1), pp. 30–39. DOI: 10.31577/ahs-2021-0022.01.0004

Keszeliová, A. - Hlávčová, K. - Danáčová, M. - Danáčová, Z. - Szolgay, J. (2021) *Detection of Changes in the Hydrological Balance in Seven River Basins Along the Western Carpathians in Slovakia*. Slovak Journal of Civil Engineering, 29(4), pp. 49-60. DOI: 10.2478/sjce-2021-0027

Martinec, J. - Rango, A. - Roberts, R. - Baumgartner, M. F. (1998) *Snowmelt runoff model (SRM) user's manual*, p. 84. Berne: University of Berne, Department of Geography

Olofintoye, O. O. - Ayanshola, A. M. - Salami, A. W. - Idrissiou, A. - Iji, J. O. - Adeleke, O. O. (2022) *A study on the applicability of a Swat model in predicting the water yield and water balance of the Upper Ouémé catchment in the Republic of Benin*. Slovak Journal of Civil Engineering, 30(1), pp. 57-66. DOI: 10.2478/sjce-2022-0007

Rutter, N. - Essery, R. - Pomeroy, J. - Altimir, N. - … - Yamazaki, T. (2009) *Evaluation of forest snow processes models (SnowMIP2)*, Journal of Geophysical Research: Atmospheres, 114(D6). DOI: 10.1029/2008JD011063

Seibert, J. - Bergström, S. (2022) *A retrospective on hydrological catchment modelling based on half a century with the HBV model*, Hydrol. Earth Syst. Sci., 26, pp. 1371–1388, DOI: 10.5194/hess-26-1371-2022

Sieber, J. - Purkey, D. (2015) *Water Evaluation And Planning (WEAP) System user guide*, Stockholm Environment Institute, Somerville, MA, USA.

Slovak Hydrometeorological Institute (2021) *Water resource balance of surface water quantity for 2020*, SHMÚ Bratislava, 399 pp.

U.S. Army Corps of Engineers, (1998) *Runoff from Snowmelt*. Engineer Manual, 1110-2-1406, Washington, DC.

Valent, P. (2014) *Rainfall-runoff modeling for frequency analysis of flows*. PhD thesis, Slovak Technical University in Bratislava, Faculty of Civil Engineering, 156 pp.

Wagner, W. - Verhoest, N. E. C. - Ludwig, R. - Tedesco, M. (2009) *Editorial: Remote sensing in hydrological sciences*. Hydrology and Earth System Sciences, 13(6), pp. 813-817. DOI: 10.5194/hess-13-813-2009

Yonus, M. - Hassan, S. A. (2022) *The Impact of Climate Change on Stochastic Variations of the Hydrology of the Flow of the Indus River. Slovak Journal of Civil Engineering*, 30(1), pp. 33-41. DOI: 10.2478/sjce-2022-0004

Zhang, G. - Xie, H. - Yao, T. - Li, H. - Duan, S. (2014) *Quantitative water resources assessment of Qinghai Lake basin using Snowmelt Runoff Model (SRM).* Journal of Hydrology, 519, pp. 976-987. DOI: 10.1016/j.jhydrol.2014.08.022

Zhou, G. - Cui, M. - Wan, J. - Zhang, S. (2021) *A review on snowmelt models: progress and prospect.* Sustainability, 13(20), 11485. DOI: 10.3390/su132011485

sciendo

Slovak Journal of Civil Engineering

Vol. 31, 2023, No. 3, 12 – 23
DOI: 10.2478/sjce-2023-0016

CALCULATION OF THE CONSTRUCTIVE NONLINEARITY OF RIBBED REINFORCED CONCRETE SLABS OF SELF-STRESSED COVERING PANELS

Anton HASENKO[1*], Volodymyr SEMKO[2], Serhii SKLIARENKO[3]

Abstract

Precast reinforced concrete constructions meet the requirements of industrialization, high manufacturability, and cost-effectiveness at a reasonably high level. The ribs in constructions perform load-bearing functions, and the slab part performs enclosing functions. Often before the installation of such structures at a construction site, they are mounted from assembly elements. The overall dimensions of the elements are limited by transportation requirements. During such an aggregated mounting, the assembly units work according to a calculation scheme that differs from an operational scheme. The structural nonlinearity of ribbed reinforced concrete slabs during transportation, mounting, and installation, and the operation of a combined spatial covering panel were investigated in this paper. The effects were identified, and a rational design of nodes connecting the individual prefabricated units into a spatial structure was developed. With the help of these nodes, it is possible to create unloading support moments, which will reduce the internal forces in the design cross-sections. The effects of changes in the width of the reinforced concrete slab shelves on the internal forces of the load-bearing ribs of a wall and a roof panel were investigated.

Address

[1] Dept. of Construction and Civil Engineering, Educational and Scientific Institute of Architecture, Construction and Land Development, "Yuri Kondratyuk Poltava Polytechnic" National University, Poltava, Ukraine

[2] Division of Structural Engineering, Institute of Building Engineering, Department of Civil and Transport Engineering, Poznan University of Technology, Poznan, Poland

[3] "Poltava-Project" (private enterprise), Poltava, Ukraine

* ***Corresponding author:*** gasentk@gmail.com

Key words

- Combined spatial covering panel,
- Structural nonlinearity.

1 INTRODUCTION

Precast reinforced concrete meets the requirements of industrialization, high manufacturability, and cost-effectiveness at a reasonably high level (Tkachenko et al., 2019; Zielińska and Grębowski, 2015). Building structures made of reinforced concrete can perform both load-bearing and enclosing functions (Shahsavar and Tofighi, 2014). To simplify the installation technology and reduce the building construction time during the development of working drawings of prefabricated reinforced concrete structures, designers strive to combine their load-bearing and enclosing functions (Lam et al., 2009). This explains the emergence of a whole range of ribbed, prefabricated, reinforced concrete structures, in which the ribs perform load-bearing functions (Abdel-Kareem et al., 2015; Sridhar and Prasad, 2019), and the slab part perform enclosing functions (Bouzid and Demagh 2011). Buildings made of such ribbed, prefabricated reinforced concrete structures are called “quick-mounted”. The field of quick-mounted building exploitation is often limited to production buildings for agricultural or warehouse purposes. However, there are problems with providing housing for displaced persons in the conditions of a war and post-war periods (Łotysz, 2016); therefore, the adaptation of such buildings to dormitory-type residential buildings is an urgent issue.

1.1 Analysis of existing studies and publications on the specified problem

Quick-mounted buildings can have a wall or frame construction scheme. In the first case (wall construction scheme of the quick-mounted buildings), ribbed reinforced concrete panels for walls and roofing perform supporting and enclosing functions (see Fig.1), which significantly reduce the number of mounting elements (Semko and Hasenko, 2020). In the second case (frame construction scheme of the quick-mounted buildings), it is first necessary to install load-bearing rod frame structures and then to install enclosing planar elements with stiffeners (Holly and Abrahoim, 2020; Pershakov, 2007). Such a mounting sequence leads to an increase in the number of mounting joints on the construction site, which complicates the building installation process and imposes some seasonal restrictions on its implementation.

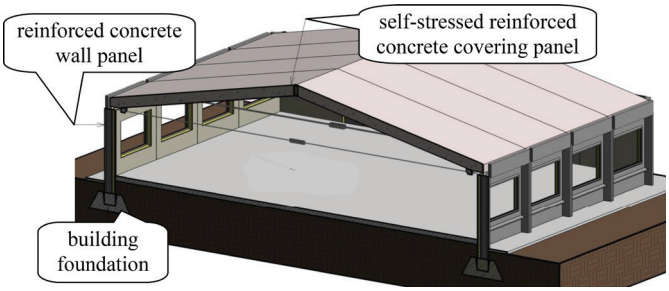

Fig. 1 *Structural scheme of walls of quickly assembled buildings using prefabricated reinforced concrete panels*

One of the restrictions related to the limit conditions for roofing and ribbed reinforced concrete panels for walls used for quickly-mounted buildings is the strict conditions regarding their overall dimensions. This is explained by the requirements for transporting the specified structures from factory warehouses to the construction site. However, despite these strict requirements for not exceeding the given dimensions of building structures, the manufacturing industry requires buildings to increase spans and expand the usable space inside a building (Semko et al., 2020). This problem is partially solved by carrying out the pre-mounting assembly of the individual elements delivered to the construction site into a spatial mounting unit (Faur and Mircea, 2011; Xiang et al., 2022).

One practical example of such structures is steel-reinforced concrete structures. The creation of these structures is based on the principle that each of the elements used is in its most favourable working conditions, namely, concrete in compression and metal in tension (Venglar et al., 2018). A typical spatial structure of the coating is a spatial cable-stayed steel-reinforced concrete structure, which consists of three-dimensional modules composed of a reinforced concrete slab and steel rods (Gasii, 2014). In addition to the modules, the structures created include steel rod elements of a lower belt, which only perceives tensile forces.

1.2 Highlighting the unresolved part of the specified problem

Prefabricated units of the steel-reinforced spatial concrete structures of long-span coatings at the stages of transportation, mounting, installation, and operation work according to various calculation schemes. This is explained by the imposition or destruction of individual boundary conditions (connections) or a change in the type of these connections at each of the specified stages (Semko et al., 2020; Sococol et al., 2021). Therefore, during the calculation of the structures considered, it is necessary to consider the so-called constructive nonlinearity of their work.

1.3 The purpose and tasks of the work

The purpose of the research is to determine the possibility of using typical ribbed reinforced concrete covering slabs to create a combined long-span triangular reinforced concrete covering system with a steel brace (see Fig. 2).

To solve the set purpose, based on the results of already conducted studies (Gomon et al., 2022; Semko and Hasenko, 2022; Sucharda and Konecny, 2018), the research task of this work was formulated, namely:

– to investigate the constructive nonlinearity of ribbed reinforced concrete covering slabs during the transportation, mounting, installation, and operation of the combined spatial covering panel;
– to identify the effect of and to develop a rational design of nodes connecting individual prefabricated units into a spatial structure, with the help of which it is possible to create unloading support moments, which will reduce the internal forces in the design cross-sections;
– to investigate the effect of the effective width of reinforced concrete slab shelves on changes in the internal forces in the load-bearing ribs of wall and roof panels.

1.4 Practical significance of the research results

The development of prefabricated reinforced concrete structures and their implementation in construction significantly increases the level of the industrialization of buildings and structures of an industrial or public purpose.

2 MATERIALS AND METHODS

Quick-mounted buildings with a wall construction scheme are considered (see Fig. 1). The transverse frame of such a building has a clear span of 18,000 mm between the inner surfaces of the wall panels. It is proposed to use a prefabricated reinforced concrete panel as a roofing structure with overall dimensions of 2980×18,730 mm (see Fig. 2). The connection point of the roofing constructions to the wall structures is a hinged fixed support that transmits both vertical and horizontal forces. The central axis of the supporting part of the roofing structure is located at a distance 315 mm outward from the inner surface of the wall panel (from the building's working span) and 145 mm from the outer edge of the longitudinal rib of the wall panel. These two distances explain the excellent value of the roofing panel dimensions compared to the working width of the room. The height of the roof panel in the ridge (including the mounting parts) is 2536 mm (Semko and Hasenko, 2020).

The covering panel consists of two reinforced concrete ribbed slabs united into a triangular roofing structure with the help of a steel brace (see Fig. 3). The height of the longitudinal rib of the symmetrically located covering plates is 450 mm. The covering plates have built-in parts for reclining on wall panels, a brace fas-

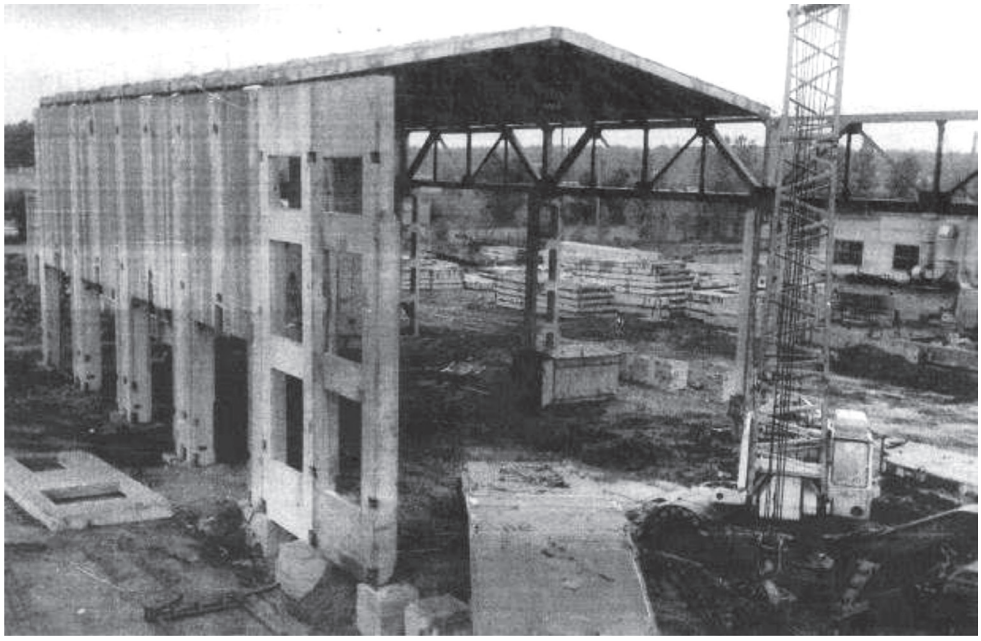

Fig. 2 *Building with the use of prefabricated reinforced concrete covering panel during installation*

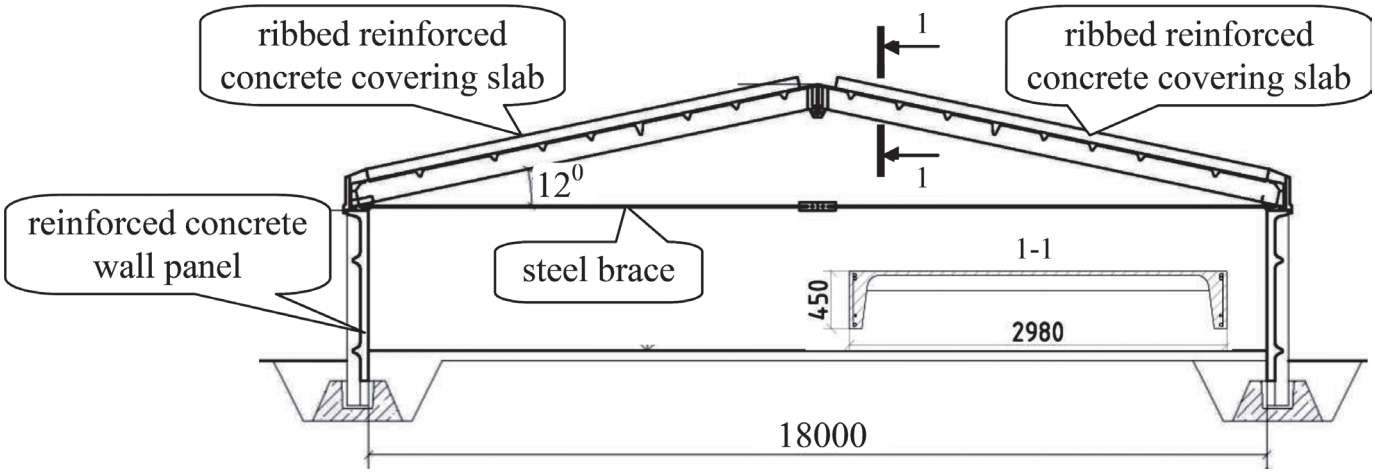

Fig. 3 *General view of the covering panel of the prefabricated reinforced concrete*

tening, and a ridge node formation to form a single hard disc of the covering.

The covering panel is transported to the construction site in the form of a set of two ribbed slabs with dimensions of 2980×9560 mm and four steel brace elements. Fig. 4 shows the scheme of the enlarging assembly of the spatial panel, the general view of which is shown in Fig. 3, from two ribbed reinforced concrete slabs and four steel brace elements. In node A of the eaves, a steel brace is attached to the ribbed slabs of the covering. In ridge node B, two ribbed plates are connected. The tightening of the brace before the installation of the roofing panel is ensured by its acceptance of the spreading force from the weight of the ribbed reinforced concrete slab. The stage of enlarging the assembly and the tensioning brace on the construction site is shown in Fig. 5.

Thus, the ribbed slabs will work according to several different calculation schemes (Semko et al., 2020), i.e.:

1. alternate installations of two ribbed reinforced concrete slabs on the mounting conductor;
2. brace tensioning from the self-weight of the ribbed reinforced concrete slabs covering and the creation of self-unloading bearing moments in the ribbed cover slabs at the hinged ridge assembly:

2.1 lifting the assembled spatial panel of the cover with a hinged ridge assembly by the two extreme mounting loops;

2.2 leaning the assembled spatial panel with a hinged ridge assembly on two extreme supports without any support on the ridge and the arrangement of a rigid comb node;

3. lifting the assembled spatial panel of the cover by the mounting loops with a rigid comb node and the brace installed after the enlarging assembly;
4. the operational position of the covering panel with a rigid comb node and brace installed on the wall panels.

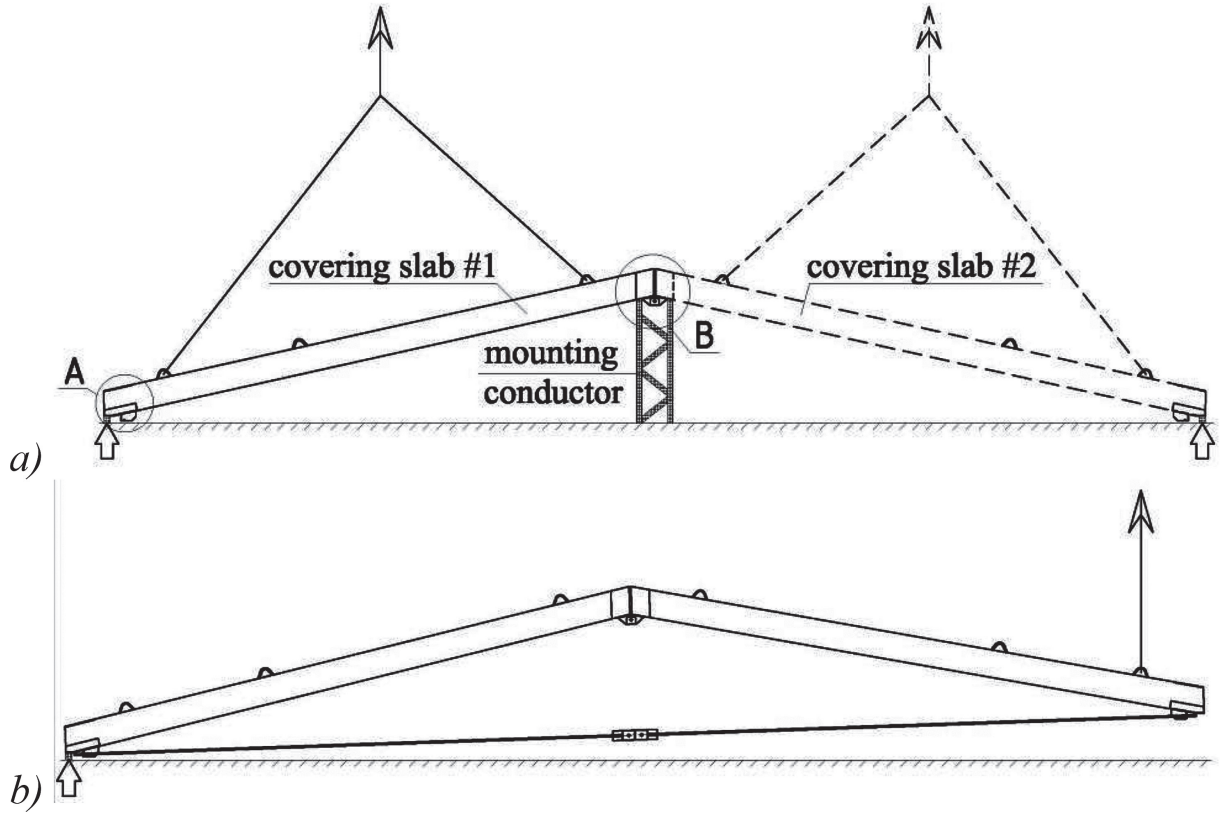

Fig. 4 *Scheme of the enlarging assembly of the covering panel: a) installation of two ribbed slabs on the conductor; b) tensioning of the steel brace*

Fig. 5 *Enlarging assembly of the covering panel and tensioning of the brace on the construction site*

3 RESULTS

3.1 General evaluation of the results obtained

On the basis of the research conducted, firstly, a rational design of the connection nodes of the precast reinforced concrete elements into a covering panel was developed, which allows for the creation of the unloading support moments; secondly, the constructively non-linear operation of the ribbed reinforced concrete slabs during the enlarging assembly of the covering panel was investigated; thirdly, the effect of the shape and dimensions of the cross-sections of the reinforced concrete roofing and wall panels calculated on any changes in their internal forces was investigated.

3.2 Development of a rational design of nodes connecting the prefabricated elements into a spatial covering panel

Usually, a ribbed reinforced concrete covering slab operates according to a single-span scheme with hinged supports. With such a calculation scheme, the maximum (calculated) value of the bending moment occurs in the middle of the span, and the moment at the supports is zero (see Fig. 7, c). As is well known, the span moment can be reduced by replacing the supports with rigid ones. In this case, the bending moment's maximum value will be on the supports and will be equal to two thirds of the bending moment's calculated value with the hinged scheme of supporting the plate and one third of the bending moment's calculated value in the middle of the span (see Fig. 10, c). Using the algorithm of reducing the span moment by creating support moments, eccentric nodes of the covering panel's mounting element connection were developed (see Fig. 6). The essence of creating eccentric connection nodes is to predict the distance e_1 between the geometric axis of the ribbed slabs and the brace axis in the eave nodes of the panel (see Fig. 6, a) and the distance e_2 between the geometric axis of the ribbed plates and the ridge joint of the combination of the two slabs (see Fig. 6, b).

3.3 Research on the constructive nonlinearity of the ribbed reinforced concrete floor slabs

Consider the process of the redistribution of the internal forces along the length of the ribbed reinforced concrete slabs.

Stage No.1 – *installation of one cover plate on the mounting conductor*. During this stage, two plates are installed alternately on the mounting conductor (see Fig. 7, a) with such calculations that it would be possible to assemble the ridge hinge and freely tighten the eave nodes. The reinforced concrete slab works as a *statically determined two-support single-span beam* (Fig. 7, b). The panel supports on the conductor are hinged. The load from the self-weight of the reinforced concrete slab is 13 kN/m (see Fig. 7, b). The maximum value of the bending moment is in the middle of the span; the fibres under tension are from the bottom of the plate; the bending moment at the supports is zero (Fig. 7, c). The heave of the panel by four mounting loops for installation on the mounting conductor is not a calculated case since, in this case, the span moment is reduced, and the moment in the places of suspension to the slings due to the small overhanging parts of the panel is negligible (see Fig. 8).

The preparation for the second stage of the enlarging assembly, i.e., the brace tension, is:

- assembly of the ridge joint of the two slabs;
- insertion of the brace's reinforcing rod into the eave nodes of the roofing panel;
- assembly of the two paired brace mounting elements into one.

After the ridge node is assembled and the brace is applied, the roof panel is ready to be tensioned by the self-weight of the two half-panels and the installation of a rigid comb node.

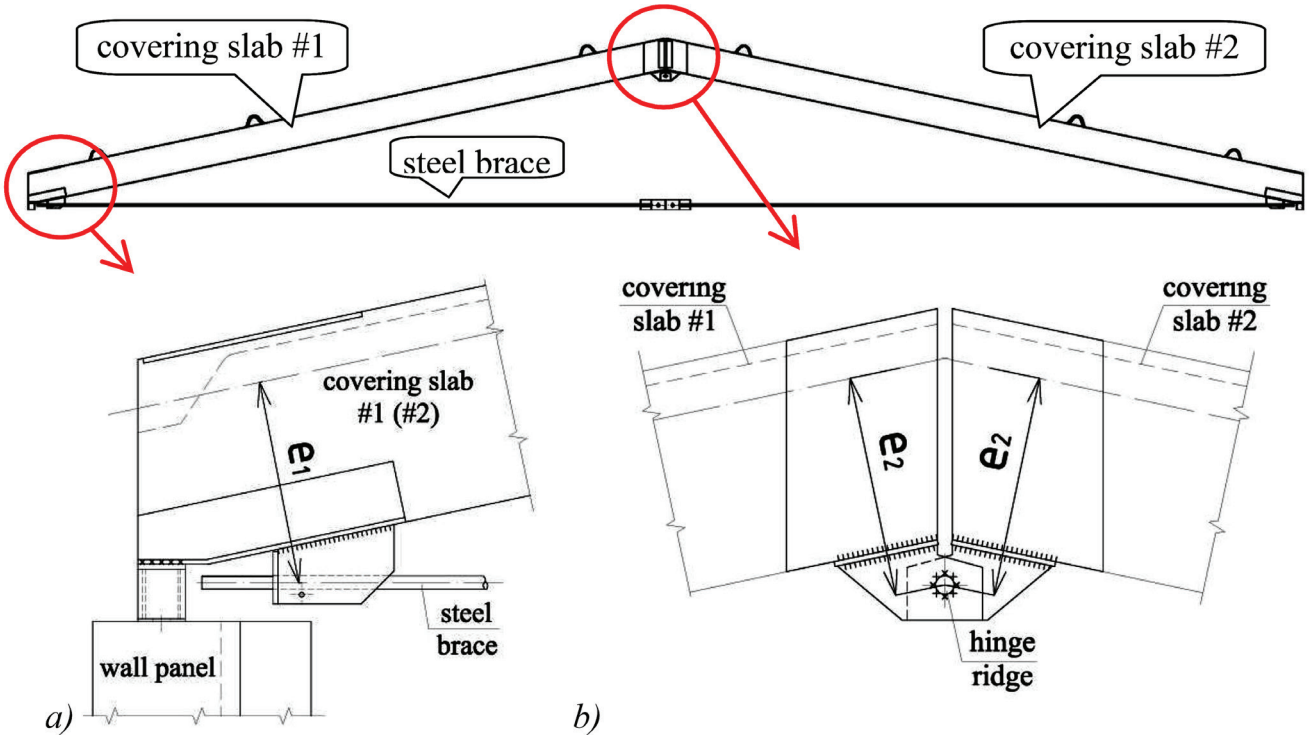

Fig. 6 *Eccentric connection of the mounting elements of the covering panel to create unloading support moments in the ribbed slabs: a) eave unit connecting the plate and the brace; b) ridge connection of two plates*

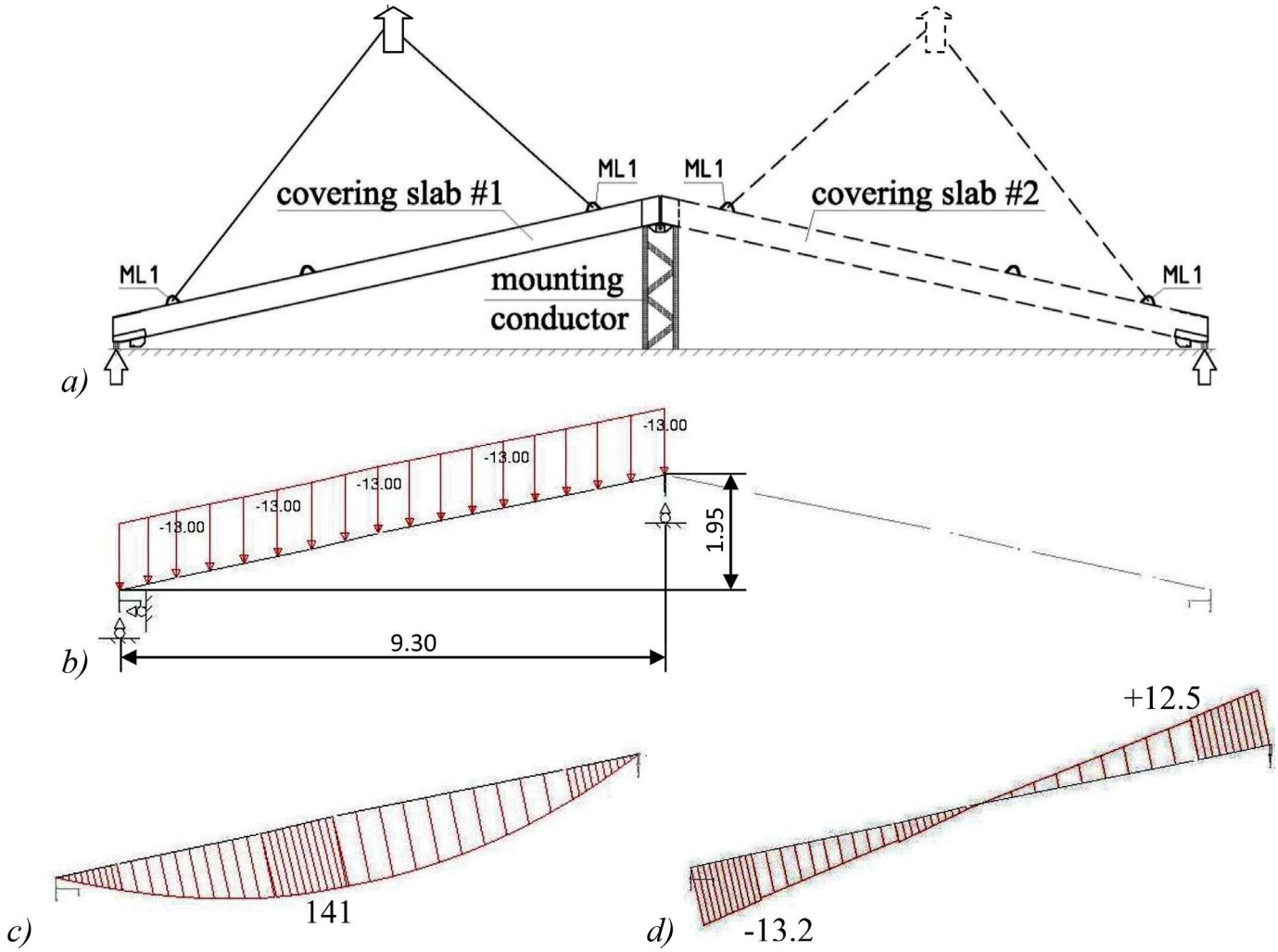

Fig. 7 *Installation of two slabs on a mounting conductor for their enlarging assembly: a) installation scheme; b) calculation scheme; c) bending moment diagram, kNm; d) axial force diagram, kN*

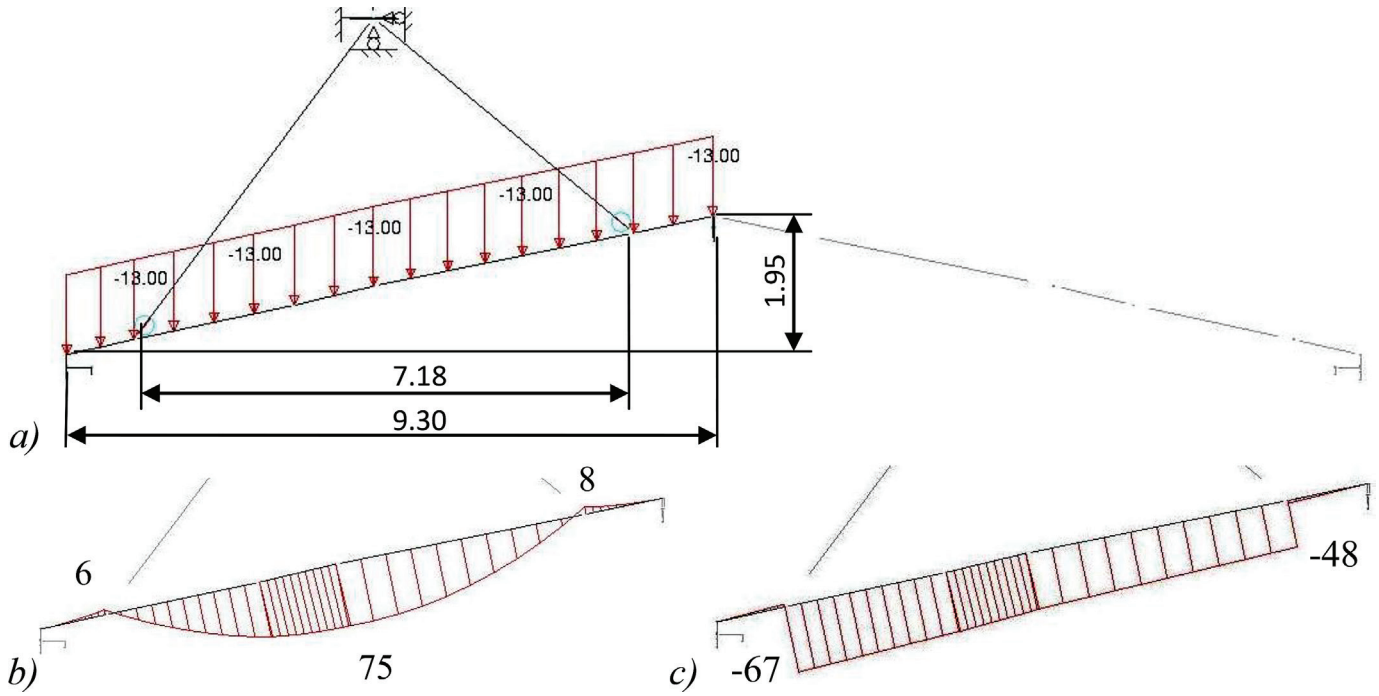

Fig. 8 *Lifting one slab by the mounting loops: a) calculation scheme; b) bending moment diagram, kNm; c) axial force diagram, kN*

Stage No.2 – *carrying out brace tensioning from the self-weight of the reinforced concrete slabs and creating self-unloading supporting moments in the slabs at the hinged ridge node*. The roof panel is raised at one end by the two extreme (closer to the supports) mounting loops ML1 (see Fig. 9, a); the mounting conductor is pulled out, and the brace is tightened at the hinged ridge node under the weight of the two plates. The load distributed along the length from the self-weight of the reinforced concrete slab is 13 kN/m (see Fig. 9, b and Fig.10, b). This is how the brace absorbs the reaction of the horizontal support from the weight of the roofing panels. Then the panel is lowered onto the extreme supports (see Fig. 10, a) without any support on the ridge. At this stage, we have a *statically determined frame with one closed circuit and three hinges*, i.e., on the ridge and at the two ends of the brace (in the places where the brace is attached to the reinforced concrete slabs).

When lifting the assembled panel with the hinged ridge node by the two extreme (closer to the supports) mounting loops ML1 (see Fig. 9, a), the maximum moment occurs on the mounting loop ML1 at a distance of 1 m from the support – the fibres under tension are on the top of the panel (see Fig. 9, c); this moment is created by the self weight of the plate console and the brace tension force (see Fig. 9, b).

When resting an assembled panel with a hinged ridge node on two extreme supports without any support on the ridge (see Fig. 10, a), the maximum moments occur at the supports of the slabs below, and the ridge fibres under tension are on the top of the panel (see Fig. 10, c). The moment on the supports is created by the brace tension force and the moment on the ridge is created by the compressive force on the upper reinforced concrete belt of the roofing system applied to the central hinge (see Fig. 10, b). These two forces (at the supports and on the ridge), which are applied with eccentricity relative to the geometric central axis of the reduced cross-section of the slab, create self-unloading support moments in the reinforced concrete slabs. After the brace tensioning, the side plates are welded onto the comb node; i.e., the node becomes rigid. The roof panel in the form of a triangular roofing system with the brace is ready for installation on the wall panels.

It should be noted that the effect of the instantaneous concrete creep from the action of the load on it will be quite insignificant; therefore, it was ignored during the analysis of the redistribution of the internal forces in the roofing system. The study of the effect of the long-term concrete creep on the redistribution of internal forces in the roofing system was not considered to be a task of these studies.

Stage No.3 – *lifting the assembled panel by the mounting loops ML2 with a hinged ridge node and installed brace*. During the installation, the roof panel is lifted by the mounting loops ML2 using a 4-branch sling or a traverse with two 2-branch slings (Fig. 11, a). Before the final lowering of the roofing panel onto the wall panel and the welding of the embedded parts, it is necessary to ensure the tensioning of the brace so that it accepts the spacer from the self weight of the reinforced concrete slabs. In this case, we have a *once statically indeterminate frame with one closed circuit and two mortised hinges* at the two ends of the brace (in the places where the brace is attached to the reinforced concrete half-panels) (Fig. 11, b). The maximum moment in the half-panels occurs at the mounting loop ML2, i.e., from above the panel (see Fig. 11, c*);*

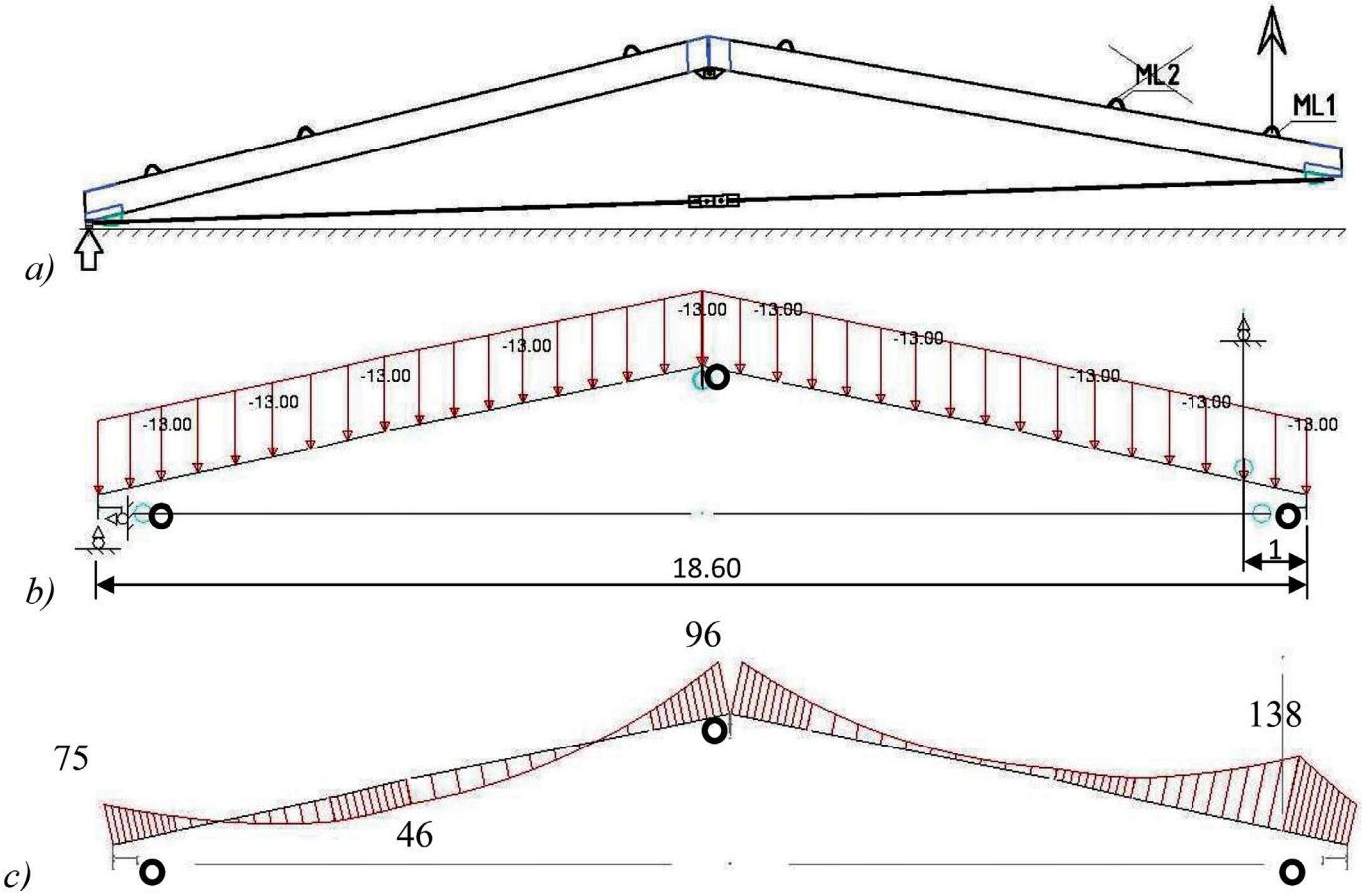

Fig. 9 *Lifting the assembled panel with a hinged ridge node by the two extreme (closer to the supports) mounting loops ML1: a) slinging scheme; b) calculation scheme; c) bending moment diagram, kNm*

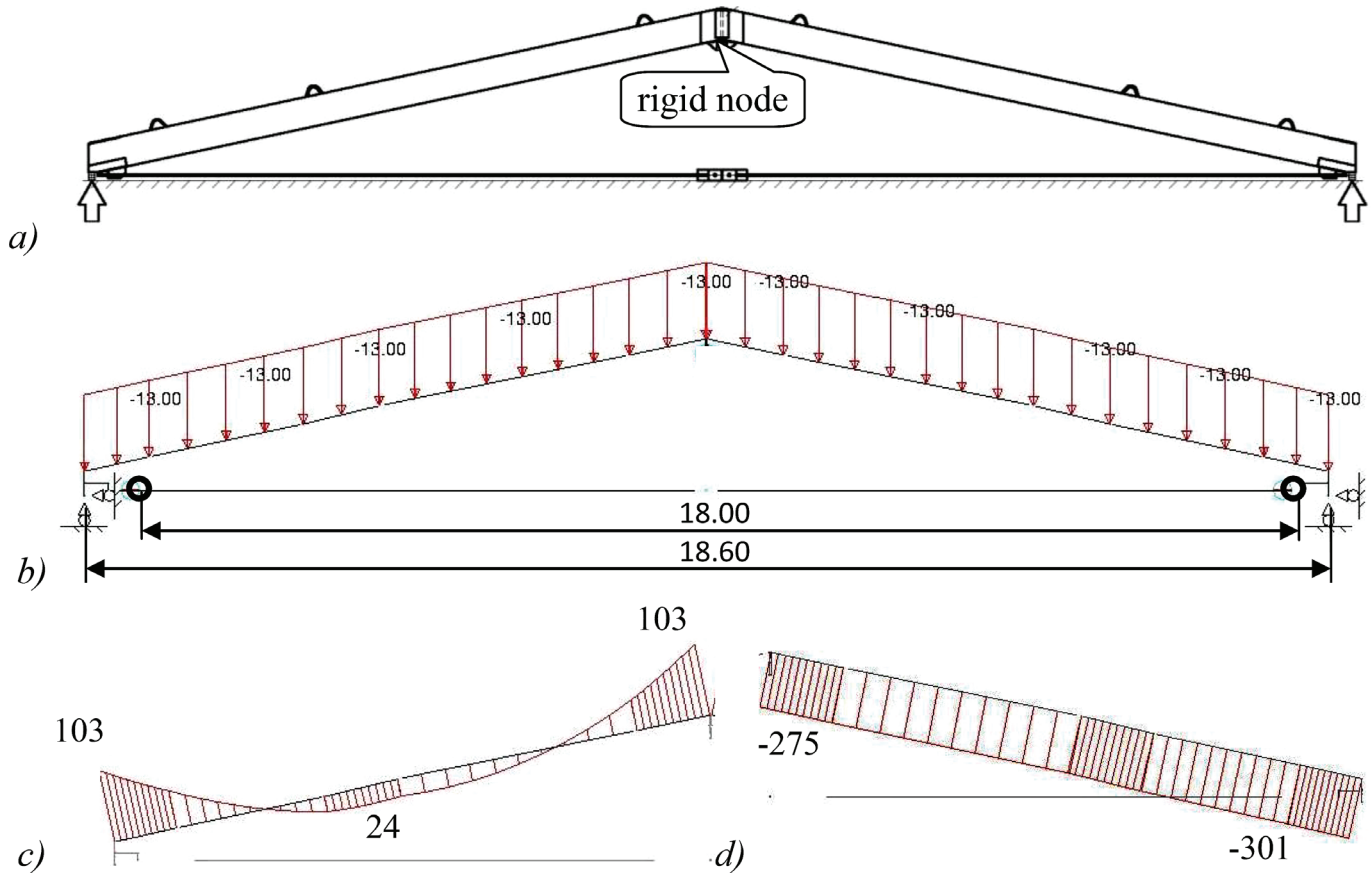

Fig. 10 *Dismantling the middle support with the hinged fixed end supports and hinged ridge node: a) layout of supports; b) calculation scheme; c) bending moment diagram, kNm; d) axial force diagram, kN*

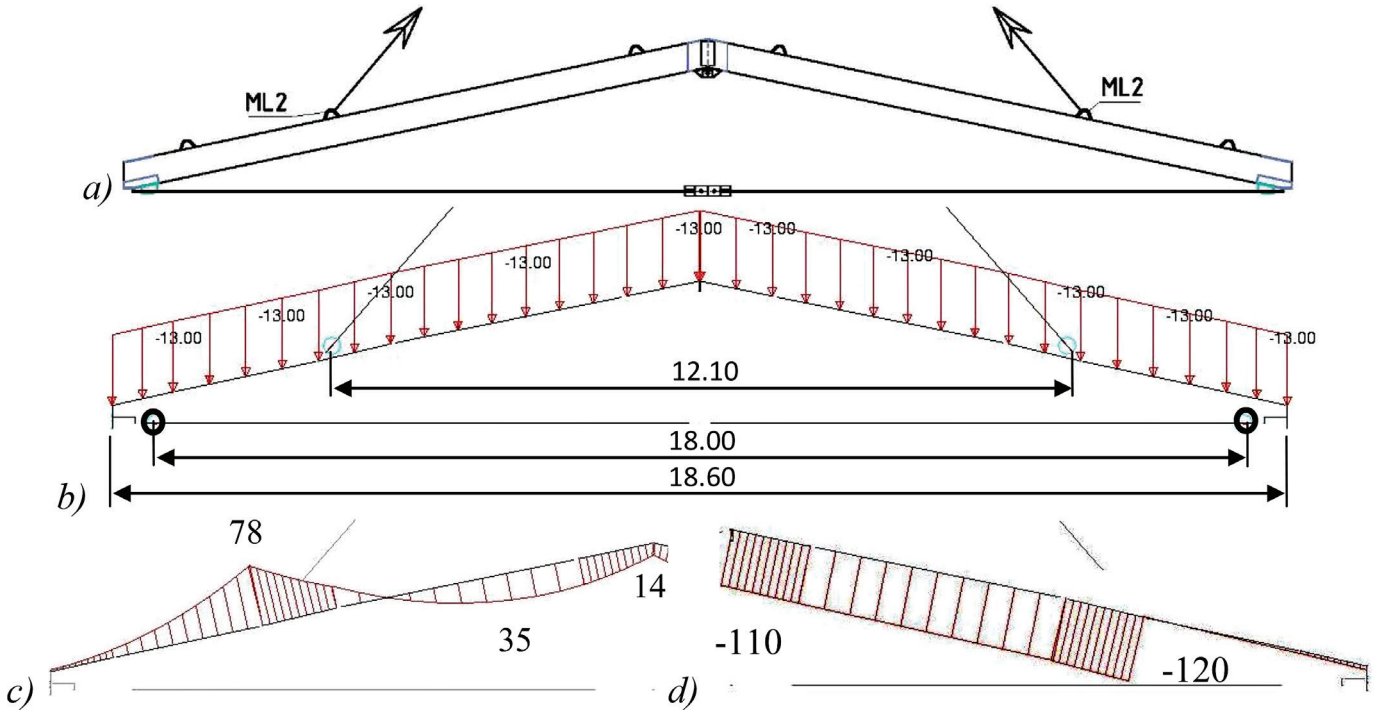

Fig. 11 *Lifting the assembled panel by the mounting loops ML2 with a hinged ridge node and installed brace: a) slinging scheme; b) calculation scheme; c) bending moment diagram, kNm; d) axial force diagram, kN*

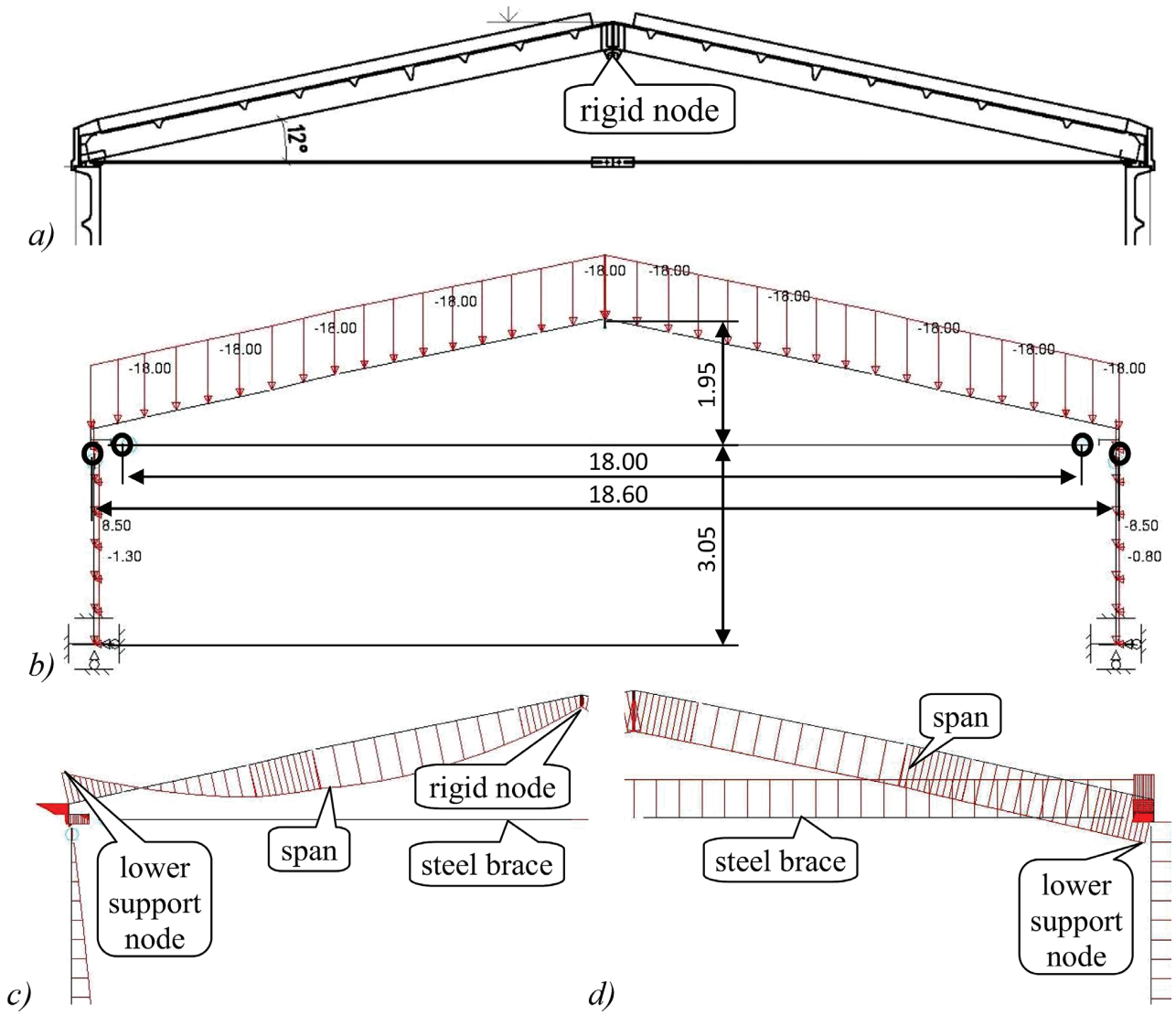

Fig. 12 *Operational position of the plate: a) schematic drawing; b) calculation scheme; c) bending moment diagram, kNm; d) axial force diagram, kN (value internal forces – Tab. 2)*

this moment is created by the self weight of the overhanging parts of the plate (see Fig. 11, b). In this case, the tension in the brace is close to zero.

Stage No.4 – *operational position of the plate (with a hinged ridge node and installed brace), taking into account the operation of the wall panels*. At this stage, we have a twice statically indeterminate frame with two closed contours and two hinges in each contour (at the sites of the brace fastened to the covering slabs for the closed contour of the triangular roof arch and at the sites of the abutment of the roofing panel on the wall panels for the lower contour). The junction of the wall panels to the foundations is taken as rigid (see Fig. 12, a).

At this stage, *taking into account the work of the shelves*, the maximum bending moment occurs: the fibres under tension are on the bottom of the slab on the span; the fibres under tension are on the top of the panel on the supports; *without taking into account the work of the shelves*, the moment in the span (the fibres under tension are on the bottom of the panel) and the moment at the supports (the fibres under tension are on the top of the panel) are practically the same (see Fig. 12, c). The moment in the span is created by the evenly distributed self weight of the panel, the weight of the light roof and any snow (the total evenly distributed vertical load in this case is equal to 18 kN/m – see Fig. 12. b), and the forces on the support (the brace tension and vertical support reaction). The moment on the supports is created by the brace tightening force, and the vertical support reaction of the panel is created from an evenly distributed load of 18 kN/m applied with eccentricity (see Fig. 12, b). The vertical load is applied to the wall panels; it is equal to the support reaction from a uniformly distributed load (the self-weight of the slabs, the structure of the light roof, and any snow).

3.4 Study of the effective width of the reinforced concrete slab shelves on any changes in the internal forces in the load-bearing ribs of the wall and roof panels

Since the walls and covering panels can contain holes in the shelves, for example, for the arrangement of a window or door openings, the use of the stiffness of two types of reinforced concrete elements is ana-

lyzed in the calculation schemes discussed above, i.e., rectangular elements, which are equal to the size of two ribs, and T-section elements, which include a shelf. The effective width of the shelf was determined according to the location of the zero bending moment points:

$$b_{eff} = b_w + 2 \cdot \left(0.2 \cdot b_i + 0.1 \cdot l_0\right), \quad (1)$$

where b_w is the width of the two edges of the plate from below;
b_i is the width of the shelf on each side of the reduced T-shaped section;
l_0 is the distance between the points of the zero bending moments on the diagram.

The combinations of the stiffness set analyzed are shown in Table 1, where they are used in the corresponding calculations. The results of the calculations (see Table 2) show that the most dangerous options for covering reinforced concrete slabs are the following options:

a) all the frame elements work by considering the inclusion of shelves (stiffness set #1 – Fig. 13, a). In this case, we have the most significant supporting moment in the g slabs – the fibres under tension are on the top of the slab (Fig. 12, c). It should be noted that the load that causes this moment is evenly distributed over the roof, without taking into account possibility of the formation of snow bags behind the aeration devices along the roof (Fig. 12, b);
b) the slab work with the inclusion of shelves in the work and wall panels without taking into account the shelves (ribs only) (stiffness set #9 – see Fig. 13, b). In this case, we have the largest span moment in the covering plates – the fibres under tension are on the bottom of the panel (see Fig. 12, c). The load that causes the formation of this moment is

Tab. 1 *Stiffness sets for the operational calculation scheme (Stage № 4)*

Stiffness set №	Left wall panel	Left covering panel	Right covering panel	Right wall panel
Set #1	**T-section**	**T-section**	**T-section**	**T-section**
Set #2	T-section	T-section	T-section	Rectangle
Set #3	T-section	T-section	Rectangle	T-section
Set #4	T-section	Rectangle	T-section	T-section
Set #5	Rectangle	T-section	T-section	T-section
Set #6	T-section	T-section	Rectangle	Rectangle
Set #7	T-section	Rectangle	T-section	Rectangle
Set #8	T-section	Rectangle	Rectangle	T-section
Set #9	**Rectangle**	**T-section**	**T-section**	**Rectangle**
Set #10	Rectangle	T-section	Rectangle	T-section
Set #11	Rectangle	Rectangle	T-section	T-section
Set #12	Rectangle	Rectangle	Rectangle	T-section
Set #13	Rectangle	Rectangle	T-section	Rectangle
Set #14	Rectangle	T-section	Rectangle	Rectangle
Set #15	T-section	Rectangle	Rectangle	Rectangle
Set #16	Rectangle	Rectangle	Rectangle	Rectangle

Tab. 2 *Internal maximum forces in the roofing slabs and brace for the operational calculation scheme (Stage No.4) (the diagram of the location of the cross-sections calculated, see Fig. 12, c)*

Stiffness set	Lower support node			Span		Ridge node			Brace
	N, kN	M,kNm	Q, kN	N, kN	M,kNm	N, kN	M,kNm	Q, kN	N, kN
Set #1	**-342**	**-116**	**89**	**-326**	**144**	**-308**	**30**	**-67**	**302**
Set #2	-354	-104	95	-336	156	-319	34	-60	310
Set #3	-373	-105	90	-354	138	-335	-14	-70	319
Set #4	-372	-105	90	-354	138	-334	-14	-70	319
Set #5	-354	-104	90	-336	156	-320	34	-71	309
Set #6	-364	-94	88	-345	142	-336	-14	-80	328
Set #7	-373	-102	89	-355	140	-336	-12	-80	331
Set #8	-385	-106	82	-357	121	-350	-23	-80	332
Set #9	**-356**	**-105**	**89**	**-338**	**160**	**-322**	**34**	**-68**	**315**
Set #10	-373	-102	89	-356	140	-336	-12	-80	328
Set #11	-375	-94	88	-355	142	-336	-14	-80	328
Set #12	-386	-101	86	-367	125	-352	-25	-68	343
Set #13	-375	-95	88	-357	142	-337	-13	-81	334
Set #14	-375	-94	88	-357	142	-337	-12	-81	335
Set #15	-386	-106	86	-367	122	-352	-22	-68	343
Set #16	-389	-101	85	-371	124	-354	**-26**	-69	**350**

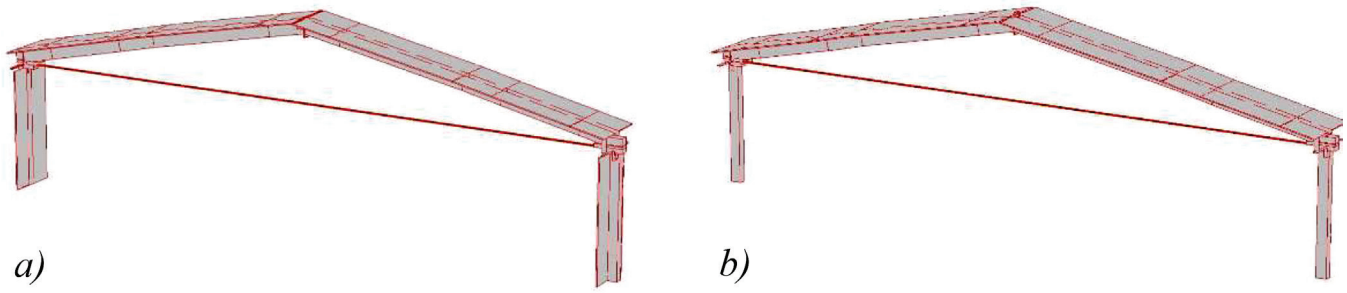

Fig. 13 *Schematic representation of the cross sections (stiffnesses) of the wall and covering panels accepted for the calculations: a) set #1; b) set #9*

unevenly distributed, taking into account the possibility of snow bags behind the aeration devices;

c) rectangular sections of the ribs (stiffness set #16) have the most minor form of inherent stiffness. We have the most significant tensile forces in the brace.

4 CONCLUSIONS

The research conducted made it possible to solve important scientific and practical issues in the development of prefabricated reinforced concrete structures that increase the level of the industrialization of buildings and structures of an industrial or public purpose.

The novelty of the development of the design of the triangular reinforced concrete covering system with steel bracing is, firstly, a study of the creation of unloading support moments to the adjacency of the steel brace in the eave nodes of the reinforced concrete slabs with eccentricity and the arrangement of a combination of the conical nodes of two reinforced concrete slabs with eccentricity; secondly, a study of the constructively nonlinear operation of ribbed reinforced concrete slabs during the enlarging installation of the spatial panel of the covering; and thirdly, a study of the effect of the shapes and sizes of the cross-sections of the reinforced concrete roof and wall panels calculated for any changes in their internal forces.

The possibility of manufacturing roofing slabs of a given span in a standard spread formwork intended for the production of serial ribbed reinforced concrete slabs with overall dimensions in a plan of 3×12 m is shown.

The structural and technological scheme of the triangular reinforced concrete roofing system with a steel brace described allows for the creation of preliminary self-stresses (stresses from its own weight) in it, namely:

1) supporting moments in the eave nodes of the reinforced concrete slabs due to an increase in the shoulder of the force pair from the brace to the neutral axis of the compressed concrete zone;
2) a zero bending moment in the ridge node due to the arrangement of the ridge hinge below the neutral axis of the compressed concrete zone and the optimal angle of the roof's slope;
3) preliminary tension of the steel brace and a significant part of its elongation even before the operational position of the structure due to the appearance of a horizontal bearing reaction in the triangular roofing system from the self weight of the reinforced concrete roofing slabs, which allows for reducing the amount of the horizontal bearing reaction from the operational load on the wall structures.

REFERENCES

Abdel-Kareem, A.H. – Abousafa, H. – El-Hadidi, O.S. (2015) *Behavior of a confined tension lap splice in high-strength reinforced concrete beams*. Slovak Journal of Civil Engineering, Vol. ***23***, No. ***3***, pp. 1-8. https://doi.org/10.1515/sjce-2015-0011

Bouzid, T. – Demagh, K. (2011) *Practical method for analysis and design of slender reinforced concrete columns subjected to biaxial bending and axial loads*. Slovak Journal of Civil Engineering, Vol. XIX, No. 1, pp. 24-32. https://doi.org/10.2478/v10189-011-0004-1

Faur, A. – Mircea, C. (2011) *Hybrid connections – the sustainable approach for prefabricated frame structures*. Proceedings of Concrete Solutions, 4th International Conference on Concrete Repair, CRC Press, pp. 227-233.

Gasii, G.M. (2014) *Technological and design features of flat-rod elements with usage of composite reinforced concrete*. Metallurgical and Mining Industry, Vol. 4, pp. 23-25.

Gomon, S. – Romanyuk, V. – Ziatiuk, Y. – Marchuk, V. – Nalepa, O. (2022) *Effective methods to strengthen the bending reinforced concrete elements*. Acta Sci. Pol., Architectura, Vol. 21 (1), pp. 51-56. https://doi.org/10.22630/ASPA.2022.21.1.6

Holly, I. – Abrahoim, I. (2020) *Connections and joints in precast concrete structures*. Slovak Journal of Civil Engineering, Vol. 28, No. 1, pp. 49-56. https://doi.org/10.2478/sjce-2020-0007

Ivanyk, I. – Vikhot, S. – Vybranets, Y. – Ivanyk, Y. (2018) *Theoretical research into spatial work of a steel-reinforced-concrete statically indeterminate combined structure.* Eastern-European Journal of Enterprise Technologies, Vol. 5/7 (95) pp. ***1***3-22. https://doi.org/10.15587/1729-4061.2018.143023

Lam, J.Y.K. – Ho, J.C.M. – Kwan, A. (2009) *Maximum axial load level and minimum confinement for limited ductility design of concrete columns*. Computers and Concrete, Vol. 6, pp. 357-376. https://doi.org/10.12989/cac.2009.6.5.357

Łotysz, S. (2016) *Reconstruction of war damaged buildings - a problem that still stands: the case of the National Economy Bank in Warsaw restored during the Second World War*. Civil and envi-ronmental engineering reports, Vol. 23(4), pp. 111-124. https://doi.org/10.1515/ceer-2016-0056

Pershakov, V.M. (2007) Каркасні будинки з тришарнірних залізобетонних рам *(Skeleton structures with three-hinged concrete frames): monograph.* K.: NAU. 301 **pp.** ISBN 978-966-2071-01-6 [in Ukrainian].

Semko, O.V. – Hasenko, A.V. (2020) *Architectural and constructive decisions of a triangular reinforced concrete arch with a self-stressed steel brace.* Zb. nauk. pr.: Tsentral′noukrayins′kyy naukovyy visnyk. Tekhnichni nauky. Kropyvnyts′kyy: KNTU, Vol. 3(34), pp. 209-217. https://doi.org/10.32515/2664-262X.2020.3(34).209-217

Semko, O.V. – Hasenko, A.V. (2022) *Classification of self-stressed steel-concrete composite structures*. Lecture Notes in Civil Engineering, Vol. 181, pp. 367-374. https://doi.org/10.1007/978-3-030-85043-2_34

Semko, O.V. – Hasenko, A.V. – Krutybich, *O.*V. (2020) Перерозподіл внутрішніх зусиль під час укрупнювальної збірки залізобетонної арки із затяжкою *(Redistribution of internal forces during the reinforcement assembly of a reinforced concrete arch with tightening)*. Abstracts of the 72nd scientific conference NUPP, pp. 106-107 [in Ukrainian].

Semko, O.V. – Hasenko, A.V. – Kyrychenko, V.A. – Sirobaba, V.O. (2020) *The rational parameters of the civil building steel frame with struts*. Lecture Notes in Civil Engineering, Vol. 73, pp. 235-243. https://doi.org/10.1007/978-3-030-42939-3_25

Shahsavar, V.L. – Tofighi, S. (2014) *Uncertainties concerning the free vibration of inhomogeneous orthotropic reinforced concrete plates*. Slovak Journal of Civil Engineering, Vol. 22, No. 3, pp. 21-30. https://doi.org/10.2478/sjce-2014-0014

Sococol, I. – Mihai, P. – Toma, I.-O. – Olteanu-Donțov, I. –Venghiac, V.-M. (2021) *Stress-strain relation laws for concrete and steel reinforcement used in non-linear static analytical studies of the moment resisting reinforced concrete (RC) frame models*. Buletinul Institutului Politehnic Din Iași, Vol. 67 (71), Nr. 1, pp. 17-29. https://doi.org/10.2478/bipca-2021-0002

Sridhar, R. – Prasad, R. (2019) *Uncertainties concerning the free vibration of inhomogeneous orthotropic reinforced concrete plates*. Slovak Journal of Civil Engineering, Vol. 27, No. 3, pp. 44-54. https://doi.org/10.2478/sjce-2019-0021

Storozhenko, L.I. – Gasii, G.M. (2014) *Experimental research of strain-stress state of ferrocement slabs of composite reinforced concrete structure elements*. Metallurgical and Mining Industry, Vol. 6(6), pp. 40-42.

Sucharda, O. – Konecny, P. (2018) *Recommendation for the modelling of 3D non-linear analysis of RC beam tests*. Computers and Concrete, Vol. 21, № 1, pp. 11-20, https://doi.org/10.12989/cac.2018.21.1.011

Tkachenko, V. – Kwilinski, A. – Klymchuk, M. – Tkachenko, I. (2019) *The economic-mathematical development of buildings construction model optimization on the basis of digital economy*. Management Systems in Production Engineering, Vol. 27, № ***2***, pp. 119-123. https://doi.org/10.1515/mspe-2019-0020

Vatulia, G.L. – Berestianskaya, S. – Opanasenko, E. – Berestianskaya, A. (2017) *Substantiation of concrete core rational parameters for bending composite structures*. DYNWIND'2017 – MATEC Web of Conferences. Vol. 107, 00044. https://doi.org/10.1051/matecconf/201710700044

Venglar, M. – Sokol, M. – Aroch, R. (2018) Ambient vibration measurements of steel truss bridges. Slovak Journal of Civil Engineering, Vol. 26, No. 4, pp. 234-239. https://doi.org/10.21595/jme.2018.20419

Xiang, L. – Xiaomeng, S. – Hamdy, M. (2022) *Optimization research on prefabricated concrete frame buildings based on the dynamic equation of eccentric structure and horizontal-torsional coupling*. Applied Mathematics and Nonlinear Sciences, Vol. 1, pp. 1-12. https://doi.org/10.2478/amns.2022.2.0158

Zielińska, M. – Grębowski, K. (2015) *Computer-aided construction at designing reinforced concrete columns as per EC*. Int. J. of Applied Mechanics and Engineering, vol. 20, No. 1, pp.183-200. https://doi.org/10.1515/ijame-2015-0013

sciendo

Slovak Journal of Civil Engineering

Vol. 31, 2023, No. 3, 24 – 33
DOI: 10.2478/sjce-2023-0017

RAISING OF EMBANKMENT OF AN ORE TAILINGS POND AND AN ANALYSIS OF ITS STABILITY

Dagmar CHROPEŇOVÁ[1], Ivan SLÁVIK[2*]

Abstract

The article presents a method for the intensification of a tailings pond. A tailings pond serves for the hydraulic storage of silt-sand waste arising during a flotation treatment and the processing of polymetallic ores. The intensification of the tailings pond consisted of raising its dam system to increase its accumulation space. The total proposed height of the tailings pond dam system after its elevation will be 60 m. The structural and shape arrangement of the dam in the dam system of the tailings pond was the result of a stability analysis of the state of the tailings pond before and after the dam system was raised. The article presents the results of experimental verifications of the geomaterial properties that form quasi-homogeneous units of the tailings pond (subsoil, dam system, and sediment) that serve as the inputs for stability analyses. New limiting and critical water levels are modelled based on the stability analysis for the intensified dam system of the tailings pond, taking into account the standard requirements for its overall stability.

Address

[1] Vodohospodárska výstavba, š.p., Technical and Safety Supervision, Bratislava, Slovak Republic

[2] Dept. of Geotechnics, Slovak University of Technology, Faculty of Civil Engineering, Bratislava, Slovak Republic

* ***Corresponding author:*** ivan.slavik@stuba.sk

Key words

- Tailings pond,
- Stability analysis,
- Dam system,
- Safety factor,
- Slip surface,
- Limiting water level.

1 INTRODUCTION

From structural and material points of view, a tailings pond is a significantly nonhomogeneous engineering structure. The non-homogeneity can be understood not only from the point of view of the different properties of the dam system materials and the sediment in the accumulation space of the tailings pond, but also from the point of view of the change in the properties of the sediment in the accumulation space of the tailings pond caused by gradual sedimentation. Taking into account the above, analysing tailing dam stability is a challenging engineering task. The credibility of the stability analysis results is contingent on the conciseness of the computational model of the tailings pond, which realistically describes not only the structural arrangement, but also the properties of the geomaterials of the tailings pond or the surrounding rock environment. The results of regular and systematic monitoring of the properties of the geomaterials of the tailings pond are decisive information for the creation of a calculation model that takes into account the structural and material composition of the tailings pond.

2 DESCRIPTION OF THE TAILINGS POND

The tailings pond analysed serves for the storage of silt sand waste generated from the flotation treatment and processing of polymetallic ores and the subsequent treatment of sewage by the sedimentation of waste sands. The tailings pond is of the valley type, with a basic loose earth dam, that is flowing but partially overflowing from the surface water. The storage of ore waste is currently permanent. The pond has been in operation since 1978 (Masarovičová et al., 2004). The tailings pond dam system consists of a base dam and elevation dams. An aerial view of the tailings pond is shown in Fig. 1, and a view of the dam system of the tailings pond is shown in Fig. 2.

Fig. 1 *The aerial view of the tailings pond*

Fig. 2 *View of the dam system of the tailings pond*

Fig. 3 *Frontal view of the base dam of the tailings pond with a gabion wall*

Fig. 4 *View of the beach of the tailings pond at the site of the last embankment*

Fig. 5 *Deposition of ore waste by the hydrocyclone*

The base dam was built by filling with local soil. Embankments are built by the upstream raising method from flotation waste (Vick, 1990). The elevation of the original ground surface at the toe of the base dam was ~ 303.0 m above sea level, and the elevation of the crest of the base dam was originally ~ 313.0 m above sea level; it later increased due to fill to an elevation of ~ 315.20 m above sea level. Currently, the base dam is filled with mine tailings at an elevation of ~ 322.00 m above sea level. The embankments were built by a hydrocyclone from sandy sediment, and their surface is covered by mine tailings. The elevation of the crest of the last embankment is ~ 355.20 m above sea level, and the elevation of the free water level in the tailings pond lake is ~ 353.90 m above sea level. At the toe of the tailings pond dam system, a gabion wall and a backfill with mine tailings were constructed to increase the overall stability of the dam system of the tailings pond. The deformations of the gabion wall are not measured but only visually monitored. The frontal view of the base dam of the tailings pond with the gabion wall is shown in Fig. 3, a view of the beach of the tailings pond at the location of the last embankment is shown in Fig. 4.

The ore waste is deposited hydraulically on the tailings pond using the hydrocyclones in Fig. 5. The drainage of the desedimented waters in the tailings pond lake is ensured by the entry openings of the collector pipe. Regulation of the water level in the tailing pond lake is performed by closing of the inlet holes. The water collected by the water intake structure and the internal drainage system is concentrated in the stilling basin located at the toe of the dam system of the tailings pond. The surface water is drained away by catchment gutters located on the left and right sides of the tailings pond.

3 PROPERTIES OF THE SUBSOIL, DAM SYSTEM AND TAILINGS SEDIMENT

The properties of the geomaterials of the subsoil, the dam system, and the sediment of the tailings pond were determined based on the results of regular survey work carried out on the tailings pond between 2000 and 2019 (Masarovičová et. al., 2000; Masarovičová et. al, 2012; Slávik et. al., 2019).

3.1 The subsoil of the tailings pond

In the immediate subsoil of the tailings pond, deluvial sediments are formed by clay of medium (CI – 4 samples) to high

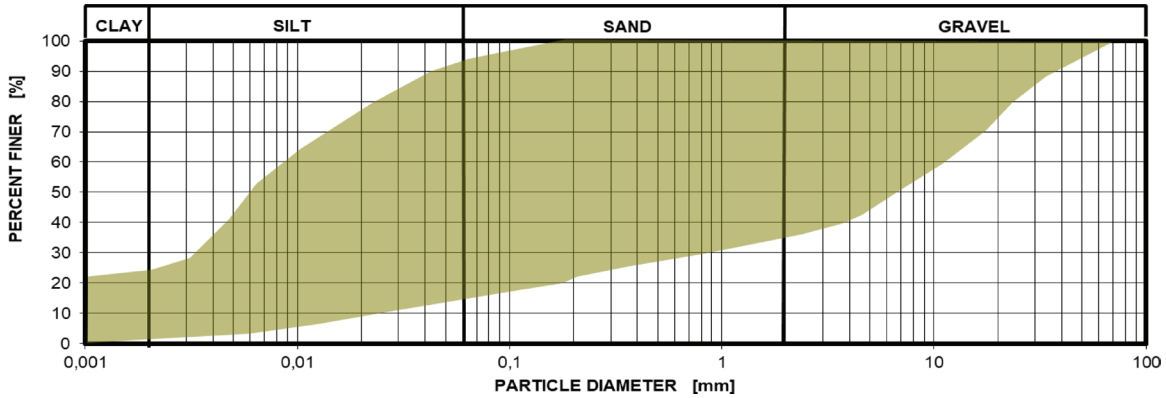

Fig. 6 *The grain size distribution of the tailing pond subsoil*

Tab. 1 *The properties of the fine-grained soil in the tailings pond subsoil*

The properties of the fine-grained soil in the tailings pond subsoil		
Parameter	**Average**	**Range of values**
γ_n [kNm^{-3}]	19.9	⟨18.8 ; 20.7⟩
w [%]	21.8	⟨6.3 ; 31.9⟩
$\mathbf{w_P}$ [%]	22.0	⟨17.8 ; 32.1⟩
$\mathbf{w_L}$ [%]	45.0	⟨35.1 ; 60.2⟩
$\mathbf{I_P}$ [%]	22.4	⟨15.5 ; 32.5⟩
$\mathbf{I_C}$ [-]	1.02	⟨0.56 ; 1.90⟩
φ_{ef} [°]	24.5	⟨21.9 ; 33.2⟩
$\mathbf{c_{ef}}$ [kPa]	21.4	⟨0.0 ; 26.5⟩

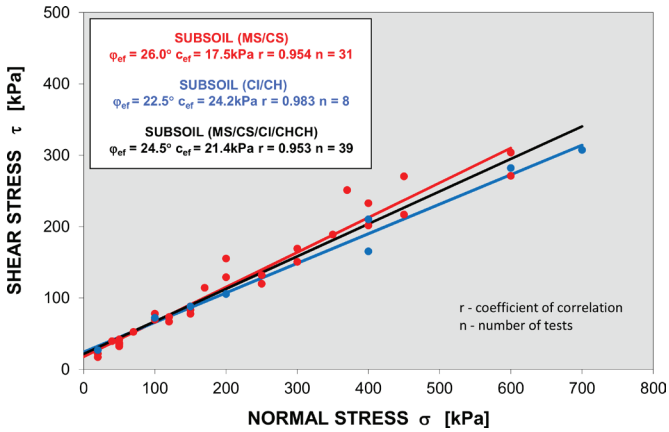

Fig. 7 *Shear strength of the fine-grained soil of the tailings pond subsoil*

plasticity (CH – 1 sample), or clay and sandy silt (CS – 11 samples / MS – 1 smaple) of a thickness of 2.5 m. Under the clayey layer, clayey gravel (GC – 2 samples) was documented with andesite boulders, respectively, and with fragments of disintegrated granodiorite. The basal layer of the subsoil of the tailings pond is formed by pyroxenic-amphibolic andesites with intense weathering. The grain size distribution of the tailing pond subsoil is shown in Fig. 6. The properties of the fine-grained soils in the tailings pond subsoil are presented in the Tab. 1. The shear strength of the fine-grained soils of the tailings pond subsoil is expressed separately for the soil group (MS/CS), the soil group (CI/CH) and for all the experimental measurements realized in Fig. 7.

3.2 Dam system of the tailings pond

The tailings pond dam system consists of a base dam with shells and two stabilization backfills (1 and 2). The body of the base dam is mainly composed of sandy clay (CS – 3 samples) and, to a lesser extent clayey gravel (GC – 1 sample). The shells of the base dam are built from gravel soil (GW – 1 sample / G-F – 1 sample). Stabilization backfill 1, which is implemented directly on the downstream slope and the crest of the base dam, is made of gravel-clay soil (GC – 2 samples / GM – 1 samples / CS – 1 sample). In order to increase the stability of the dam system at the location of the base dam, stabilization backfill 2 composed of coarse-grained gravel (GW – 2 samples / G-F – 2 samples) was implemented on top of stabilization backfill 1. The grain size distribution of the soil of the individual layers of the dam system of the tailings pond in that part of the base dam is presented in Fig. 8. The properties of the fine-grained soils of the base dam of the tailings pond are presented in Tab. 2. The shear strength of the soil of the base dam, and the stabilization backfills 1 and 2 are presented in Fig. 9.

Tab. 2 *The properties of the fine-grained soil of the tailings pond of the base dam*

The properties of the fine-grained soil of the tailings pond of the base dam		
Parameter	**Average**	**Range of values**
γ_n [kNm^{-3}]	19.5	⟨19.0 ; 19.8⟩
w [%]	25.8	⟨19.8 ; 33.5⟩
$\mathbf{w_P}$ [%]	23.4	⟨19.9 ; 29.3⟩
$\mathbf{w_L}$ [%]	52.6	⟨36.5 ; 74.8⟩
$\mathbf{I_P}$ [%]	29.3	⟨16.6 ; 45.5⟩
$\mathbf{I_C}$ [-]	0.93	⟨0.83 ; 1.01⟩
φ_{ef} [°]	20.9	⟨17.9 ; 25.9⟩
$\mathbf{c_{ef}}$ [kPa]	20.0	⟨9.7 ; 23.7⟩

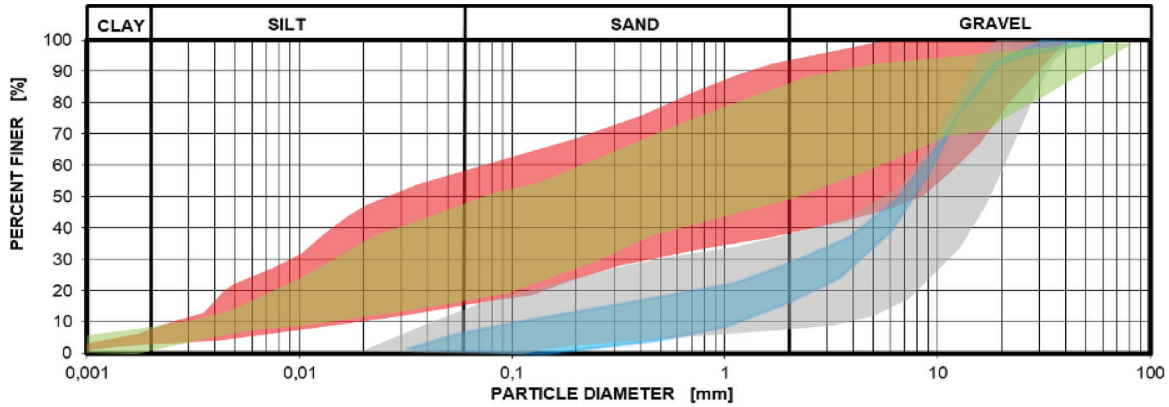

Fig. 8 *The grain size distribution of the soil of the base dam of the tailings pond*

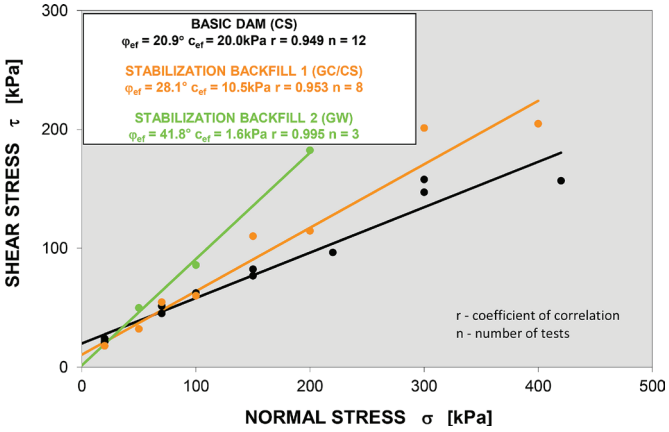

Fig. 9 *Shear strength of the soil of the base dam of the tailings pond*

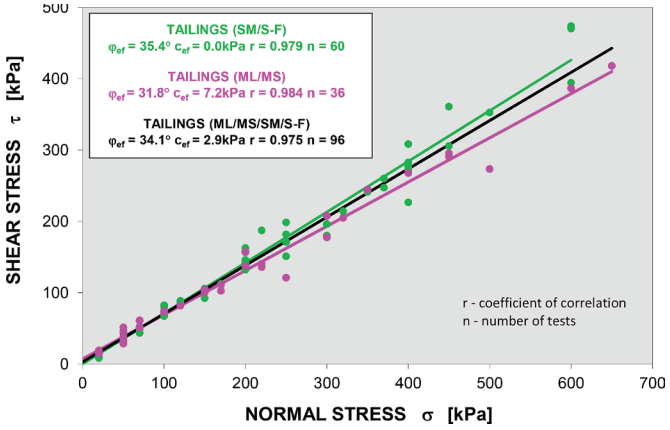

Fig. 11 *Shear strength of the tailings sediment*

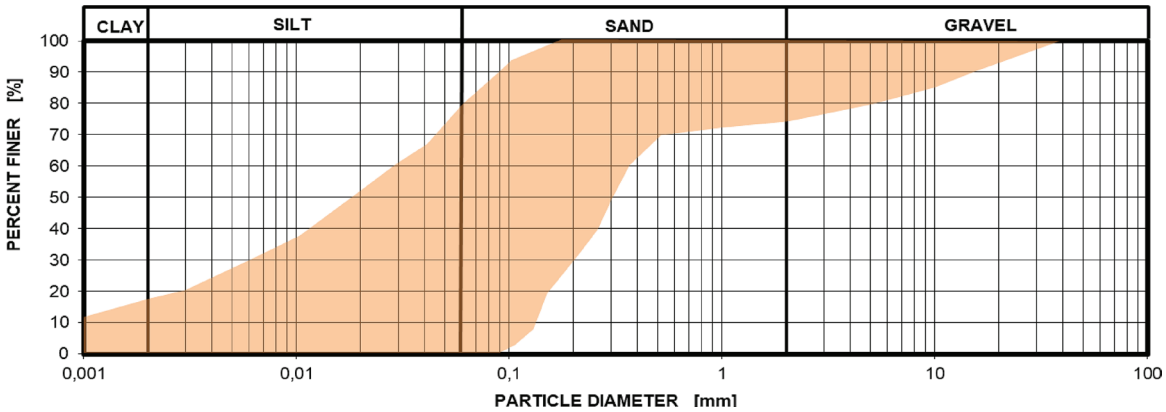

Fig. 10 *The grain size distribution of the tailings sediment*

3.3 The tailing sediment

The dam system above the base dam was built using a hydrocyclone from the coarse-grained separated part of the ore tailings that drifted. The finer part of the ore tailings, which were separated by a hydrocyclone, is floated into the storage area of the tailings pond. In terms of grain size, the sediment of the ore tailings can be characterized as silt (ML – 1 sample / MS – 8 samples) or sand (SM – 11 samples / S-F – 21 sample / SP – 4 sample). The grain size distribution of the tailings is shown in Fig. 10. The properties of the tailings sediment are presented in Tab. 3. The shear strength of the tailings sediment is expressed separately for the group of silt-type sediments (ML/MS), separately for the group of sand-type sediments (SM/S-F/SP) and separately for all the experimental measurements realized in Fig. 11. The parameters of shear strength of tailing sediment were determined by the direct shear tests (each test on 4 testing samples, dimensions 60/60/25 mm), at actuation of a normal stress 20-650 kPa and speed of direct shear testing 0,00975mm.min^{-1}.

Tab. 3 *The properties of the tailings sediment*

The properties of the tailings sediment		
Parameter	**Average**	**Range of values**
γ_n [kNm^{-3}]	20.5	⟨18.6 ; 21.8⟩
w [%]	17.4	⟨4.6 ; 28.5⟩
$\mathbf{w_P}$ [%]	18.8	⟨14.2 ; 26.8⟩
$\mathbf{w_L}$ [%]	23.0	⟨20.1 ; 36.4⟩
$\mathbf{I_P}$ [%]	4.2	⟨1.6 ; 9.6⟩
$\mathbf{I_C}$ [-]	1.04	⟨0.42 ; 1.80⟩
φ_{ef} [°]	34.1	⟨27.2 ; 38.4⟩
$\mathbf{c_{ef}}$ [kPa]	2.9	⟨0.0 ; 16.3⟩

4 STABILITY ANALYSIS OF THE TAILINGS POND BEFORE INTENSIFICATION

The tailings pond is of the valley type. For this reason, the most unfavourable valley profile of the tailings pond was selected for the stability analysis. The valley profile of the tailings pond is presented in Fig. 12. The shear strength parameters of the geomaterials are decisive for the stability analysis of the tailings pond. These parameters were determined by experimental measurements (direct shear tests, each test on 4 testing samples, dimensions 60/60/25 mm) and expressed as average shear strength parameters by a regression analysis for the fine-grained soil of the subsoil, the soil of the base dam, the soil of the stabilization backfills 1, 2 of the base dam, and the tailings sediment (Slávik et. al, 2019). For the coarse soil of the subsoil and the soil of the base dam shell, the shear strength parameters were expressed at the level of an expert estimation based on their grain size composition and the results of the experimental testing mentioned in (Stacho, J. – Sulovská, M., 2022). The resulting

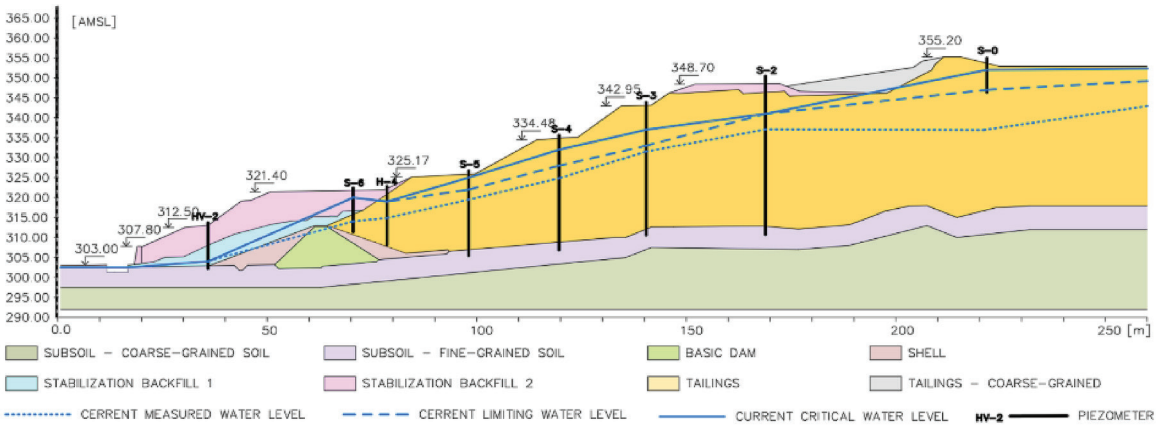

Fig. 12 *Schematic valley profile of the tailings pond before its intensification*

Tab. 4 *The parameters of the geomaterials considered in the stability analysis*

Geomaterial parametres	SUBSOIL coarse-grained soil	SUBSOIL fine-grained soil	BASIC DAM	SHELL	STABILIZATION BACKFILL 1	STABILIZATION BACKFILL 1	TAILINGS	TAILINGS coarse grained
γ_n [kN.m^{-3}]	19.5	20.0	19.5	20.0	20.0	20.0	20.5	20.0
γ_{sat} [kN.m^{-3}]	20.5	21.0	20.5	21.0	21.0	21.0	21.5	21.0
φ [°]	32.0	24.0	20.0	35.0	28.0	40.0	33.0	35.0
c [kPa]	10.0	21.0	20.0	0,0	10.0	0.0	0.0	0.0

parameters of the geomaterials considered in the stability analysis of the tailings pond are presented in Tab. 4.

Another important parameter that significantly affects the stability of a tailings pond is the position of the water level in its body. The stability analysis of the tailings pond was carried out assuming the maximum water level measured in the observation probes of the valley profile as a part of the regular monitoring, the simultaneously valid limiting level, and the simultaneously valid critical water level in the body of the tailings pond (Chropeňová, 2022). The limiting water level is the expected limit water level and the critical water level is level whose occurrence causes concern about the safety of the tailings pond (Vyhláška č. 119/2016 Z.z.). The limiting and critical water levels are determined by stability analysis. The three water levels considered are presented in the valley profile of the tailings pond in Fig. 12. According to EN 16907-7 all material parameters, partial factors, and stability shall be compliant with good practice and meet standard national and international criteria. Assessment of the overall stability of tailings pond comply with STN EN 1997-1, it is recommended that this is undertaken using Design Approach 3. In the stability analysis of the tailings pond, the effect of the seismic load corresponding to the normative seismic load of the given locality is also considered (STN EN 1998-1 Eurocode 8). According to a map of the seismic loading areas on the territory of Slovakia, the tailings pond region belongs to an area of seismic acceleration with a value of a_{gR} = 0.63 m.s^{-2}. The seismic effects are accepted in the calculations by means of the horizontal acceleration factor K_h = 0.07.

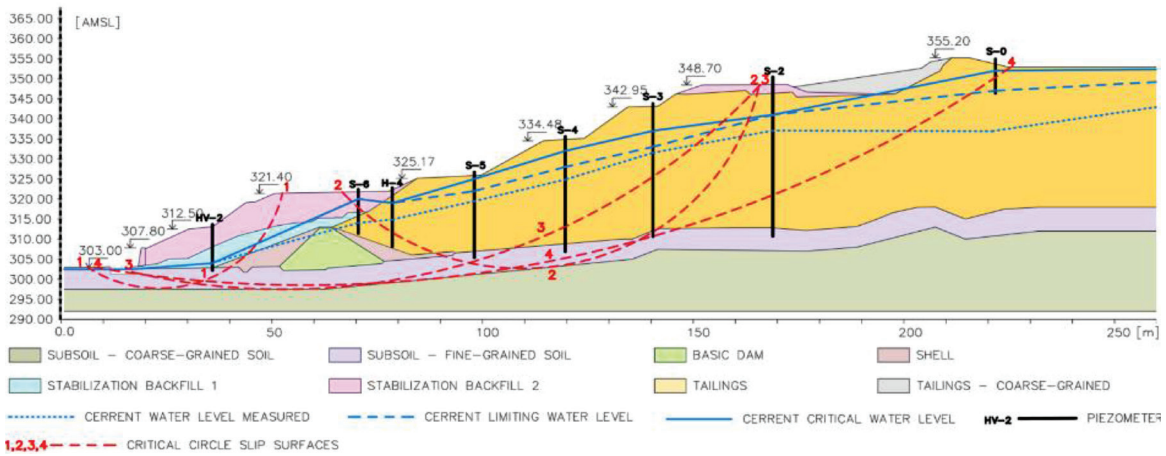

Fig. 13 *The critical circle slip surfaces – pre-intensification state*

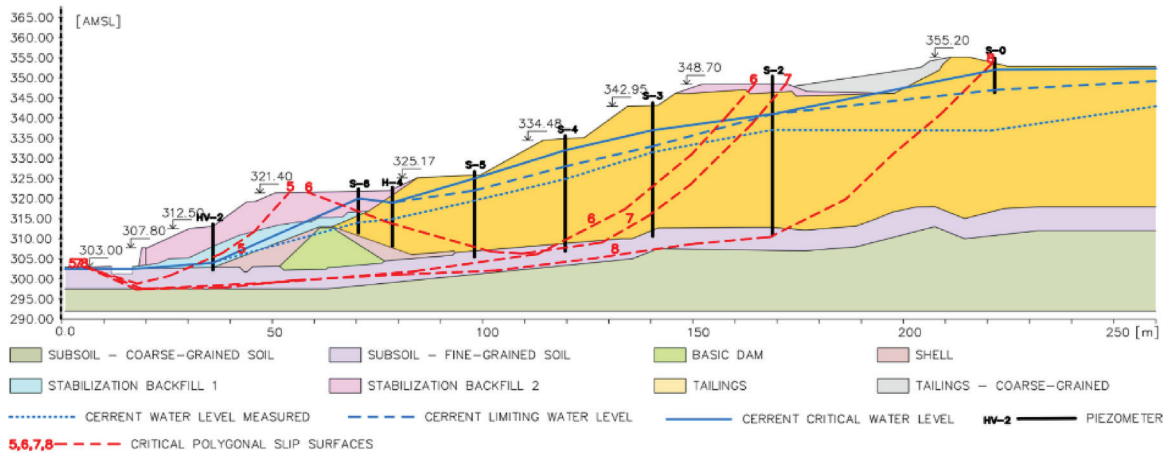

Fig. 14 *The critical polygonal slip surfaces – pre-intensification state*

Tab. 5 *Safety factors (F_S) – pre-intensification state*

Safety factors (F_S) – pre-intensification state			
Case considered	**Bishop, Spencer** (circle slip surfaces)	**Sarma, Spencer** (polygonal slip surfaces)	$F_{s,min}^{*}$
Current measured water level without seismicity	⟨1.65 ; 2.19⟩	⟨1.55 ; 2.12⟩	1.5
Current measured water level with seismicity	⟨1.39 ; 1.88⟩	⟨1.33 ; 1.77⟩	1.1
Current limiting water level without seismicity	⟨1.61 ; 2.04⟩	⟨1.54 ; 1.95⟩	1.5
Current limiting water level with seismicity	⟨1.30 ; 1.76⟩	⟨1.25 ; 1.63⟩	1.1
Current critical water level without seismicity	⟨1.52 ; 1.95⟩	⟨1.45 ; 1.80⟩	1.3
Current critical water level with seismicity	⟨1.23 ; 1.69⟩	⟨1.19 ; 1.51⟩	1.1

Note : *Required safety factor (F_S) according to standards (STN 75 3310, 1991)

The stability analysis was carried out in two phases (Slávik et al., 2019). In the first phase, the condition of the tailings pond before intensification was assessed with the level of the last embankment at 355.20 m above sea level. In the second phase, the method of intensification of the tailings pond was proposed to rise to a level of 363.00 m above sea level. For the stability analysis, the software system GEO (2021), which uses the limit equilibrium methods of (Bishop, 1959; Spencer, 1967) (circle slip surfaces) and methods of (Sarma,1973; Spencer,1967) (polygonal slip surfaces), was applied. The stability analysis of the entire tailings pond is performed per its parts, i.e., the toe and centre of the dam system and the entire dam system. For the most unfavourable valley profile of the tailings pond and its individual parts as defined, a set of circular and polygonal slip surfaces was optimized, the most unfavourable of which (the critical slip surfaces) are depicted in the profile of the tailings pond in Fig. 13 (the critical circle slip surfaces) and Fig. 14 (the critical polygonal slip surfaces). An overview of the results of the stability analysis of the tailings pond dam system, as expressed in intervals of safety factors (F_S) together with standard requirements (STN 75 3310, 1991), is presented in Tab. 5.

5 THE METHOD OF INTENSIFICATION OF THE TAILINGS POND

The intensification of the tailings pond consisted of a proposal to elevate the tailings pond dam system to a level of 363.00 m above sea level. Modelling the shape of the embankment from the current crest level of the dam system, i.e., 355.20 m above sea level to the level of 363.00 m above sea level, was gradually implemented in several steps. The condition was to preserve the current general slope of the dam system (~ 1:3) and, at the same time, to meet the standard requirements for the stability of the dam system of the tailings pond (STN 75 3310, 1991). The final shape of the proposed elevation of the dam system of the tailings pond is shown in Fig. 15. The dimensional parameters of the embankment of the tailings pond are clear from its cross section in Fig. 16. With a cross-sectional area of the embankment of 330 m^2 and a total length of 310 m, 102,300 m^3 of material will be needed to build the embankment. Coarse-grained sand obtained from the hydromix during the floating of the tailings to the hydrocyclone tailings pond was proposed for the construction of the embankment. The results of the shear strength parameters of the coarse-grained sand washed by hydrocyclones as determined by the shear box test are presented in Fig. 17.

6 STABILITY ANALYSIS OF THE TAILINGS POND AFTER INTENSIFICATION

The proposed elevation of the tailings pond dam system was analysed using a procedure identical to the stability assessment of the tailings pond before intensification. For the proposed elevation of the dam system, a new limiting and critical water level was modelled in the tailings pond by the stability analysis to ensure that the levels meet the standard requirements for the stability of the tailings pond. The new limiting and critical water levels in the

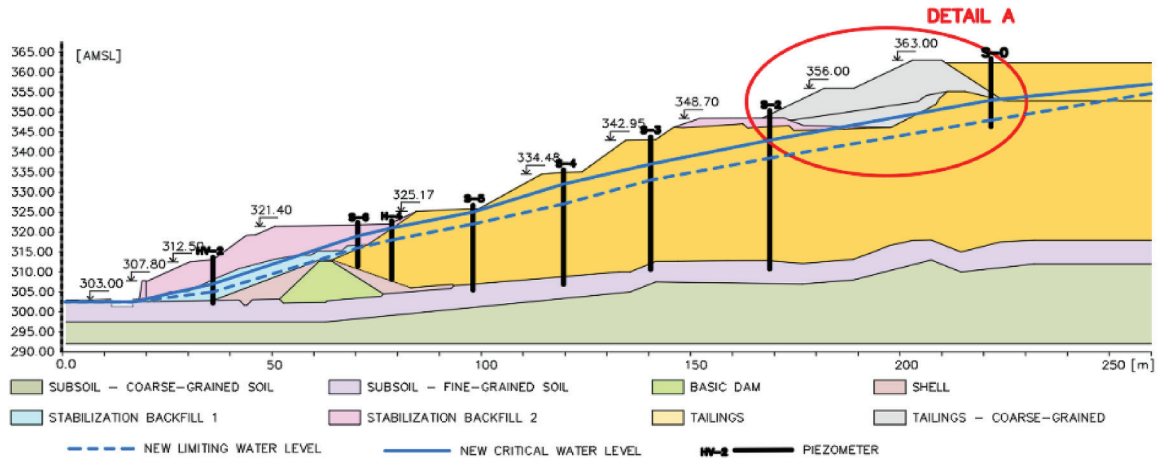

Fig. 15 *Schematic valley profile of the tailings pond after its intensification*

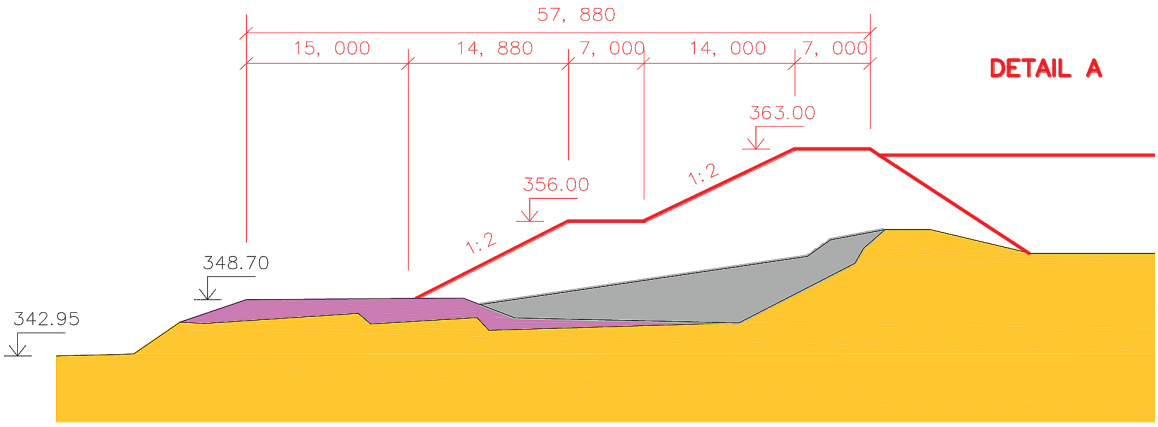

Fig. 16 *Cross section of the embankment and its dimensional parameters*

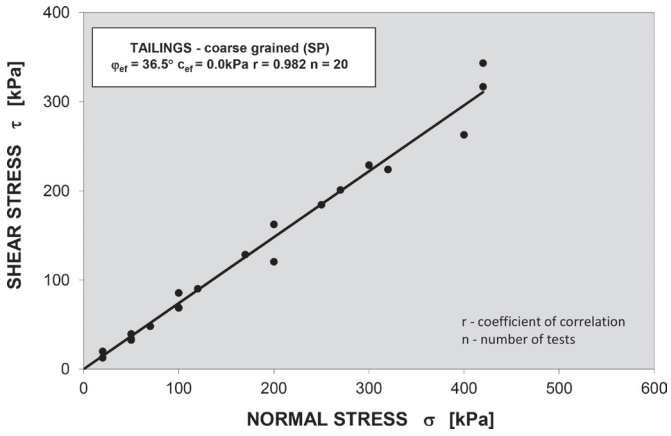

Fig. 17 *Shear strength of the coarse-grained tailings washed by hydrocyclones*

body of the tailings pond are shown in Figs. 18 and 19. An overview of the results of the stability analysis of the proposed elevation of the tailings pond dam system, as expressed in intervals of the safety factors (F_S) together with the standard requirements (STN 75 3310, 1991), is presented in Tab. 6. The shapes of the optimized circle slip surfaces are presented in Fig. 18 and the polygonal slip surfaces in Fig. 19.

7 CONCLUSION

Referring to the design and material composition of the tailings pond, the stability analysis of the tailings pond presented, demonstrated its sufficient safety, not only before, but also after its intensification. The summaries of the results of the stability analysis of the tailings pond, which are presented in Tab. 4 and Tab. 6, showed that the safety factors (F_S) meet the standard requirements (STN 75 3310, 1991).

Tab. 6 *Safety factors (F_S) – state after intensification*

Safety factors (F_S) – state after intensification			
Case considered	**Bishop, Spencer** (circle slip surfaces)	**Sarma, Spencer** (polygonal slip surfaces)	$F_{s,min}^{*}$
new limiting water level without seismicity	⟨1.60 ; 1.81⟩	⟨1.50 ; 1.82⟩	1.5
new limiting water level with seismicity	⟨1.28 ; 1.52⟩	⟨1.21 ; 1.52⟩	1.1
new critical water level without seismicity	⟨1.45 ; 1.65⟩	⟨1.36 ; 1.64⟩	1.3
new critical water level with seismicity	⟨1.17 ; 1.39⟩	⟨1.11 ; 1.36⟩	1.1

Note : *Required safety factor (F_S) according to standards (STN 75 3310, 1991)

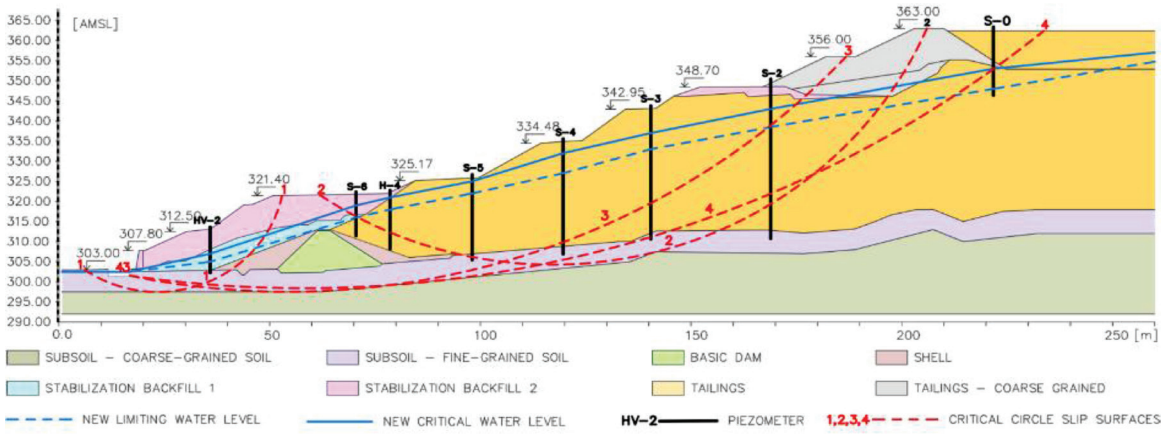

Fig. 18 *The critical circle slip surfaces – state after intensification*

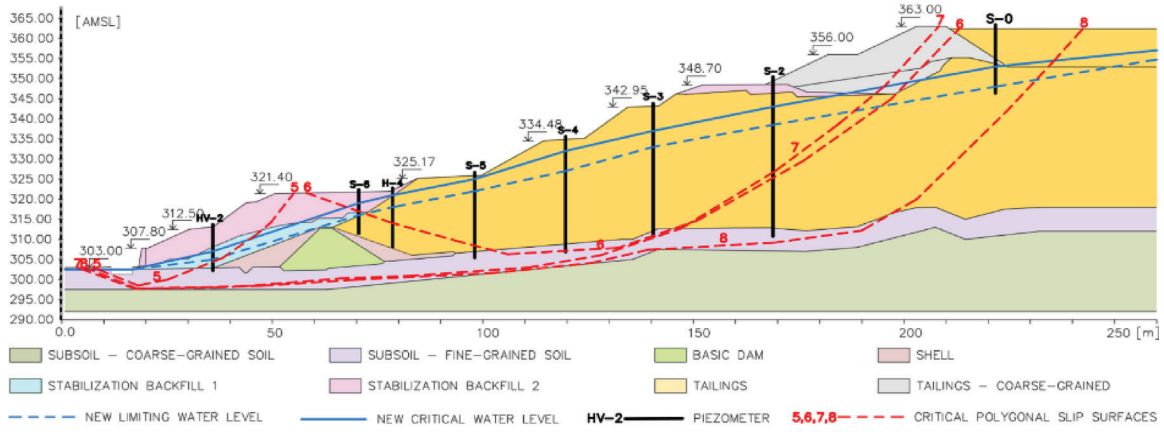

Fig. 19 *The critical polygonal slip surfaces – state after intensification*

1/ The state of the tailings pond before intensification:

- ✓ in the case of the maximum measured water level considered in the tailings pond
  $F_S = \langle 1.55 ; 2.19 \rangle$ $F_{S,min} \geq 1.5$ / seismicity $F_S^{seis} = \langle 1.33 ; 1.89 \rangle$ $F_{S,min}^{seis} \geq 1.1$
- ✓ in the case of the limiting water level considered in the tailings pond
  $F_S = \langle 1.54 ; 2.04 \rangle$ $F_{S,min} \geq 1.5$ / seismicity $F_S^{seis} = \langle 1.25 ; 1.76 \rangle$ $F_{S,min}^{seis} \geq 1.1$
- ✓ in the case of the critical water level considered in the tailings pond
  $F_S = \langle 1.45 ; 1.95 \rangle$ $F_{S,min} \geq 1.3$ / seismicity $F_S^{seis} = \langle 1.19 ; 1.69 \rangle$ $F_{S,min}^{seis} \geq 1.1$

2/ The state of the tailings pond after intensification:

- ✓ in the case of the new limiting water level modelled in the tailings pond
  $F_S = \langle 1.50 ; 1.82 \rangle$ $F_{S,min} \geq 1.5$ / seismicity $F_S^{seis} = \langle 1.21 ; 1.52 \rangle$ $F_{S,min}^{seis} \geq 1.1$
- ✓ in the case of the new critical water level modelled in the tailings pond
  $F_S = \langle 1.36 ; 1.65 \rangle$ $F_{S,min} \geq 1.3$ / seismicity $F_S^{seis} = \langle 1.11 ; 1.39 \rangle$ $F_{S,min}^{seis} \geq 1.1$

Tailings ponds are engineering structures, the shape and material parameters of which change over time and in space. They represent an environmental burden for both the present and the future; the solution to their issues must be gradual and systematic in order to reduce the possibility of accidents to a minimum. The safety of a tailings pond is expressed on the basis of its stability analysis. Assessing the stability of a tailings pond is a difficult task due to its non-homogeneity. The quality of a stability analysis is conditioned by the accuracy of the computational model of the tailings pond, which must not only realistically describe the structural arrangement, but also the properties of the geomaterials of the tailings pond´s construction and the surrounding rock massif. The properties of a tailings pond´s geomaterials forming quasi-homogeneous units (subsoil, dam system, and tailings pond sediment) and expressed on the basis of experimental verifications are the basic input for creating a computational model of a tailings pond.

REFERENCES

Bishop, A.W. (1959) *The Use of the Slip Circle in the Stability Analysis of Slopes*. Geotechnique 5, pp. 7-17.

Chropeňová, D. (2022) *Vodná stavba Odkalisko Hodruša – Hámre, Etapová správa o TBD za obdobie od 01.01.2020 do 31.12.2021 (Tailings pond Hodruša – Hámre, Stage report on TBD for period from 01.01.2020 to 31.12.2021)*. Vodohospodárska výstavba, š.p. Bratislava, 88 pp.

Masarovičová, M. – Slávik, I. – Jesenák, J. (2000) *Geotechnické posúdenie odkaliska Slovenská Banská s.r.o. Hodruša – Hámre (Geotechnical assessment of the Slovenská Banská s.r.o. Hodruša – Hámre tailings pond).* STU Bratislava, 68 pp.

Masarovičová, M. – Slávik, I. – Jesenák, J. (2004) *Komplexný monitoring odkalísk SR* – časť *2 (Comprehensive monitoring of Slovak tailings pond – part 2).* STU Bratislava, 43 pp.

Masarovičová, M. – Slávik, I. – Martinka, L. (2012) *Geotechnické informácie pre posúdenie stability odkaliska Hodruša – Hámre (Geotechnical information for assessing the stability of the Hodruša – Hámre tailings pond)*. STU Bratislava, 62 pp.

Sarma, S.K. (1973) *Stability analysis of embankments and slopes.* Geotechnique 23, pp. 423 – 433.

Slávik, I. – Stacho, J. – Suchánecková, E. (2019) *Experimentálny výskum vlastností geometeriálov a optimalizačný výskum tvaru hrádzového systému odkaliska Hodruša – Hámre (Experimental research on the properties of geomaterials and optimization research on the shape of the Hodruša – Hámre tailings pond dam system)*. STU Bratislava, 129 pp.

Spencer, E. (1967) *Method of Analysis of the Stability of Embankments Assuming Parallel Inter-Slice Forces*. Geotechnique 17, pp. 11-26.

Stacho, J. – Sulovska, M. (2022) *Shear Strength Properties of Coarse-Grained Soils Determined Using Large-Size Direct Shear Test.* Civil and Environmental Engineering, Vol. 18, Issue 1, pp. 244-257, DOI: 10.2478/cee-2022-00

Vick, S.G. (1990) *Planning, Design, and Analysis of Tailings Dams.* BiTech Publishers LTD, Vancouver, B.C. Canada, ISBN 0-921095-12-0, 369 pp.

GEO (2021) *User guide manual* – FINE – Civil Engineering Software.

EN 16907-7 *Earthworks - Part 7: Hydraulic placement of extractive waste*

STN EN 1997-1 *Eurocode 7 Geotechnical design. Part 1: General rules*

STN EN 1998-1 *Eurocode 8 Design of structures for earthquake resistance - Part 1: General rules, seismic actions and rules for buildings.*

STN 75 3310 (1991) – *Odkalisko (Tailings pond).*

VYHLÁŠKA č. 119/2016 Z.z. *Ministerstva* životného *prostredia Slovenskej republiky from 22. februára 2016, ktorou sa ustanovujú podrobnosti o výkone odborného technicko-bezpečnostného dohľadu nad vodnými stavbami a o výkone technicko-bezpečnostného dozoru (Decree No. 119/2016 Ministry of Environment of the Slovak Republic 22.2.2016, which establishes details on the performance of professional technical and safety supervision over water structures and on the performance of technical and safety supervision)*

sciendo

Slovak Journal of Civil Engineering

Vol. 31, 2023, No. 3, 34 – 42
DOI: 10.2478/sjce-2023-0018

ASSESSMENT OF THE PROBABILITY OF EXCEEDING THE LIMITING DEFORMATIONS OF A BUILDING FOUNDATION

Oksana KICHAIEVA[1,2*], Dietmar ADAM[2]

Abstract

The level of ground settlement under the effect of certain factors is one of the markers indicating the adequacy of adopted design solutions. By comprehending settlement values, it is possible to infer the degree of risk associated with a project and, if necessary, introduce changes to the design. The concept of reliability management here manifests itself in the timely adjustment of the decisions made, while it is necessary to use the procedure of the quantitative assessment of the probability of the occurrence of a particular limit state. A qualitative assessment indicates only the limits of an area, which approximately characterizes the effects of changes in the geotechnical situation. In this article, a method for determining the probability of exceeding the limit deformation of a building-base massif using the Monte Carlo statistical method is developed, and an algorithm and computer program implementing the proposed calculation method are created.

Address

[1] Dept. of Geotechnics, Underground Structures and Hydrotechnical Construction, O. M. Beketov National University of Urban Economy in Kharkiv, Kharkiv, Ukraine

[2] Institute of Geotechnics, TU Wien, Vienna, Austria

* ***Corresponding author:*** o_kichaieva@ukr.net

Key words

- Settlements,
- "Building – base" system,
- Monte Carlo method,
- Reliability, Probability.

1 INTRODUCTION

1.1 Statement of the problem in general terms

The Eurocode design concept (EN 1990) is adopted as the Partial Factor Design concept. This approach takes into account the variability of the initial parameters of loads and impacts on a building (structure). All the input data for a design scheme are definitely stochastic; however, in the existing approach they are replaced by deterministic averaged values. However, the coefficient approach is not always able to take into account the random nature of the many factors affecting a final assessment, as deterministic calculations are only a special case of probabilistic-statistical calculations. A deterministic calculation can only provide a single value, whereas a probabilistic calculation provides a holistic view of the possible values of the random variables.

It is obvious that a "building – base" system should be considered when taking into account the stochastic nature of the physical and geometric parameters of a whole system, as well as the random character of external influences. To calculate and design such systems, methods of probability theory, random functions and fields, as well as reliability theory should be applied; they make it possible to more adequately reflect the stochastic nature of the main design parameters, the relationship between external influences, and the strength of a structure in order to assess its safety and durability.

Therefore, the goal of this work is to develop a method for determining the probability of exceeding the limit deformation of the foundation settlement of a "building – base" system, taking into account the stochastic character of the loads, impacts and properties of soils.

1.2 Existing methods for assessing the reliability of technical systems and building structures. Monte Carlo method

A systematic description of the basic concepts of structural reliability can be found in the EN 1990 Eurocode and the international standard ISO 2394. The results of the work of a group of scientists working under the auspices of the Joint Committee on Structural Safety (JCSS) include: 1) the fundamental theoretical study "Probabilistic Model Code", which recommends the use of probabilistic

methods of the assessment of structural reliability and describes models of basic variables and probabilistic assessment methods, and 2) the document ISO 2394-1998 "General principles on reliability for structures".

ISO 2394 defines "reliability" as follows: "reliability" is the ability of a structure to meet specified requirements under specified conditions during its intended service life. Extending the term "reliability" to the "building – base" system, we note that this system must perform the functions of providing (any) needs of the population during its estimated service life and maintaining structural indicators in the specified modes of operation in the conditions of operation, maintenance and repair. The concept of the reliability of the complex system considered includes the stability of the quality indicators and the efficiency of its functioning, which depend on the reliability of the structures and systems, in our case, the preservation of the strength of any dangerous section under any possible influences (and their combination), as well as the absence of exceeding the normative values of the deformations of the building.

A defined limit state function is used to solve limit state risk problems. This function is derived from the existing (most often normative) method of solving a particular deterministic problem within the limit state methodology. In solving the problems of reliability theory, it is particularly difficult to determine the value of the risk of reaching a limit state on the basis of solving the corresponding statistical dynamics task. To solve such a problem today, the following methods are used: numerical integration techniques, Monte Carlo simulations, and First and Second Order Reliability Methods (FORM/SORM). The Monte Carlo statistical testing method (Monte Carlo Simulation) is a numerical method for solving mathematical problems based on modelling random variables and performing a significant number of statistical tests using random variables according to known distribution laws. The statistical test method is quite universal and is used to assess the reliability and safety of building structures and bases when solving reliability theory problems based on modelling random variables and constructing statistical estimates, as well as to develop possible (probable) processes or results using various random number generation methods, which are then applied to a real model.

A prerequisite for the application of the probabilistic-statistical approach in calculating the reliability of complex technical systems is the functional description and comparison of resistance and loading processes, which results in the definition of an integral function of serviceability. Loads and impacts are considered in this case through the nature of stochastic processes. In other words, probabilistic-statistical calculations of the reliability of a system are not based on partial (deterministic) values of loads, but on discrete or continuous functions of the distribution of random quantities. According to EN0, the value of the probability of reaching the limit state (the probability of structural failure) P_f can be obtained from the formula:

$$P_f = \Phi(-\beta), \quad (1)$$

where

Φ – is the cumulative distribution function of the standardised normal distribution,

β – reliability index (or safety characteristic), which may be determined by:

$$\beta = \frac{\mu_R - \mu_E}{\sqrt{\sigma_R^2 + \sigma_E^2}}, \quad (2)$$

where μ_R, μ_E, σ_R, σ_E – the first moments of the distribution (respectively, the mathematical expectations and standards of the generalised carrying capacity of the element R and the generalised force impact E).

A reliability assessment using the FORM methodology requires probabilistic calculations when formulating the safety condition in the form of $g = R - E$. This approach is based on the integral probability of the failure of the variables R and E; given that the functions R and E have a normal distribution and are not mutually correlated, the function g performance function or "safety reserve" will also have a normal distribution.

Table 1 illustrates the relationship between the safety and reliability characteristics according to ISO 2394 and EN 1990:2002 (Table C1).

Tab. 1 *Correlation between the reliability index and reliability according to ISO 2394 and EN 1990:2002*

P_f	10^{-1}	10^{-2}	10^{-3}	10^{-4}	10^{-5}	10^{-6}	10^{-7}
β	1.3	2.32	3.09	3.72	4.27	4.75	5.20

For existing structures with an expected service life of 50 years, EN 1990:2002 establishes minimum values for the reliability index for various limit states (Annex B, C) (Table B2, C2).

According to J.-A. Calgaro and H. Gulvanessian (2001), the probability of failure and its corresponding β index are only notional values that do not necessarily represent actual failure rates and that are used as operational values for code calibration purposes and comparisons of the reliability levels of structures.

The Monte Carlo method is also widely used in geotechnical engineering when considering completely different problems (Fenton and Griffiths, 2002, 2003; Chalermyanont and Benson 2004; Vu, 2018; Pereia, 2011; Misra, 2009; Roberts, 2007, etc.). Fishman (1995) and Harr (1996) decided that since no closed-form probabilistic solutions could be obtained from the elastic settlement equation, only a Monte Carlo simulation method seems to be possible. One type of failure of the building-base system can be related to exceeding the absolute or uneven base settlement (SLS) values, the assessment of which probability is proposed in this article.

Tab. 2 *Reliability classes and recommended minimum values for reliability index β*

Reliability Class	Minimum values for β					
	Ultimate limit states		Fatigue		Serviceability	
	1 year reference period	50 year reference period	1 year reference period	50 year reference period	1 year reference period	50 year reference period
RC1	5.2	4.3				
RC2	4.7	3.8		1.5 to 3.8	2.9	1.5
RC1	4.2	3.3				

2 GENERAL PROVISIONS FOR THE CALCULATION OF SETTLEMENTS ACCORDING TO THE NORMATIVE METHOD

To ensure operational suitability (serviceability limit states (SLS)), it is necessary to perform calculations to determine the deformations of the bases, the main condition of which is to limit the level of deformations enforced by regulatory documents.

In accordance with Austrian norm ÖNORM B 1997-1-2:2021-08 "Eurocode 7: Geotechnical design – Part 1-2: Spread foundations – Analysis of bearing capacity and of settlement – National specifications concerning ÖNORM EN 1997-1", the vertical deformation of foundations can be determined in two ways, whereby the formulae for determining stress are based on equations for an elastic-isotropic semi-space: 1) the addition (integration) of the stressed surface, which varies with the depth (Fig. 1); 2) calculation of any deformations using Young's modulus.

The formula for calculating deformations by the first method is as follows:

$$S = \int_0^{z_g} \frac{\sigma_{zus}}{E_s} dz \approx \int_0^{z_g} \frac{i \cdot \sigma_0'}{E_s} dz = \sum \frac{i \cdot \sigma_0'}{E_S} = \sum_i \Delta s_i ; \quad (3)$$

here

S – base settlement, which is determined, m;
E_s – modulus of elasticity, kN/m^2;
σ_{zus} – additional stress, kPa;
i – effect of coefficients for determining stress at a certain depth (Steinbrenner curves);
z_g – ultimate depth of compressible stratum, m;
σ_0' – vertical stresses in the soil, which are determined: σ_0 – $\gamma \cdot d$, kPa;
ΔS_i – settlement of soil layers located below, mm;
σ_0 – pressure under the foundation slab due to the loads applied, kPa;
d – the depth of the pit, м;
γ – specific gravity of the soil, kN/m^3.

In this case σ_z – are the normal stresses at distance z from the surface of the ground, which are determined by the formula:

$$\sigma_z = \frac{\sigma_0}{2\pi}\left[\arctan\frac{l \cdot b}{z \cdot R} + \frac{l \cdot b \cdot z}{R}\left(\frac{1}{l^2+z^2} + \frac{1}{b^2+z^2}\right)\right] = \sigma_0 \cdot i. \quad (4)$$

Here
l – length of foundation, m;
b – width of foundation, m;
z – vertical coordinate, m,

$$R = \sqrt{l^2 + b^2 + z^2}. \quad (5)$$

Moreover,

$$\sigma_0 = F_n/(b \cdot l), \quad (6)$$

where

F_n – vertical load at the level of the base of the foundation, kN.

Figure 1 shows a schematic representation of the definition of a compressible thickness consisting of several different layers of soil.

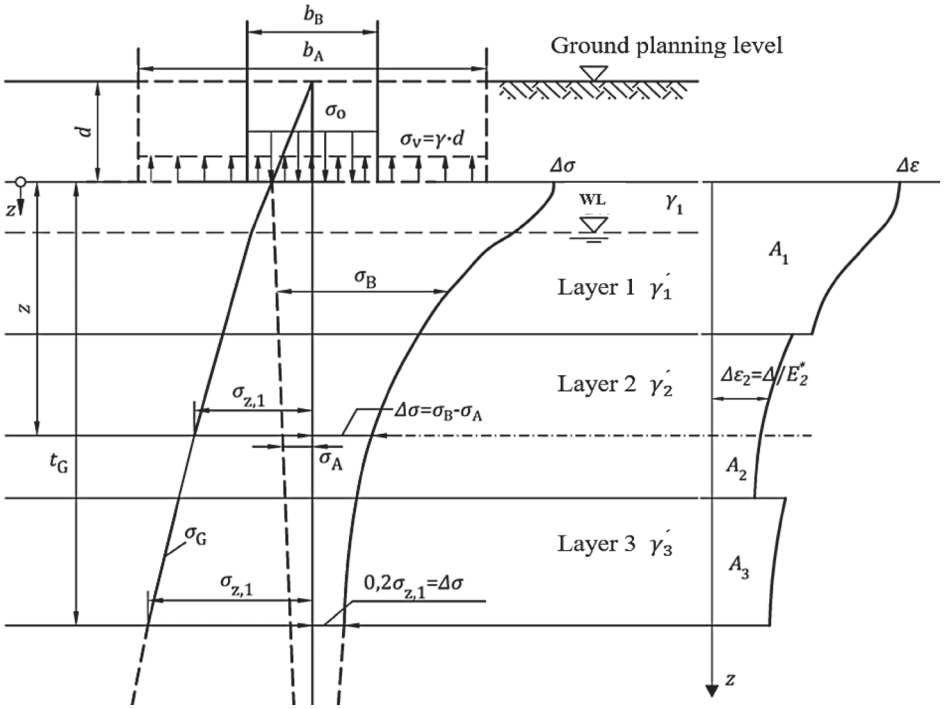

Fig. 1 *Schematic for determining the depth of the compressible thickness of a multi-layer foundation according to the standard ÖNORM B 1997-1-2. In the figure the following designations are: σG – stresses from the self weight of the soil (Pa), σz – normal stresses at depth z from the surface of the soil (Pa), σA – normal stresses from the self weight of soil removed from an excavation (Pa), σB – total normal stresses in the soil from the weight of the soil removed from an excavation and the load on foundation footing (Pa), Δσ – change in the value of normal stress due to the excavation (Pa), d – depth of the foundation (m), σV – stress caused by the weight of the soil removed from the excavation (Pa), σ0 – normal stress at the foundation base (Pa), tG – compressible thickness of the soil, z – vertical coordinate (m), WL - groundwater level, γ – specific gravity of the 1st layer above the groundwater table (kN/m3), γ1', γ2', γ3' – specific gravity of the 1st, 2nd, and 3rd layers below the groundwater table respectively (kN/m3), Ai – area of the figure; Δε – value of the corresponding settlement values*

Tab. 3 *Limit values for deformations of foundations and foundations of structures in new constructions (selective)*

Structure	Limit deformations of the base		
	$(\Delta S/L)_U$	slope, i_u	medium (max) settlement $s_{max,u}$, cm
1. Industrial and civil single-storey and multi-storey buildings with full frames:			
– reinforced concrete, steel-reinforced concrete;	0.002	-	(10)
– the same, with the construction of reinforced concrete belts or monolithic slabs, as well as monolithic building constructions;	0.003	-	(15)
– steel;	0.004	-	(15)
the same with reinforced concrete belts or monolithic slabs;	0.005	-	(15)
2. Buildings with structures that do not experience forces from uneven settlements	0.006	-	12
3. Multi-storey frame-less buildings with load-bearing walls made of:			
– large panels;	0.0016	0.005	12
– large blocks or masonry without any reinforcement;	0.002	0.005	12
– the same with a reinforcement, including reinforced concrete belts or monolithic slabs, as well as monolithic buildings	0.0024	0.005	18

The total settlement is determined by a layer-by-layer summation of the values of the settlement of the soil layers within the compressible thickness:

$$S = \sum S_i = \sum A_i. \quad (7)$$

When determining the suitability of any structural system for normal operations (the service limit state), the question arises as to the limits of the admissibility of the determined values of the deformations.

Obviously, a limit value must be set for deformations, shears, deflections, etc. Such a limit should be enforced by regulatory documents or obtained from expert assessments resulting from the analysis of numerous monitoring data for various buildings and structures.

In the case of assessing the level of deformations, the operational reliability of a building or system can be considered secure if the following condition is met:

$$S \leq s_u, \quad (8)$$

where

S – the strain value calculated;

s_u – limiting value of the joint deformation of the base and the building (here, it should be understood as *u - ultimate*).

The following approach has been adopted in the regulations of some countries and unions. In accordance with Annex H of EN 1997-1, the acceptable settlement In the European Union for conventional foundations may be no more than $s_u = 50$ mm.

In post-Soviet countries the limit deformations of buildings (structures) are regulated by special tables. They are divided into relative deformations $(\Delta s/L)_u$, medium s_u (maximum $s_{max,u}$) and slope i_u. The regulated values of the limit deformations are given both for new constructions and for the reconstruction of structures with different structural designs. Below are some values for allowable deformations of designed residential buildings from DBN V.2.1-10:2018 (the Ukrainian Building Code) (Table 3).

Objectively, the value of "safe" settlements for a building is, of course, dependent on the structural design of the building, its foundations, and the geotechnical conditions, which vary over time and in space. The question of the acceptable limit of a settlement value is as much a matter of principle as it is a matter of discussion, and it requires an analysis of numerous databases involving the monitoring of buildings and structures of various types over many years to understand the whole range of possible displacements. Each construction site has its own unique ground conditions, loads and impacts, so forces, stresses and displacements of "building – base" systems are also unique.

According to (Skempton and McDonald, 1956), allowable settlements for a free-standing foundation can be taken as 60 mm for non-cohesive soil. Table 4 gives the displacement limits for buildings, according to (Bogusz and Godlewski, 2017). Obviously, the values of limiting deformations must be justified and clearly marked for each type of building (structure). It must also be taken into account that the long-term settlement of a substrate can increase due to various factors (e.g., rising groundwater, suffusion processes, etc.).

As can be seen, there is a big difference between the settlement limits given by European norms and Ukrainian norms (as an example of a post-Soviet country standard). Therefore, let us calculate the probability of exceeding precipitation for a range of values from 20 mm to 70 mm and analyse the values obtained.

Tab. 4 *The limiting values of displacement for buildings*

Types of buildings and their load-bearing elements	$\nu_{SLS,}$ mm	ν_{ULS}, mm
Masonry buildings without roof and floor bands, with wooden or steel-framing floors	5 - 7	15 - 18
Masonry buildings with suspended beam-and-slab or reinforced concrete floors, or buildings constructed with precast concrete elements	7 - 9	20 - 25
Cast-in-place concrete or steel buildings	9 - 11	25 - 35

3 PROPOSED METHODOLOGY

3.1 Initial data

All the components of the equations (3-8), directly or indirectly included, are random variables; however, some quantities can be taken as deterministic. In this paper, the geometric characteristics of the foundations are considered deterministic, i.e., *b, l, d.* All other characteristics of the constraint equation are considered random variables. These options include:

1) specific weight of soil γ;
2) vertical load on the foundation F;
3) stresses under the base of the foundation σ_0;
4) vertical stresses in the soil massif from the load on the foundation σ_z;
5) deformation characteristics of the foundation soil (modulus E_S);
6) deformations S.

The following laws of the distribution of random input parameters are adopted in the work:

1. Distribution $P_\gamma = P_\gamma(\gamma)$ of the random value of the specific weight of the soil, which is assumed to be normal with the mathematical expectation m_γ and standard deviation σ_γ. The values of this parameter are determined by the results of testing soil samples.
2. Distributions $P_F = P_F(F)$ of random variables – a vertical load, which are assumed to be normal with mathematical expectations m_F, respectively, and standard deviations σ_F. The values of these parameters can be determined on the basis of the adopted structural solution of the building, taking into account the design standards.
3. Distributions and of the random variables – vertical load and vertical stresses in the soil massif, which are assumed to be normal with mathematical expectations and , and standard deviations and respectively. The values of these parameters can be determined on the basis of the preliminary calculations.
4. Distribution – the random value of the calculated soil modulus, taken as logarithmically normal with the mathematical expectation and standard deviation . The values of this parameter are determined by analysing the results of soil tests.

The specified distributions for loads and materials are mainly taken from the Probabilistic Model Code, draft Eurocode 7 prEN 1997-1:2022 (E), and from some other sources of scientific literature (G.A. Fenton, 1997; A.J. Bond, 2011; K. Phoon, 1999; Roberts, L.A., Mistra, A., 2007; etc.).

All the calculations are made for the estimated service life T. All the calculations have been carried out using the Mathcad Prime software package, and 10^4 tests have been carried out.

3.2 Calculation procedure

Thus, to determine the probability of exceeding the limiting deformations of the "building – base" system, it is advisable to use the method of statistical tests (Monte Carlo) using the standard methodology for calculating the settlements set out in paragraph 1.

The expression for the limit state function for solving this problem can be written as follows:

$$Y = s_u - S(\gamma, E_S, b, l, d, F, t_G) \geq 0. \quad (7)$$

According to this method, N statistical trials are performed. For each test, calculations are made according to the algorithm.

1. We set out a random probability of the following parameters uniformly distributed in the range from 0 to 1: specific weight of the soil P_γ; vertical load intensity P_F; stresses under the base of the foundation σ_0; vertical stresses in the soil massif from the load on the foundation σ_z; deformation characteristics of the foundation soil (modulus E_S).
2. Quantiles are found from the probability values, i.e., the values of the corresponding parameters according to the known distribution functions: P_γ, P_F, .
3. Random values σ_z are determined by formula (4).
4. The random values of stresses from the self-weight of the soil $\sigma_{z,l}$ are determined by the formula $\sigma_{z,l} = \gamma_n \cdot t_n$, where γ_n is the specific gravity of the i^{th} soil layer, and t_n is the thickness of the i^{th} soil layer.
5. Random values of the stresses in the soil massif from the load on the foundation are determined (σ_z).
6. Random stress values $0.2\sigma_{z,l}$ are determined.
7. The compressible thickness of the soil t_G is determined.
8. The random values of deformations S are determined by formula (3) in each layer and the total value of the deformations.
9. In each case, condition (8) is checked.
10. After performing all N tests, the probability of exceeding the limiting deformations over the estimated service life of the P_T is calculated as the ratio of the number of tests N, in which $Y = s_u - S < 0$, to the number of all the tests.

It should be noted that based on this approach, a methodology for assessing the excess of the uneven settlements of the building base $\Delta s/L$ can also be developed, taking into account the factors that most affect the current geotechnical situation. An analysis of the results of the probabilistic calculations will permit choosing such a technical solution for correcting the state of the "building – base" system, which will provide the necessary level of reliability, as enforced by the regulatory documents.

To illustrate the application of the proposed methodology, we performed calculations to determine the probability of exceeding the limiting deformations of an ordinary five-story masonry building, consequences class of building – CC2 (Table B1 EN 1990 Annex B). Table 5 shows the deterministic values, and Table 6 shows the probabilistic characteristics of the normal distribution functions of the random variables.

Tab. 5 *Deterministic quantities*

NN	Parameter name	Designation	Units	Meaning
1	Foundation width	b	m	1.0
2	Foundation length	l	m	1.0
3	Foundation depth	d	m	1.5

Figure 2 illustrates the probability density function (a) and the distribution function of a random variable (b) of the ground deformation modulus (for a variation coefficient of 15%).

Some clarification is required here about the limits of the variation coefficient of the strain modulus E, the value of which directly affects the vertical deformation value. In the course of this

Tab. 6 *Random variables properties*

NN	Parameter name	Designation	Units	Distribution function	Probabilistic characteristics	
					mathematical expectation, *m*	standard deviation σ
1	Specific gravity of the soil	γ	kN/m^3	Normal	20.0	0.6
2	Vertical load	F	kN	Normal	250.0	30.0
3	Estimated soil modulus	E_s	kPa	Lognormal	9.43	1.41
4	Pressure under the foundation	σ_0	kPa	Normal	250.0	30.0
5	Additional stress reduced by dredging the pit at depth *d*	σ_Z	kPa	Normal	220.0	26.4

Tab.7 *Statistical parameters of the distribution of the joint value of the ultimate deformation of the base (for an E value of 15%)*

Parameters	Meaning (1 year)	Meaning (50 year)
Mean value (mathematical expectation), m	0.035	0.044
Standard deviation	0.004	0.002
Variation coefficient, %	8.8	4.5
Maximum value, m	0.049	0.052
Minimum value, m	0.019	0.045

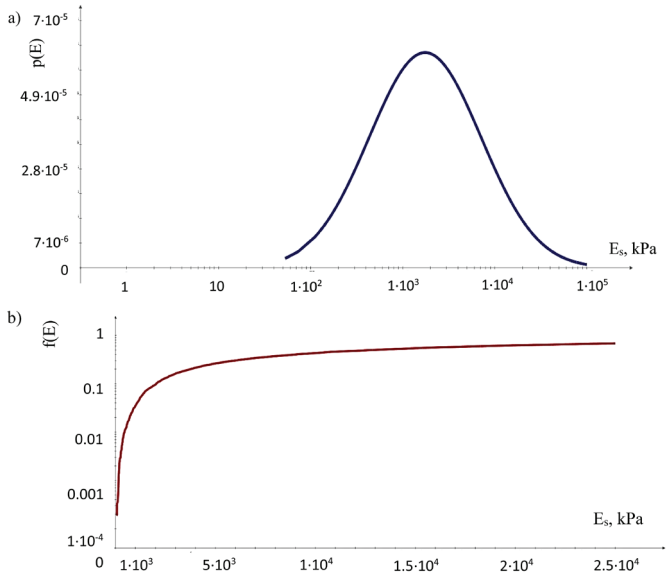

Fig. 2 *Probability density function (a) and the distribution function of a random variable (b) of the ground deformation modulus (for a variation coefficient of 15%), lognormal distribution*

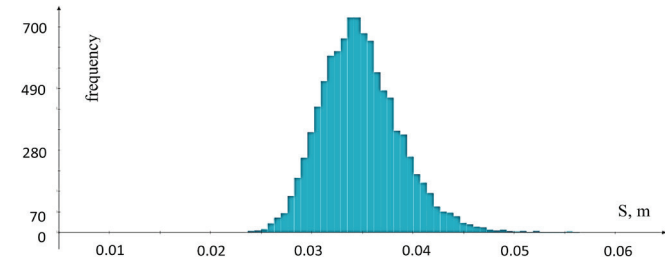

Fig. 3 *Histogram of vertical deformations obtained using the proposed methodology with a variation coefficient of 15 % for E*

Tab. 8 *Results of probabilistic calculations of exceeding ultimate deformation of the base* **s** *(1 year reference period)*

The name of the values	20 mm	35 mm	50 mm	70 mm
The probability of exceeding the limit deformation of the base	1	5 x 10^{-1}	1 x 10^{-4}	0
Recommended minimum values (EN 1990:2002), ISO 2394:2015 (normal level)	3.2x10^{-3}			
Reliability index β	less than 1.28		3.72	5.2
Recommended minimum values (EN 1990:2002), ISO 2394:2015 (normal level)	2.9			

Tab. 9 *Results of probabilistic calculations of exceeding ultimate deformation of the base* $\mathbf{s}_t$ *(50-year reference period)*

The name of the values	20 mm	35 mm	50 mm	70 mm
The probability of exceeding the limit deformation of the base	1	1	1.2 x 10^{-2}	0
Recommended minimum values (EN 1990:2002), ISO 2394:2015 (normal level)	8.1x10^{-2}			
Reliability index β	less than 1.28		2.15	5.2
Recommended minimum values (EN 1990:2002), ISO 2394:2015 (normal level)	1.5			

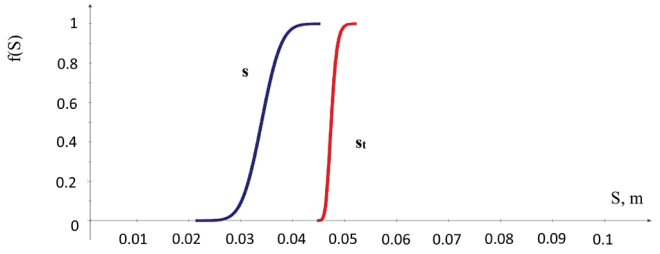

Fig. 4 *Cumulative distribution function of random variables* **s** *and* $\mathbf{s}_t$ *– calculated ground settlements: blue curve: probability of exceeding standard settlements for a year, red curve: probability of exceeding settlements for 50 years*

study, a numerical experiment was carried out and the values of failure the probability – the probability of exceeding permissible settlements for the range of the coefficient of variation E within 5 - 35% (as allowed in scientific and normative literature: Ermolaev, N.N. Mikheev, V.V., 1976; Bugrov, A.K., 2003; Phoon K.K., 2008 etc.), where investigated. The results of the numerical experiment are shown in Figure 3. It can be seen that as the coefficient of variation increases and the limit value of strain s_u decreases, the value of the probability of failure, i.e., the probability of exceeding the limit settlements, also increases.

Using the methodology developed, calculations were carried out to determine the probability of exceeding the ultimate expected deformation of the base. The calculated results are shown in Fig. 3 - 5 and in Tables 7 - 9 (for an E value of 15%).

4 CALCULATIONS ACCORDING TO THE FORM METHODOLOGY

As mentioned earlier, according to this method, the reliability of a building (structure) is achieved by checking the value of the reliability index (safety characteristic) β according to formula (2) in the ULS and SLS limit states. Figure 5 shows the reliability index curves for various permissible settlement values (in brackets) plotted after the FORM reliability has been determined for various values of the variation coefficient of the strain modulus E_s, which varies from 0 to 35%.

It was also interesting to compare the probability of exceeding the sludge limit value calculated by the method proposed by the authors with the results obtained by the FORM method. When comparing the results, it can be seen that the nature of the curves is certainly the same, but the differences are due to the peculiarities of the calculation of the two methods.

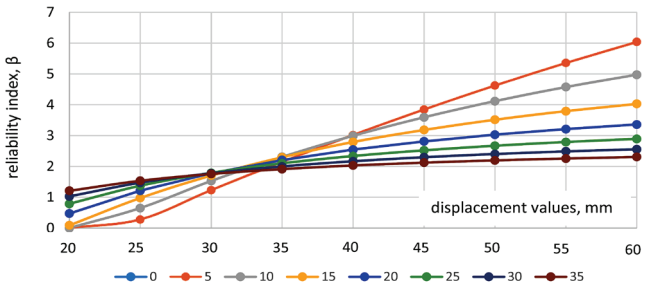

Fig. 5 *Reliability index graphs β for different permissible settlement values and for different values of the variation coefficient of strain modulus E_s*

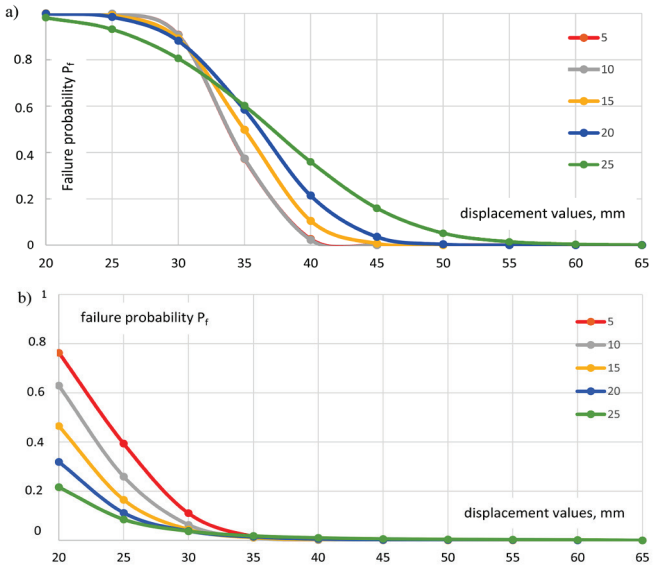

Fig. 6 *Probability of failure according to the criterion of excessive settlement obtained by: a) calculations according to the proposed method (using the Monte Carlo method); b) calculations according to the FORM method*

5 CONCLUSIONS

1. A methodology has been developed to determine the probability of exceeding the vertical deformation limits of the "building – base" system. In developing the methodology, we used a statistical Monte Carlo approach, the use of which allowed us to take into account the stochastic nature of the physical and mechanical properties of the soil mass. Also, this approach shows the possibility of taking into account and integrating the different functions of distributions, using numerical methods of probabilistic-statistical modelling.
2. Using a simple and clear approach dictated by the EU building codes (standards), the proposed method also implements the principles of controlled reliability and durability. The level of the reliability of the "building – base" system at any stage can be checked by a designer (in the process of designing a new structure) or an expert (during the examination of the current facility) and can be changed as required by the customer or a technical inspection.
3. The most important role in probabilistic statistical calculations is played by the initial parameters. As this study has shown, this is especially true for the physical and mechanical characteristics of the soil, the variation coefficients of which are quite large. There is no doubt that this factor cannot be ignored because it has a direct influence on the settlement value and consequently on the establishment of the reliability of the "building – base" system. A numerical experiment was carried out to establish the dependence probability of the failure of the "building – base" system on the coefficient of variation (COV) of the soil deformation modulus in the context of the expected level of settlement. It has been shown that with increasing the COV (over 25%) and decreasing the subsidence level threshold, the probability of failure sharply approaches 1 (Fig. 6a). Taking into account the notion that the probability of failure for a 1-year period should not exceed $P_f = 3.2 \cdot 10^{-3}$ ($\beta_{min} = 2.9$), and $P_f = 8.1 \text{x} 10^{-2}$ ($\beta_{min} = 1.5$) for a 50-year period, the reliability values should be within $P = 0.919...0.9968$. Ideally the COV E_s should not exceed 15-20% to obtain the correct settling values. If $s_u = 50$ mm and a COV E_s range of 15-20% is assumed, the probability of failure values will be in the range $P_f = 1 \cdot 10^{-4}$ ... $4 \cdot 10^{-3}$, and the reliability of the systems will be in the range P = 0,996 ... 0,9999, which complies with the requirements of the standards and also corresponds with the results of research by other scientists involved in the topic (for instance, Ermolaev, N.N. Mikheev, V.V., 1976; Probabilistic Model Code, 2001).
4. Using the Monte Carlo approach, the calculation of the proposed methodology, is suitable for those cases where packages of input data with different distribution laws

(e.g. normal and lognormal, normal and Weibull, etc.) are stacked in a "black box". The FORM method approximates the different distributions by a Gaussian function, which, as sussested in our example, causes some underestimation of the probability of failure and has variations with a rather abrupt character, which often do not correspond to the real situation.

5. Using the proposed method, the probability of failure of the "building – base" system can be determined using the criterion of uneven building foundation settlement $\Delta s/L$ (the difference between two values of the settlement of neighbouring foundations).

REFERENCES

Ahmed, A. – Soubra, A.-H. (2014). *Probabilistic analysis at the serviceability limit state of two neighbouring strip footing resting on a spatially random soil.* Structural safety, Vol. 49, pp.2-9. DOI: 10.1016/j.strusafe.2013.08.001

Beacher, G.B. – Cristian, J.T. (2003) *Reliability and statistics in geotechnical Engineering.* New York, John Wiley. 619 pp. ISBN 0-471-49833-5

Bogusz, W. (2019) *Risk management for tunnelling-induced deformations in relation to the Eurocodes.* Tunnels and Underground Cities: Engineering and Innovation Meet Archaeology, Architecture and Art, pp. 5390-5398. ISBN 978-1-138-38865-9

Bogusz, W. – Godlewski, T. (2017). *Geotechnical interaction in underground space – theory and practice.* Proc. Of the 13th Intern. Conf. on Undergr. Infr. of Urban Areas, pp. 19-31, Wrocław: CRC Press.

Bond, A.J. (2011). *A procedure for determining the characteristic value of a geotechnical parameter*. Proc. of the 3rd Intern. Symposium on Geotechnical Safety and Risk (ISGSR2011). Munich, Germany. pp. 419-426.

Bugrov, A.K. – Shilin, V.G. (2003). *Determination of probabilistic characteristics of active soil pressure by Monte-Carlo method.* Reconstruction of Cities and Geotechnical Construction, No. 5. pp. 92-94. http://www.georeconstruction.net/journals/05/12/12.htm

Calgaro, J.-A. – Gulvanessian, H. (2001). *Management of reliability and risk in the Eurocode System*. IABSE International Conference on "Safety, Risk and Reliability – Trends in Engineering", Malta. pp. 1-6.

Calgaro, J.-A. (2011). *Safety philosophy of Eurocodes*. ISGSR 2011. Vogt, Schuppener, Straub & Bräu (eds.). Bundesanstalt für Wasserbau. pp. 29-36. ISBN 978-3-939230-01-4

Chalermyanont, T. – Benson, C.H. (2004). *Reliability-based design for internal stability of mechanically stabilized earth walls.* Journal of Geotechnical and Geoenvironmental Engineering, 128(5), pp. 381-390 DOI: 10.1061/(ASCE)1090-0241(2004)130:2(163)

Cherubini, C. (2007). *Shallow Foundation Reliability Design.* Proc. of the 1st Intern. Symposium on Geotechnical Safety and Risk. China, Shanghai, pp. 71-90.

CEN (2003) EN 1990:2002 Eurocode. Basis of structural design. European Committee for Standartization, Brussels. 87 pp.

CEN (2018) Eurocode: Basis of structural and geotechnical design (fin. draft, 2018-05-09).

CEN (2018) Eurocode 7: Geotechnical design – Part 1: General rules (fin. draft, 2018-05-04).

CEN (2022) prEN 1997-1 Eurocode 7: Geotechnical design - Part 1: General rules. 105 pp.

DBN V.2.1-10:2018. *State building regulation "Bases and foundation of buildings and structures"* (in Ukrainian), Kyiv, 2018, 36 pp.

Ermolaev, N.N. – Mikheev, V.V. Reliability of Structural Bases (1976). Publishing House of Civil Engineering. 151 pp.

Faber, M.N. – Sørensen, J.D. (2003). *Reliability based code calibration: The JCSS approach.* In A. D. Kiureghian, S. Madanat, & J. M. Pestana (Eds.). Proceedings of ICASP9, 9th International Conference on Applications of Statistics and Probability in Civil Engineering, Vol. 2, San Francisco, USA, pp. 927-935. https://vbn.aau.dk/en/publications/reliability-based-code-calibration-the-jcss-approach

Fenton, G.A. (1997) *Probabilistic Methods in Geotechnical Engineering.* Utah. 96 pp.

Fenton, G. A. – Griffits, D. V. (2002) *Probabilistic foundation settlement on spatially random soil.* Journal of Geotechnical and Geoenvironmental Engineering, 128(5), pp. 381-390

Fenton, G. A. – Griffits, D. V. (2003) *Bearing-capacity prediction of spatially random c-soils.* Canadian Geotechnical Journal, 40(1), pp. 54-65

Fenton, G. A. – Griffits, D. V. (2008) *Risk Assessment in Geotechnical Engineering.* John Wiley & Sons, Inc., 455 pp.

Fishman, G.S. (1995) *Monte Carlo: Concepts, Algorithms, Application.* Springer-Verlag, New York. 722 pp. ISBN 0-387-94527-X.

Harr, M.E. (1996) *Reliability-Based Design in Civil Engineering.* Dover Publications, Inc., Mineola, New York. 291 pp. ISBN 10: 0486694291, ISBN 13: 9780486694290

Harvey, E. – Wahls, F. (1981) *Tolerable Settlement of Buildings*. Journal of the Geotechnical Engineering Division. Vol. 107, No. 11. DOI: 10.1061/AJGEB6.0001204

Honjo, Y. (2011) *Challenges in Geotechnical Reliability Based Design Proc.* of the 3rd Intern. Symposium on Geotechnical Safety and Risk (ISGSR2011). Munich, Germany. pp. 11-27. ISBN 978-3-939230-01-4

ISO 2394:2015 General principles on reliability for structures. (2015) Geneva, Switzerland. 111 pp.

Misra, A. – Roberts, L.A. – Levorson, S.M. (2007) *Reliability analysis of drilled shaft behaviour using finite difference method and Monte Carlo simulation.* Geotechnical and Geological Engineering, 25 (1), pp. 65-77. DOI:10.1007/s10706-006-0007-2

Misra, A. – Roberts, L.A. (2009) *Service limit state resistance factors for drilled shafts.* Géotechnique 59, No.1, pp. 53-61 DOI: 10.1680/geot.2008.3605

Pereia, C. – Caldeira, L. (2011) *Shallow Foundation Design through Probabilistic and Deterministic.* Proc. of the 3rd Intern. Symposium on Geotechnical Safety and Risk (ISGSR2011). Munich, Germany. pp. 199-207. ISBN 978-3-939230-01-4

Phoon, K. – Kulhawy, F. (1999) *Characterization of geotechnical variability.* Canadian Geotechnical Journal, Vol. 36, No. 4, pp. 612-624. DOI: 10.1139/t99-038

Phoon, K. (2017) *Role of reliability calculations in geotechnical design*. Georisk: Assessment and Management of Risk for Engineered Systems and Geohazards, Vol. 11, No. 1, pp. 4-21 DOI: 10.1080/17499518.2016.1265653

Roberts, L.A. – Mistra, A. (2007) *Reliability-Based Design of Shallow Foundations Based on Elastic Settlement.* Proc. of the 1st Intern. Symposium on Geotechnical Safety and Risk. China, Shanghai, pp. 471-483.

Probabilistic Model Code (2001) *Part I – Basic of Design.* ISBN 978-3-909386-79-6. 62 pp.

Schuppener, B. (2011) *Reliability Theory and Safety in German Geotechnical Design*. Paper presented at the third international symposium on Geotechnical Safety & Risk, Federal Waterways Engineering and Research Institute, Germany, pp. 527-536.

Shahin, M.A. – Cheung E.M. (2011) *Probabilistic Analysis of Bearing Capacity of Strip Footings.* Proc. of the 3rd Intern. Symposium on Geotechnical Safety and Risk (ISGSR2011). Munich, Germany. pp. 225-230. ISBN 978-3-939230-01-4

Skempton, A.W. – McDonald, D. H. (1956) *The Allowable Settlements of Buildings.* Proceeding of the Institution of Civil Engineers, Vol. 5, No. 6, Part 1, pp. 727-768.

Vu, T. – Loehr, E. – Smith D. (2018) *Probabilistic analysis and resistance factor calibration for deep foundation design using Monte Carlo simulation.* Helion, Elsevier. Vol. 4, No. 8, pp. 1-18. DOI: 10.1016/j.heliyon.2018.e00727

Won J.Y. (2009). *A probabilistic approach to estimate one-dimensional consolidation settlements.* Proc. of the 17th Intern. Conf. on Soil Mechanics and Geotechnical Engineering. – Alexandria, Egypt. pp. 2012-2015. DOI: 10.3233/978-1-60750-031-5-2012

Zhang, L.M. – Ng, M.Y.A (2005) *Probabilistic limiting tolerable displacements for serviceability limit state design of foundations.* Géotechnique 55(2), pp. 151-162. DOI: 10.1680/geot.2005.55.2-151

Zhang, L.M. – Ng, M.Y.A (2007) *Limiting tolerable displacements and angular distortion for building foundations.* Geotechnical Special Publication, No. 170. DOI: 10.1061/40914(233)18

sciendo

Slovak Journal of Civil Engineering

Vol. 31, 2023, No. 3, 43 – 48
DOI: 10.2478/sjce-2023-0019

EXPERIMENTAL STUDY ON CONCRETE BY ADDING POLYESTER FIBRES

Nirmala D. B[1*], Akshay Angadi[1]

Abstract

There are increased innovations in the field of concrete because there are endless opportunities for innovative materials, techniques, applications, and design. Today's construction industry is looking for cost-effective materials to improve the strength of concrete structures. As a result, an attempt has been made in the current research to investigate the impact of adding polyester fibres (Recron 3s) to concrete. Fibres improve concrete's tensile and flexural strength, fatigue properties, durability, shrinkage properties, impact and erosion resistance, and serviceability. Polyester fibres (Recron 3s) are micro fibres; they contribute to enhancing the resistance of concrete to shrinkage and cracking and also help to improve mechanical properties such as the flexural / split tensile and transverse strength of concrete along with improvements in abrasion and impact strength. An experimental study was done using a M30 mix design. Polyester fibres (Recron 3s) were used in the concrete with varying dosage rates of 0.50 kgs / cu.m – 2.00 kgs / cu.m. This study describes the enhancement in the strength of the M30 grade mix concrete by the addition of polyester fibres (Recron 3s) in the proportions of 0.5, 1, 1.5, 2.0kg/cu.m, and M30 concrete with varying dosages of the polyester fibres (Recron 3s) were mixed and cast.

Address

[1] Dept. of Construction Technology and Management, Sri Jayachamarajendra College of Engineering, JSSSTU, Mysuru, India

* ***Corresponding author:*** nirmaladb@sjce.ac.in

Key words

- Polyester fibres,
- Split tensile strength,
- Flexural strength,
- Recron 3s.

1 INTRODUCTION

The Industrial Revolution, industrial growth, and rapid population growth have all contributed to increases in the demand for construction materials in recent decades. Because of its economy, durability, strength, and flexibility in moulding to any desired shape and size, concrete plays an essential role as a construction material primarily for building, and its demand as a basic building material in construction is increasing. In all types of civil engineering projects, concrete is one of the most important building materials. Since concrete's adoption as a building material, numerous studies and research have been conducted to improve its quality, strength, and durability. Simultaneously, efforts are being made to reduce the cost of concrete construction when compared to other materials.

Concrete is a material made up of cement, water and fine and coarse aggregates; it has a high compressive strength but a low tensile strength. There are two methods for dealing with low tensile strength, i.e., reinforcing and pre-stressing. Because of its many valuable properties, such as high compressive strength, stiffness, low thermal and electrical conductivity, and low combustibility and toxicity, concrete is used in a variety of innovative designs. Secondary reinforcement in concrete has recently gained popularity in a variety of fields, providing a solid technical foundation for addressing these flaws. Polyester fibre has been one of the most successful commercial applications. Recron 3s is a new generation secondary reinforcement for the construction industry. Recron 3s polyester fibre improves the homogeneity of concrete by reducing aggregate segregation. It reduces shrinkage cracks/

micro cracks and increases the ductility and the compressive, tensile and flexural strength by reducing water permeability. The addition of small, closely spaced, uniformly dispersed fibres to concrete has long been recognised as a way to improve its static and dynamic properties while also providing crack resistance.

Fibre-reinforced concrete (FRC) is defined as "concrete that contains fibrous material to improve structural integrity." It is made up of short discrete fibres that are uniformly distributed and randomly oriented. Furthermore, the character of fibre-reinforced concrete varies, depending on the concrete, fibre materials, geometries, distribution, orientation, and densities used. Steel, glass, synthetic and natural fibres are among the various types of fibres used in concrete, each of which lends varying properties to the concrete.

This study describes enhancement in the strength of a M30 grade mix concrete by the addition of polyester fibres (Recron 3s) in the proportions of 0.5, 1, 1.5, 2.0kg/cu.m and M30 concrete with varying dosages of polyester fibres (Recron 3s), which were mixed and cast. The total mix proportion for this investigation involves five mix proportion samples: Mix proportion one is a normal M30 concrete mix without any polyester fibre (Recron 3s). The second mix proportion is an M30 concrete mix with a dosage of 0.5kgs/cu.m polyester fibre (Recron 3s). The third mix proportion is an M30 concrete mix with a dosage of 1.0 kgs/cu. polyester fibre (Recron 3s). The fourth mix proportion is an M30 concrete mix with a dosage of 1.5kgs/cu.m polyester fibre (Recron 3s). The last mix proportion is an M30 concrete mix with a dosage of 2.0kgs/cu.m polyester fibre (Recron 3s). The aim of the present investigation is to study the workability parameters of an M30 grade of fresh concrete using the slump cone, compaction factor, and Vee-bee time tests. The moulds were cast for 7, 28 and 56 day strength parameters from each mix proportion. The fresh and mechanical properties of the concrete with polyester fibres (Recron 3s) are compared with normal concrete properties.

2 EXPERIMENTAL PROGRAM

2.1 Material Properties

A. Cement – The cement used was OPC 53 grade cement. There should be no lumps in the cement. Ordinary Portland cement of grade 53, which complies with IS 12269 (1987), was used, and it had a fresh, uniform consistency. If there is any foreign matter or lumps, it should not be used. The cement should be kept as dry as possible.

Tab. 1 *Physical properties of cement*

Sl no	Physical properties	Results
1	Specific gravity	3.13
2	Standard consistency	29.5%
3	Initial setting time	60 min
4	Final setting time	270 min

B. Fine aggregate - M-sand conforming to zone II and passing through a 4.75mm IS sieve was used as a fine aggregate. The physical properties of the fine aggregates were tested as per IS: 383-2016.

Tab. 2 *Physical properties of fine aggregate*

Sl no	Properties	Results
1	Specific gravity	2.67
2	Water absorption	2.14%
3	Fineness modulus	3.47
4	Sieve zone	Zone II

C. Coarse aggregate - The size of the coarse aggregates was 20 mm passing and 4.75 mm IS sieve - retained coarse aggregates. IS: 383-2016 code is referred to for the coarse aggregate.

Tab. 3 *Physical properties of coarse aggregates*

Sl no	Properties	Result
1	Specific gravity	2.79
2	Water absorption	0.4%
3	Fineness modulus	6.9
4	Aggregate impact value	26.2%
5	Aggregate crushing value	26.8%

D. Polyester fibre (Recron 3s) – Triangular virgin polyester fibre, which is manufactured by Reliance Industries Limited, is called Recron 3S polyester fibre. For use in concrete, Recron 3S fibres are manufactured in an ISO 9001:2000 facility. ASTM C 1116 was met by the fibres.

Tab. 4 *Properties of polyester fibre (Recron 3S)*

Sl no	Properties	Specification
1	Shape	Triangular
2	Cut length	12mm
3	Effective diameter	20-40 microns
4	Specific gravity	1.34-1.39
5	Elongation	60-90%
6	Melting point	250-265 deg.C
7	Tensile strength	4-6 Gpd
8	Young's modulus	>5000 Mpa

E. Water - The water used for the mixing was clean and free of any organic matter or harmful solutions that could cause the mortar to deteriorate and lose its properties. It is not a good idea to use salt water. The water used for both mixing and curing the specimens should be the same.

F. SP-430 dis – Conplast SP 430 dis super plasticizer was used as the chemical admixture.

2.2 Mix Design and Mix Calculations

The process of choosing the right concrete materials and figuring out their ideal proportions in order to manufacture concrete that meets certain compressive strength requirements and has a desirable degree of workability as economically as possible is known as concrete mix design. As per IS: 10262-2009, the

mix design of the concrete was performed. M30 grade concrete was adopted for the mix proportion. The water / cement ratio adopted was 0.45. The mix proportion of the M30 grade concrete 1:2.1:3.7 was calculated as per IS: 10262-2009. Conplast SP-430 dis plasticizer was used as the chemical admixture. The total mix proportion for this investigation involved five mix proportion samples: Mix proportion one was a normal M30 concrete mix without any polyester fibre (Recron 3s). The second mix proportion was an M30 concrete mix with a dosage of 0.5kgs/cu.m polyester fibre (Recron 3s). The third mix proportion was an M30 concrete mix with a dosage of 1.0 kgs/cu. polyester fibre (Recron 3s). The fourth mix proportion was an M30 concrete mix with a dosage of 1.5 kgs/cu.m polyester fibre (Recron 3s). The last mix proportion was an M30 concrete mix with a dosage of 2.0kgs/cu.m polyester fibre (Recron 3s). For each mix, nine cubes (150 x 150 x 150 mm size), nine cylinders, (150 x 300 mm size), and nine prisms (100 x 100 x 500mm size) were cast to determine the compressive, split tensile and flexural strength of the concrete for each mix.

Tab. 5 *Mix design*

Particulars	Quantity
W/C ratio	0.45
Cement	340kg/m^3
Fine aggregate	728kg/m^3
Coarse aggregate	1272kg/m^3
Water	154ltr
Chemical Admixture	SP430 dis

Tab. 6 *Different mix designs*

Designation	Description
M-0	Conventional concrete mix
M-0.5	Concrete mix containing 0.5kg/m3 of polyester fibres
M-1.0	Concrete mix containing 0.5kg/m3 of polyester fibres
M-1.5	Concrete mix containing 0.5kg/m3 of polyester fibres
M-2.0	Concrete mix containing 0.5kg/m3 of polyester fibres

3 RESULTS AND DISCUSSION

3.1 Slump test

The designed slump value for conventional concrete is 75 mm as per IS 10262:2009. The slump value obtained for conventional concrete is 73 mm; it was acceptable as per the design. The degree of workability of conventional concrete is medium as per IS 456:2000. As polyester fibres were added to the conventional concrete mix in 0.5, 1.0, 1.5 and 2.0 kg/m^3 proportions, the slump values were 68, 59, 51 and 44 mm simultaneously. With the increase in the percentage of polyester fibres, the slump value decreased as shown in Table 7. The concrete mix with 2.0kg/m^3 polyester fibres as the lowest slump value and the degree of workability of the mix was also low as per the code.

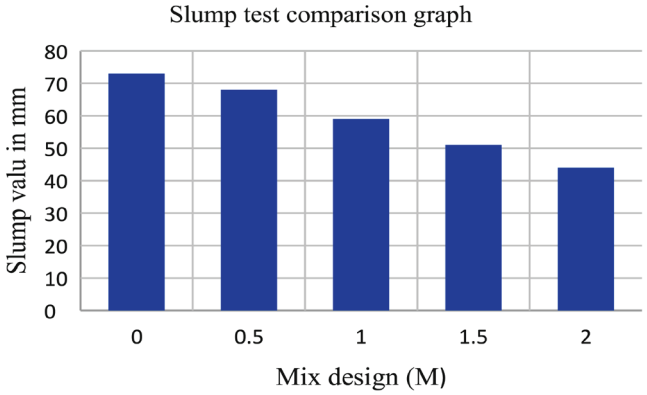

Fig. 1 *Comparison of the slump with the different concrete mixes*

Tab. 7 *Slump test results*

Concrete mix	Slump (mm)	Degree of workability as per IS 456:2000
M-0	73	Medium
M-0.5	68	Medium
M-1.0	59	Medium
M-1.5	51	Medium
M-2.0	44	Low

3.2 Compaction factor test

The compaction factor value for conventional concrete mix is 0.88, and the degree of workability is medium. The compaction factor value decreases as the fibres added to the concrete mix increase. A comparison of the compaction factor values are shown in the graph below.

Tab. 8 *Compaction factor test results*

Concrete mix	Compaction factor value	Degree of workability
M-0	0.88	Medium
M-1	0.87	Medium
M-2	0.85	Medium
M-3	0.83	Medium
M-4	0.82	Low

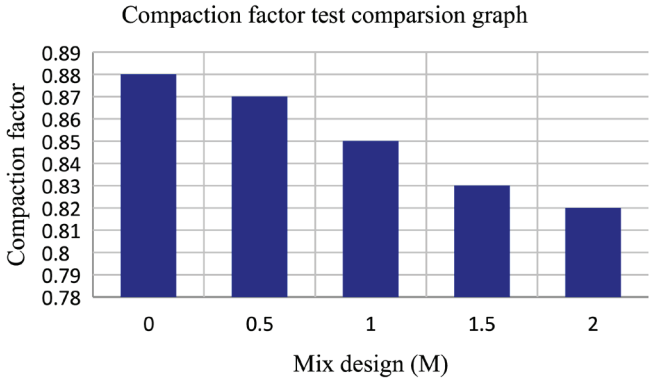

Fig. 2 *Comparison of the compaction factor with the different concrete mixes*

3.3 Compressive strength test of the concrete

The M30 mix design was adopted. The compressive strength of conventional concrete at 28 days of curing is 34.96 N/mm^2. Concrete containing 0.5, 1.0, 1.5 and 2.0 kg/m^3 of polyester fibres possesses 36.54, 40.06, 35.03 and 35.67 N/mm^2 of compressive strength at 28 days respectively. A concrete mix containing 1kg/m^3 of polyester fibres has more compressive strength than other mixes. It has 14.58% more compressive strength than a conventional mix at 28 days' strength. Beyond that, the compressive strength is reduced as the amount of polyester fibre increases. The M-2.0 concrete mix has a lower compressive strength than the conventional mix at 28 days. It decreased 13.13% from the conventional concrete.

Tab. 9 *Compressive strength test results*

Concrete Mix	Compressive strength of concrete (N/mm2)		
	7 days	28 days	56 days
M-0	24.07	34.96	35.31
M-0.5	24.44	36.54	37.02
M-1.0	27.70	40.06	40.67
M-1.5	24.74	35.48	36.14
M-2.0	23.11	30.37	31.33

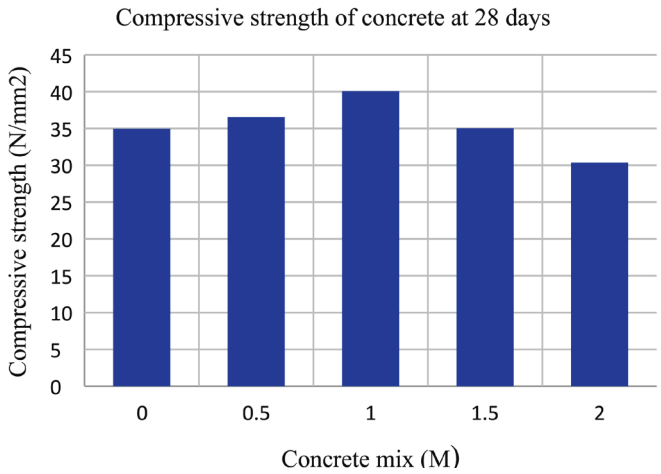

Fig. 3 *Comparison of compressive strength with different concrete mixes*

3.4 Split tensile strength test of concrete

The split tensile strength of conventional (M-0 mix) concrete at 28 days is 3.13 N/mm^2. The M-0.5, M-1.0, M-1.5 and M-2.0 concrete mixes possess 3.27, 3.60, 3.30 and 3.23 N/mm^2 of split tensile strength at 28 days respectively. The M-1.0 concrete mix has 15.02% more split tensile strength compared to the conventional mix. The M-1.5 and M-2.0 concrete mixes show that as the fibre content increases, the tensile strength decreases, but the tensile strength does not decrease below the conventional mix strength.

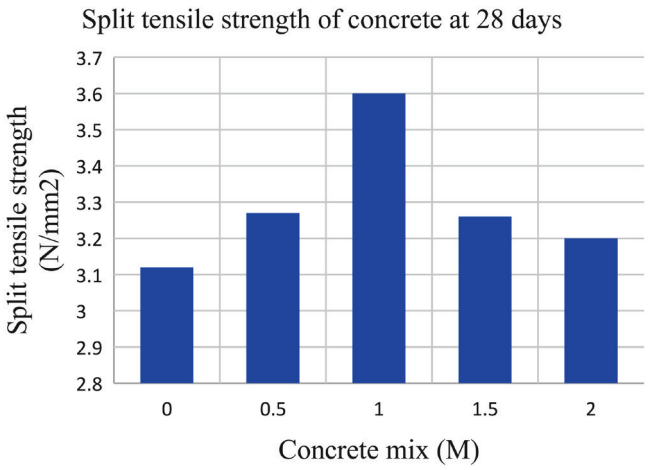

Fig. 4 *Comparison of split tensile strength with different concrete mixes*

Tab. 10 *Split tensile strength test results*

Concrete Mix	Split tensile strength of concrete (N/mm^2)		
No. of days	7 days	28 days	56 days
M-0	2.69	3.13	3.27
M-0.5	2.98	3.27	3.47
M-1.0	3.13	3.60	3.72
M-1.5	2.92	3.30	3.41
M-2.0	2.91	3.23	3.33

3.5 Flexural strength test of concrete

The flexural strength of the five concrete mixes at 28 days was 4.91, 5.15, 6.08, 5.35 and 4.60 N/mm^2 respectively. The M-1.0 concrete mix had 23.9% more strength than the conventional concrete. The flexural strength increased as the fiber content increased up to the M-1.0 mix; beyond the M-1.0 concrete mix, as the fibre content increased, the flexural strength reduced. The M-2.0 concrete mix had 6.3% less flexural strength than the conventional mix at 28 days.

Tab. 11 *Flexural strength test results*

Concrete Mix	Flexural strength of concrete (N/mm^2)		
No. of days	7 days	28 days	56 days
M-0	3.57	4.91	5.33
M-0.5	3.94	5.15	6.19
M-1.0	4.70	6.08	6.74
M-1.5	3.84	5.35	5.65
M-2.0	3.40	4.60	5.30

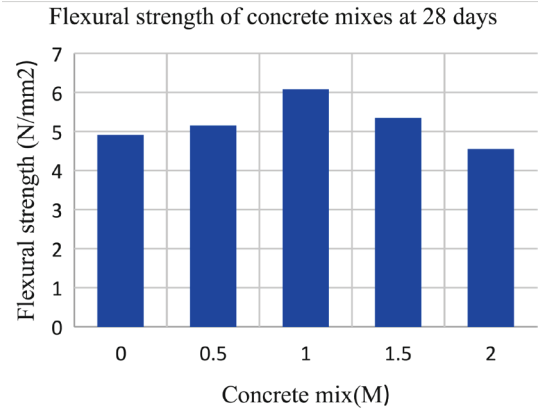

Fig. 5 *Comparison of flexural strength with different concrete mixes*

4 CONCLUSION

After analysing the results, it was possible to draw some insightful conclusions about the strength properties of the fibre added to the concrete for the M30 concrete mix. The investigation of the strength characteristics of the properties of the fibre added to the concrete leads to the following conclusions:

As the polyester fibre content increased in the concrete mix, the slump value decreased. The workability of concrete is measured from the slump value. Hence, it can be concluded that with the increase in fibre content in the concrete mix, the workability of the concrete decreases.

The workability of concrete is also measured from the compaction factor test: as the compaction factor value declines, the workability of the concrete reduces. Here, the compaction factor values decline as the polyester fibre content increases in the concrete mix; therefore, the workability of the concrete declines as the polyester fibre content increases in the concrete mix.

As can be seen from the experimental results, the optimum polyester fibre content of 1.0 kg/m^3 is recommended for achieving the maximum benefits. A 1.0 kg/m^3 concrete mix containing polyester fibre possesses more compressive, split tensile and flexural strength compared to the other fibre - containing concrete mixes and the conventional mix. The 1.0 kg/m^3 polyester fibre - added concrete mix has a lower slump value and compaction factor value than the conventional mix; however, this lies within the range of the design, so the addition of 1.0 kg/m^3 polyester fibre to the concrete mix is an optimum value compared to the other mixes.

The compressive strength of the M30 at 28 days increased with the addition of the polyester fibre compared to the conventional concrete. The 0.5, 1.0 and 1.5kg/m^3 fibre - containing concrete mixes have 4.52%, 14.58% and 1.5% increased compressive strength compared to the conventional concrete, but the 2.0kg/m^3 fibre-containing concrete mix has 13.13% less compressive strength compared to the conventional concrete. The 1.0kg/m^3 polyester fibre - containing concrete has the highest compressive strength; beyond that, as the fibre content increases, the compressive strength is reduced.

The split tensile strength of the concrete containing 1.0kg/m^3 of polyester fibre shows 15.02% more strength than the conventional concrete. Beyond that, the additional fibre reduces the split tensile strength, but not below that of the conventional tensile strength. The 1.0kg/m^3 polyester fibre - containing concrete has optimum strength values compared to the other concrete mixes.

Our study of a conventional concrete mix with polyester fibre added to the mix has revealed the superiority of the 1.0kg/ m^3 of polyester fibre - added concrete by showing an increase of 23.9% flexural strength at 28 days. As the addition of fibre increases beyond 1.0kg/m^3, the flexural strength is reduced. The 1.0kg/m^3 polyester fibre- containing concrete has the maximum flexural strength compared to the other mixes, and it is recommended as the optimum value to be added to concrete for maximum benefits.

REFERENCES

Akanksha, P. - Pradeep, T. V. (2020) *Effect of addition of recron 3s fiber and glass fiber on the strength characteristics of M-30 concrete.* JETIR, Vol.7, No. 2.

Selvarani, B. - Preethi, V. (2021) *Investigational study on optimum content of GGBS and fibres in fibre non-breakable self compacting concrete.* Materials Today: Proceedings.

Venkat, B. - Narsimha, R.- Mahesh, M. - Satya, S. (2016) *Recron fibre reinforced concrete pavements,* IJEDR, Vol.4, No. 4.

Dara, - Easwar, karthik, - Shaik, M.- Arifullah. (2020) *Micro structural examination of low-density light weight concrete based on expanded polypropylene foam.* Materials Today: Proceedings.

D.S.V. Prasad, D.S.V.- Shivanarayana, - Vinod, K.G. (2017) *Strength and durability studies of recron 3s fiber reinforced concrete,* International journal of advanced research trends in engineering and technology, Vol.4, No. 9.

Shaik, - Yajdani, - Korrapati, - Anil, K. - Ganta, S. R. (2017) *Study on properties of concrete using recron 3s fiber,* International Journal of Science Technology & Engineering, Vol.4, No. 3.

Sunil, V. - Desale, - Bhagyashri, S. (2015) *Use of industrial waste and recron 3s fiber to improve the mechanical properties of concrete,* Indian Journal of Research, Vol.4, No. 7.

IS 10262 : 2009. *Concrete mix proportioning. Bureau of Indian Standards.* New Delhi, India.

IS 456 : 2000. *Plain and reinforced concrete. Bureau of Indian Standards.* New Delhi, India.

IS : 516 – 1959. *Methods of tests for strength of concrete.* Bureau of Indian Standards, New Delhi, India.

IS 12269: 2013. *Ordinary portland cement, 53 grade –specification.* Bureau of Indian Standards. New Delhi. India.

IS : 4031- 1988. *Methods of physical tests for hydraulic cement.* Bureau of Indian Standards. New Delhi. India.

IS : 2386 – 1963. *Methods of test for aggregates for concrete.* Bureau of Indian Standards. New Delhi. India.

IS: 383 – 1970, *Specification for coarse and fine aggregates from natural sources for concrete.* Bureau of Indian Standards. New Delhi. India.

Julia, - Blazya,- Rafal, B. (2021) *Polypropylene fiber reinforced concrete and its application in creating architectural forms of public spaces,* Case Studies in Construction Materials.

Neeladharan, C. - Murulidharan, A. (2020) *Behaviour of fibre reinforced concrete using recron 3s,* International Journal of Advanced Research in Management, Architecture, Technology and Engineering, Vol.6, No. 6.

Radhikesh, P. - Nanda, - Arup, K. Mohapatra,- Bipleb, B. (2020) *Influence of metakaolin and recron 3s fiber on mechanical properties of fly ash replaced concrete,* Construction and Building Materials, pp. 270-280.

Rafat, S, - Kushal, K. (2011) *Effect of polyester fibres on the compressive strength and abrasion resistance of HVFA concrete,* Construction and Building Materials,Vol.29, pp. 270-278.

Ridha, N. - Prashant, K. (2016) *Effect of different percentages of polypropylene fibre (recron 3s) on the compressive, tensile and flexural strength of concrete,* International Journal of Engineering Research & Technology, Vol. 5, No. 11.

Saif, H. - Imtia, M. Uddin, Munshi. (2021) *Assessing the influence of fly ash and polypropylene fiber on fresh, mechanical and durability properties of concrete,* Engineering Science.

Sujay, H.M. - Nishant, A. N.- Sairam, V. (2020) *Experimental study on durability characteristics of composite fiber reinforced high-performance concrete incorporating nanosilica and ultra fine fly ash,* Construction and Building Materials.

sciendo

Slovak Journal of Civil Engineering

Vol. 31, 2023, No. 3, 49 – 54
DOI: 10.2478/sjce-2023-0020

PREPARATION AND MODIFICATION OF CHIP-CEMENT WOODEN COMPOSITES BASED ON RECYCLED PLASTICS

Terézia CABANOVÁ[1*]

Abstract

The production of plastics and the associated increasing amount of plastic waste is currently a serious environmental problem that has a negative impact on the environment. It is necessary to develop new methods of recycling and also solutions for the further use of already recycled plastics. Thus far, a lot of research has been devoted to this issue, which focuses on the effective recycling and reuse of recycled plastic in the construction sector. One of the possibilities is the application of a filler substitute in concrete, which is an economically and ecologically advantageous solution that ensures optimal thermal insulation and acoustic properties. The aim of this study was to analyze the potential replacement of conventional aggregates in lightweight concrete, with a filler made of recycled plastic with a lower bulk density. In the research, wood chips were used in combination with recycled waste fillers including polystyrene (SE), polyethene (SP), and polyurethane foam (SU) in ratios of 1:3, 1:1, and 3:1 as an alternative to conventional filler. Concrete composites from these materials were prepared and characterized by their bulk density, thermal conductivity and compressive strength parameters.

Address

[1] Dept. of Materials Engineering and Physics, Slovak University of Technology, Slovakia

[*] ***Corresponding author:*** terezia.cabanova@stuba.sk

Key words

- Recycled plastic filler,
- Compressive strength,
- Thermal conductivity,
- Bulk density,
- Cement composites.

1 INTRODUCTION

The production of vast amounts of waste worldwide is a growing problem for the environment, and issues involving its disposal and storage need to be effectively addressed. One of the significant problems related to waste generation is the excessive production of plastic, which causes an enormous amount of waste (about 6,5 billion tonnes worldwide). Its primary raw material is fossil fuels (approximately 10% of fossil fuels), which causes pollution associated with oil extraction. Plastic waste is currently recycled, burned in various incinerators, and disposed of in landfills. Recycling is a complex process that has certain limits and is not sustainable, so the disposal and incineration of waste is still the preferred process. Available statistical data show that around 51% of plastic waste is buried; 27% is incinerated; and 22% is recycled (N. Saikia & J. De Brito, 2012). The ill-conceived disposal and storage of plastic waste now require more innovative and efficient solutions that consider the consequences of excessive environmental pollution due to the long-term degradation of plastics. The greatest threats we are experiencing today are damaged ecosystems, polluted seas and oceans, and endangered coral reefs, along with the pollution of the atmosphere, groundwater, and the overall environment.

In construction, concrete is one of the most used materials, mainly due to its simplicity, strength, durability, and adaptability. As one of the main components of concrete, cement production produces a large number of greenhouse gases, which also contribute a large part to climate change. The search for environmentally friendly alternative solutions that can replace natural resources with other recycled materials has been the subject of much research (C. Jacob-Vaillancourt & L. Sorelli, 2018; M. Batayneh et al., 2007). The application of recycled plastics is valuable, for example, in lightweight building materials, where they can replace the aggregates in concrete.

Concrete containing different types of plastic granules differs from ordinary concrete in that they reduce concrete´s bulk density and improve its thermal insulation properties. This idea has more positives, e.g., protecting natural resources, reducing greenhouse gas production, reducing energy costs, reducing the amount of plastic waste in landfills, and improving the sustainability of natural resources. Some research reports that the use of plastic waste in concrete has an impact on its energy absorption and concrete's impact strength (I. Almeshal et al., 2020; S. Bahij et al., 2020; L. Gu & T. Ozbakkaloglu, 2016; N.Saikia & J. de Brito, 2012). The main challenge is to improve the physico-mechanical properties of such kinds of concrete, where resistance and compressive strength are still a major problem. Fire resistance, durability, and time-dependent properties are also monitored. Currently, various types of recycled materials are used for thermal insulation and acoustic purposes, including, for example, recycled glass foam, cotton, textile fibers, etc. As for plastic waste, polyester fibers made from recycled PET bottles are an adequate component for the thermal insulation of buildings. (Francesco Asdrubali et al., 2015; N.Saika & J. De Brito, 2012).

This research is mainly aimed at finding the most straightforward possible alternatives to lightweight concrete using recycled plastics and wood chips as fillers. The mixtures studied contained recycled waste polystyrene, polyethylene and polyurethane foam; they were mixed with wood chips in individual proportions (Table 1). Test samples of lightweight concrete were made from the above-mentioned materials; after 28 days, their bulk density, coefficient of thermal conductivity, and dependence on compressive strength were analyzed. The primary purpose of combining wood chips and recycled plastic waste in a cement composite was to find the variant with the lowest bulk density with respect to mechanical and thermal-technical properties. The principle of the experiment consisted in the use of plastic waste as a filler for lightweight concrete in order to achieve an ecologically and economically available material.

2 METHODOLOGY

The measurements took place in a laboratory environment, where standardized procedures for sample production and corresponding measurements were maintained (EN 206:2013+A2:2021). The percentage and volume values of the individual proportions of the materials used were determined in advance. Three types of recycled pastes were used as filler in combination with wood chips. The samples were made specifically from recycled polyethylene, recycled polyurethane waste, and recycled expanded polystyrene (Fig. 1).

2.1 Materials

Wood chips are an easily available and processable material that contributes to the woodworking industry. Materials of a plant origin are able to regulate the surrounding climate and have a good synergy with the external environment. The positive properties of wood chips include their low bulk density (ranging from 100 to 300 kg/m^3 depending on the moisture content and type of wood), good thermal insulation properties (the thermal conductivity of wood chips is 0.038 W.m^{-1}. K^{-1}), a good ratio of compressive strength to tensile strength after bending, and a good sound absorption coefficient. The negative properties of wood chips are large volume changes due to humidity, low compressive strength, large shrinkage, and creep (Zdeněk Pastorek et al., 2004). Polyethylene is a thermoplastic polymer, the production of which varies, depending on the required physical and mechanical properties of the final product. It is characterized by thermal stability, high strength and low density. Depending on the type of polyethylene, its density varies, mostly in the range of 900 - 980 kg.m^{-3} (Alejandro Meza de Luna and Faiz Uddin Ahmed Shaikh, 2020). Expanded polystyrene belongs to the group of foam plastics with a closed surface, and its density ranges

Fig. 1 *a) Recycled polyethene fraction 4/8 mm, b) Recyclate from waste polyurethane fraction 4/8 mm, c) Recycled from expanded polystyrene fraction 4/8 mm, d) Wood chip fraction 4/16*

from 11 - 32 kg.m^{-3}. It is produced by polymerization of the chemical substance styrene and is obtained industrially from petroleum (Wensu Chen et al., 2015). A universally usable material is polyurethane foam, which has a low coefficient of thermal conductivity and represents good thermal insulation properties. It does not burden a building during insulation due to its low density (soft foams from 15 to 70 kg.m^{-3}, hard foams from 10 up to 600 kg.m^{-3}) and bulk density; it also has good mechanical strength. It is characterized by excellent sound insulation and fire resistance and keeps its properties constant and unchanging. The recycling of this material takes place by crushing it into smaller parts and subsequently processing it (Gama V. Nuno et al., 2018). The experiment was supplemented with 100% of the mixing value from previous research with the same amount of cement and water to the water and cement ratio (M. Ledererova et al., 2018). The recipe of the individual mixes is shown in Table 1. In the experiment, Portland cement CEM II/B-M (S-LL) 32.5 R with the characteristics declared by the manufacturer was used for the production of the test samples (EN 197-1:2011). Samples of the lightweight concrete with a constant water-to-cement ratio of w/c=0.5 and a constant dose of cement of 175 kg.m^{-3} were produced.

Tab. 1 *Composition of individual mixtures with a water coefficient of 0.5*

A component of concrete		Filler ratio				
		Amount during production in kg/l				
		1:0	3:1	1:1	1:3	0:4
Cement		0,75 kg				
H2O (w/c=0,5)		0,35 l				
Wood chips + Polystyrene (EPS)	SE	4 l	3 l	2 l	1 l	
			1 l	2 l	3 l	4 l
Wood chips + Polyethylene (PE)	SP	4 l	3 l	2 l	1 l	
			1 l	2 l	3 l	4 l
Wood chips + Polyurethane foam (PUR)	SU	4 l	3 l	2 l	1 l	
			1 l	2 l	3 l	4 l

2.2 Preparation of samples

Cube-shaped samples (100 mm x 100 mm x 100 mm) were fabricated under laboratory conditions with the appropriate equipment. Before the actual production, the preparation of the moulds, necessary materials, and tools was carried out. According to the prescribed amount, an exact amount of filler, cement and mixed water was measured; they were first mixed in a dry state, and then water was added. After thorough mixing was conducted, the mixture, which was filled in three layers into moulds, was prepared (Fig.2). Each layer was separately compacted according to the standard (EN 206:2013+A1:2018). This procedure was repeated during the preparation of each mixture. The three filled moulds were subsequently stored in a humid environment for 48 hours. The samples were then demoulded, marked with appropriate marks, and stored in a place with relative humidity ($\varphi \geq 95$ %) for 28 days.

2.3 Properties and methods tested

One of the properties observed was the bulk density given by the ratio of the mass of the material without voids and pores to the total volume of the material. It was evaluated on the test samples of each mixture after 28 days by measuring the necessary parameters and then calculating the bulk density. The decisive factor in the resulting bulk density was the weight of the cement binder and, above all, the weight of the filler, where the ratio of the number of wood chips with a given granulate of recycled plastic changed. Generally, the values of the bulk density decreased as the proportion of recycled plastics and fillers increased. In the case of the expanded polystyrene combination (SE), the volumes and the mass gradually decreased from 420 kg.m^{-3} to the lowest value of 260 kg.m^{-3}. When combining the wood chips with the

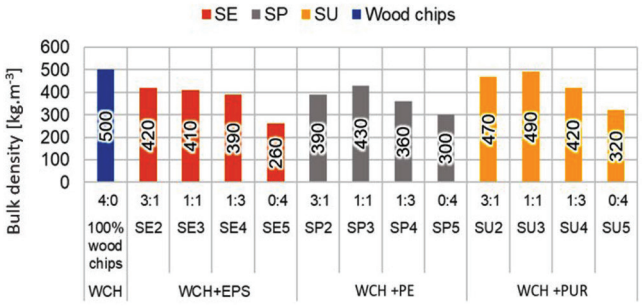

Fig. 3 *Dependence of the bulk density on the type and ratio of filler used.*

Fig. 2 *The mixture of fresh concrete and moulds filled with the manufactured samples*

polyethene (SP) and polyurethane foam (SU), the increase in volume was assessed at different ratios (1:1 versus ratios of 3:1 and 1:3), where their bulk density were recorded. This fact may also be attributed to the processing of the mixture.

Another parameter studied was the basic thermal characteristics, which were evaluated on the test samples at the age of 28 days using the Isomet 2114 instrument with a surface probe with a measuring range of 0.04 - 0.3 $W.m^{-1}.K^{-1}$. The main parameter observed was the thermal conductivity coefficient. The measurement was carried out in a laboratory environment with a temperature of about 20 °C and relative humidity of φ = 60 %. The results showed that as the proportion of plastic recyclate increased, the coefficient of the thermal conductivity values gradually decreased. Regardless of the filler used, the resulting values ranged from 0.066 to 0.129 $W.m^{-1}.K^{-1}$, and their course corresponded with the results of the bulk density calculations (Fig.4).

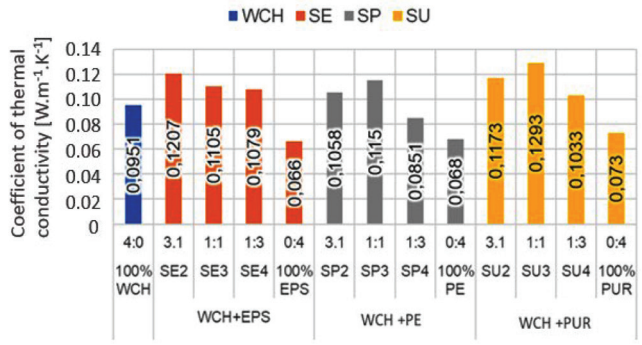

Fig. 4 *Dependence of the coefficient of thermal conductivity on the type and ratio of the fillers used.*

The last aspect observed was the tension at the specified deformation, which determines the ability of the material to withstand pressure loads. The test samples were centrically placed between the printed plates of the hydraulic press and perpendicular to the direction of the concrete compaction (Fig.5). By pushing the plates, a smooth sample load was gradually developed, where at specified deformations of 2.5; 5; 7.5 and 10%, the magnitude of the force load applied was recorded. The resulting value of the voltage magnitude was obtained using a formula based on the recorded values.

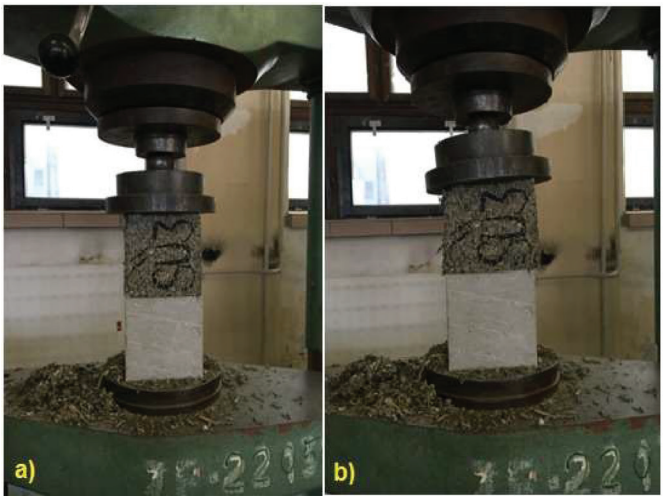

Fig. 5 *Test sample stored in a hydraulic press: a) before loading; b) after loading.*

The amount of the deformation of the individual samples mainly depended on the changing proportions of the amount of filler used and on its properties. The results of the strength characteristics are shown in Fig. 6. The compressive strength or the stress during deformation gradually increased with the increasing content of the plastic filler. The values of the maximum stresses, regardless of the filler used, ranged from 0.18 to 0.67 MPa, while the test samples with a 100% chip dosage reached a maximum stress of 0.76 MPa. The composites with filler based on polyurethane foam took a different course, i.e., the highest values of compressive strength at a specific strain were manifested at a filler dose of 1:1, namely 0.67 MPa. With the other doses (1:3 and 3:1), the compressive strength was almost identical.

3 RESULTS AND DISCUSSION

The concrete composites prepared were characterized by their bulk density, thermal conductivity coefficient, and compressive strength at a specific deformation. The purpose of using recycled plastic aggregate in combination with wood chips was to reduce the bulk density of the lightweight concrete, where the characteristics of the samples were monitored at different filler ratios. The primary goal of the experimental research was to find a combination of plastic recyclate with wood chips in a specific ratio, the resulting bulk density of which reaches the lowest values when taking into account the thermo-physical properties. The results showed that the amount of plastic material used significantly affects the monitored properties of the light chip-cement composites. As their proportion increased, the specific gravity of the composites decreased, which means that the lowest volume values were achieved by samples with 100% filler content made from recycled plastic. This was due to the significant weight and the difference in proportion between the recycled plastic waste and wood chips. Also, the varying compactibility, absorbency, porosity and volume changes of the materials had an impact on the resulting parameters of the samples. The lowest value was achieved with sample SE5 with the EPS used, namely, 260 $kg.m^{-3}$. Conversely, samples with 100% filler content from chips had the highest value, where the value reached 500 $kg.m^{-3}$. This fact can be attributed to the method of processing the mixture, where it concerned the method of placing the mixture in the mold and the structure of the filler used. The coefficient of thermal conductivity took a similar course as the bulk density. It also turned out that the most optimal values were achieved by the samples with a filler content from recycled EPS, 0.066 $W.m^{-1}.K^{-1}$. The resulting thermal characteristics were affected by the thermo-physical properties of the individual materials, which changed the overall character, depending on the amount used. In contrast to the bulk density, the combination of wood chips and polyurethane foam in a ratio of 1:1 with a value of 0.1293 $W.m^{-1}.K^{-1}$ was the most unfavorable. The compressive strength at a specific strain reached the lowest value for the pure polyurethane foam, where it was 0.18 MPa at a 10% deformation. Conversely, the highest values were for the composites with a combination of filler based on polyurethane foam in combination with wood chips in a 1:1 ratio, where the resulting value was 0.67 MPa at a 5% deformation and also at a 100% wood chip content with a value of 0.76 MPa at a 2.5% deformation. This parameter was dependent on the elasticity, resistance, strength, and the structure of the material. The higher the elasticity of the material, the greater the ability of the sample to return to its original shape and resist the pressure applied.

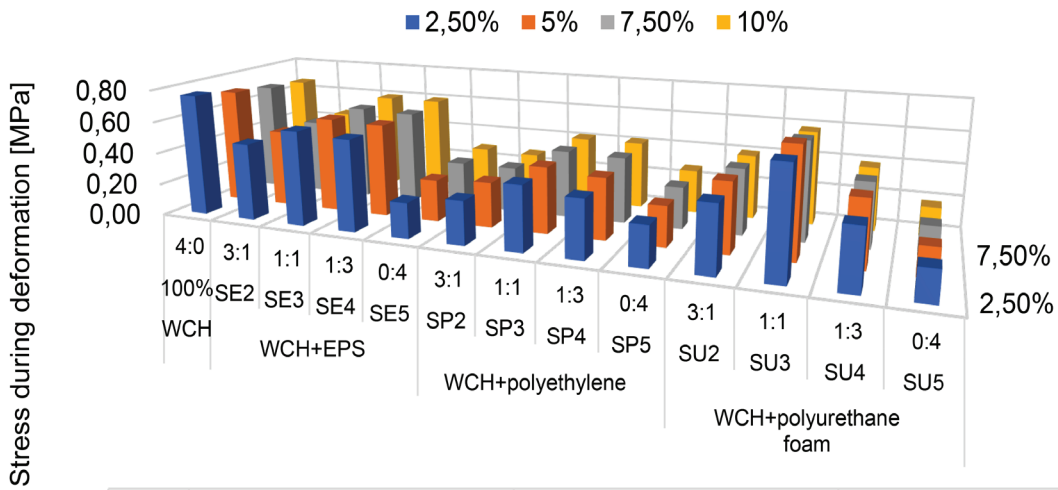

	WCH	WCH+EPS				WCH+polyethylene				WCH+polyurethane foam			
	100%	SE2	SE3	SE4	SE5	SP2	SP3	SP4	SP5	SU2	SU3	SU4	SU5
	4:0	3:1	1:1	1:3	0:4	3:1	1:1	1:3	0:4	3:1	1:1	1:3	0:4
2,50%	0,76	0,48	0,59	0,57	0,22	0,27	0,4	0,36	0,25	0,41	0,66	0,37	0,19
5%	0,72	0,48	0,59	0,58	0,26	0,28	0,41	0,38	0,25	0,43	0,67	0,41	0,18
7,50%	0,69	0,47	0,59	0,58	0,28	0,28	0,42	0,41	0,26	0,41	0,61	0,4	0,18
10%	0,67	0,46	0,6	0,6	0,29	0,28	0,42	0,42	0,27	0,4	0,58	0,39	0,18

Fig. 6 *Dependence of the compressive strength at a specified strain on the type and ratio of filler used.*

4 CONCLUSION

The construction industry is one of the most developed industries that is constantly advancing and looking for innovative technologies to minimize the energy load and decrease environmental pollution. This is an excellent prerequisite for the application of recycled plastics to building elements from economic and ecological points of view. However, the disadvantage is the deterioration of the quality of plastics during recycling. For this reason, improving the physical-mechanical and thermal-technical properties of other composites is necessary for their full use in construction. This article deals with the usability of three types of recycled plastic waste (EPS, PE, PU) as an alternative substitute for coarse aggregate, which was combined with wood chips in specific proportions. It can be concluded from the experiment that a larger proportion of plastic aggregates in the sample had an effect on reducing its bulk density. The lightest alternative was the sample with a filler containing only recycled EPS; on the contrary, the component with a pure dose of wood chips achieved the highest bulk density. This resulted from the weight and physical properties of the individual materials, where all three types of plastic aggregates used had a lower bulk density than the wood chips in 100% doses. The use of such materials in load-bearing constructions has a good future in terms of reducing their bulk density and improving their thermal insulation properties. The problem could be lower compressive, tensile, and bending strengths and resistance to environmental influences, regardless of the type of recycled plastic used. Therefore, further research is needed in this area. However, it can be concluded that classic solid wood can be partially replaced with recycled plastic in combination with wood chips, which would mean less plastic waste in the environment. In practice, this combination of materials could be used, for example, in anti-noise walls, load-bearing structural elements, thermal insulation materials, etc.

REFERENCES

Nabajyoti Saikia - Jorge de Brito, (2012). Use of Plastic Waste as Aggregate in Cement Mortar and Concrete Preparation: A Review. Construction and Building Materials, Vol. 34, pp. 385-401, ISSN 0950-0618, https://doi.org/10.1016/j.conbuildmat.2012.02.066.

Rabin Tuladhar - Shi Yin, (2019). 21 - Sustainability of using recycled plastic fiber in concrete, Editor(s): Fernando Pacheco-Torgal, Jamal Khatib, Francesco Colangelo, Rabin Tuladhar, In Woodhead Publishing Series in Civil and Structural Engineering, Use of Recycled Plastics in Eco-efficient Concrete, Woodhead Publishing, 2019, pp. 441-460, ISBN 9780081026762, https://doi.org/10.1016/B978-0-08-102676-2.00021-9.

Colin Jacob-Vaillancourt - Luca Sorelli, (2018). Characterization of concrete composites with recycled plastic aggregates from postconsumer material streams, Construction and Building Materials, Vol. 182, pp. 561-572, ISSN 0950-0618, https://doi.org/10.1016/j.conbuildmat.2018.06.083.

Malek Batayneh - Iqbal Marie - Ibrahim Asi, (2007). Use of selected waste materials in concrete mixes, Waste Management, Vol. 27, No. 12, pp. 1870-1876, ISSN 0956-053X, https://doi.org/10.1016/j.wasman.2006.07.026.

Rafat Siddique - Jamal Khatib - Inderpreet Kaur, (2018). Use of recycled plastic in concrete: A review, Waste Management, Vol. 28, No. 10, pp. 1835-1852, ISSN 0956-053X, https://doi.org/10.1016/j.wasman.2007.09.011.

Ibrahim Almeshal - Bassam A. Tayeh - Rayed Alyousef - Hisham Alabduljabbar -Abdeliazim Mustafa Mohamed - Abdulaziz Alaska, (2020). Use of recycled plastic as fine aggregate in cementitious composites: A review, Construction and Building Materials, Vol. 253, 119146, ISSN 0950-0618, https://doi.org/10.1016/j.conbuildmat.2020.119146.

Sifatullah Bahij - Safiullah Omary - Francoise Feugeas - Amanullah Faqiri, (2020). Fresh and hardened properties of concrete containing different forms of plastic waste: A review, Waste Management, Vol. 113, pp. 157-175, ISSN 0956-053X, https://doi.org/10.1016/j.wasman.2020.05.048.

Lei Gu - Togay Ozbakkaloglu, (2016). Use of recycled plastics in concrete: A critical review, Waste Management, Vol. 51, pp. 19-42, ISSN 0956-053X, https://doi.org/10.1016/j.wasman.2016.03.005.

Francesco Asdrubali - Francesco D'Alessandro - Samuele Schiavoni, (2015). A review of unconventional sustainable building insulation materials, Sustainable Materials and Technologies, Vol. 4, pp. 1-17, ISSN 2214-9937, https://doi.org/10.1016/j.susmat.2015.05.002.

Zdeněk Pastorek - Jaroslav Kára - Petr Jevič. Biomasa, (2004). Renewable energy source. FCC PUBLIC, ISBN 80-86534-06-5.

Alejandro Meza de Luna - Faiz Uddin Ahmed Shaikh, (2020). Anisotropy and bond behaviour of recycled Polyethylene terephthalate (PET) fibre as concrete reinforcement, Construction and Building Materials, Vol. 265, 120331, ISSN 0950-0618, https://doi.org/10.1016/j.conbuildmat.2020.120331.

Wensu Chen, Hong Hao - Dylan Hughes - Yanchao Shi - Jian Cui - Zhong-Xian Li, (2015). Static and dynamic mechanical properties of expanded polystyrene, Materials & Design, Vol. 69, pp. 170-180, ISSN 0261-3069, https://doi.org/10.1016/j.matdes.2014.12.024.

Gama Nuno V. - Artur Ferreira - Ana Barros-Timmons (2018). Polyurethane Foams: Past, Present, and Future Materials, Vol. 11, No. 10: 1841. https://doi.org/10.3390/ma11101841

Miriam Ledererova – ZuzanaŠtefunková – Valéria Gregorová, (2018). The use of environmentally acceptable plastic materials based on cement and polymer composites without consideration to their physical properties. IOP Conference Series: Materials Science and Engineering. 385. 012033. 10.1088/1757-899X/385/1/012033.

EN 206:2013+A2:2021: Concrete. Specification, performance, production and conformity

EN 197-1:2011: Cement - Part 1: Composition, specifications and conformity criteria for common cements